

Electronic Thesis and Dissertation Repository

---

9-24-2013 12:00 AM

## Application of Differential and Polarimetric Synthetic Aperture Radar (SAR) Interferometry for Studying Natural Hazards

Samira Alipour, *The University of Western Ontario*

Supervisor: Dr. Kristy Tiampo, *The University of Western Ontario*

A thesis submitted in partial fulfillment of the requirements for the Doctor of Philosophy degree in Geophysics

© Samira Alipour 2013

Follow this and additional works at: <https://ir.lib.uwo.ca/etd>



Part of the [Other Earth Sciences Commons](#), and the [Tectonics and Structure Commons](#)

---

### Recommended Citation

Alipour, Samira, "Application of Differential and Polarimetric Synthetic Aperture Radar (SAR) Interferometry for Studying Natural Hazards" (2013). *Electronic Thesis and Dissertation Repository*. 1673. <https://ir.lib.uwo.ca/etd/1673>

This Dissertation/Thesis is brought to you for free and open access by Scholarship@Western. It has been accepted for inclusion in Electronic Thesis and Dissertation Repository by an authorized administrator of Scholarship@Western. For more information, please contact [wlsadmin@uwo.ca](mailto:wlsadmin@uwo.ca).

APPLICATION OF DIFFERENTIAL AND POLARIMETRIC SYNTHETIC APERTURE RADAR (SAR)  
INTERFEROMETRY FOR STUDYING NATURAL HAZARDS

(Thesis format: Integrated-Articles)

by

Samira Alipour

Graduate Program in Geophysics

A thesis submitted in partial fulfillment

of the requirements for the degree of

Doctor of Philosophy

The School of Graduate and Postdoctoral Studies

The University of Western Ontario

London, Ontario, Canada

© Samira Alipour 2013

# Abstract

In the following work, I address the problem of coherence loss in standard Differential Interferometric SAR (DInSAR) processing, which can result in incomplete or poor quality deformation measurements in some areas. I incorporate polarimetric information with DInSAR in a technique called Polarimetric SAR Interferometry (PolInSAR) in order to acquire more accurate and detailed maps of surface deformation.

In Chapter 2, I present a standard DInSAR study of the Ahar double earthquakes ( $M_w=6.4$  and 6.2) which occurred in northwest Iran, August 11, 2012. The DInSAR coseismic deformation map was affected by decorrelation noise. Despite this, I employed an advanced inversion technique, in combination with a Coulomb stress analysis, to find the geometry and the slip distribution on the ruptured fault plane. The analysis shows that the two earthquakes most likely occurred on a single fault, not on conjugate fault planes. This further implies that the minor strike-slip faults play more significant role in accommodating convergence stress accumulation in the northwest part of Iran.

Chapter 3 presents results from the application of PolInSAR coherence optimization on quad-pol RADARSAT-2 images. The optimized solution results in the identification of a larger number of reliable measurement points, which otherwise are not recognized by the standard DInSAR technique. I further assess the quality of the optimized interferometric phase, which demonstrates an increased phase quality with respect to those phases recovered by applying standard DInSAR alone.

Chapter 4 discusses results from the application of PolInSAR coherence optimization from different geometries to the study of creep on the Hayward fault and landslide motions near Berkeley, CA. The results show that the deformation rates resolved by PolInSAR are in agreement with those of standard DInSAR. I also infer that there is potential motion on a secondary fault, northeast and parallel to the Hayward fault, which may be creeping with a lower velocity.

Finally, discussions on the application of the PolInSAR technique and the geophysical implications of the standard DInSAR study are presented, with suggestions for future work, in the conclusions.

## Keywords

Differential Interferometric Synthetic Aperture Radar (DInSAR), Polarimetric SAR Interferometry (PolInSAR), polarimetry, coherence optimization, surface deformation, Hayward fault, Berkeley landslides, Ahar earthquake

## Co-Authorship Statement

The thesis is prepared in integrated-article format and the following manuscripts were written by Samira Alipour:

- Alipour, S., Tiampo, K.F., González, P.J., Samsonov, S., Source model for the 2012 Ahar double earthquakes, Iran, from DInSAR analysis of RADARSAT-2 imagery, *submitted to the Geophysical Journal International*.
- Alipour, S., Tiampo, K., González, P.J., 2013. Multibaseline PolInSAR Using RADARSAT-2 Quad-Pol Data: Improvements in Interferometric Phase Analysis. *IEEE Geosciences and Remote Sensing Letters*, doi:10.1109/LGRS.2012.2237501
- Alipour, S., Tiampo, K.F., González, P.J., Samsonov, S., Short-term surface deformation on the northern Hayward fault, CA, and nearby landslides using Polarimetric SAR Interferometry (PolInSAR), *accepted by Pure and Applied Geophysics*.

The work for these projects was completed under supervision of Dr. Kristy Tiampo and with financial support from the Ontario Early Researcher Award and the NSERC and Aon Benfield/ICLR Industrial Research Chair in Earthquake Hazard Assessment. RADARSAT-2 images were provided by the Canadian Space Agency.

The DInSAR deformation map of Ahar earthquake was processed by Sergey Samsonov.

The orbital refinement code for DInSAR products was produced by Pablo González.

The Small Baseline technique for multibaseline processing of DInSAR images was developed by Sergey Samsonov and applied to this analysis by Samira Alipour.

## Acknowledgments

First and foremost I offer my sincerest gratitude to my supervisor Dr. Kristy Tiampo, who has supported me throughout my thesis with her valuable guidance and advice while allowing me the freedom to work in my own way. I attribute my PhD degree to her motivation and encouragement.

I offer my sincere thanks to Dr. Sergey V. Samsonov and Dr. Pablo J. González for their insightful guidance throughout the completion of my research. Their motivation inspired me immensely during my graduate studies and I truly appreciate their time and willingness to help.

My special thanks go to all my friends at the Department of Earth Sciences, University of Western Ontario, who supported me through my toughest times.

Last but not the least, I would like to thank my family: My parents, Nazi and Ali, and my older brother and sister, Aydin and Elmira. I cannot thank them enough for their dedication, many years of support and standing by me in my good times and bad times.

# Table of Contents

Abstract.....	ii
Co-Authorship Statement.....	iv
Acknowledgments.....	v
Table of Contents.....	vi
List of Tables.....	x
List of Figures.....	xi
<b>Chapter 1.....</b>	<b>1</b>
<b>1 General Introduction.....</b>	<b>1</b>
1.1 Introduction.....	1
1.2 Synthetic Aperture Radar (SAR).....	2
1.3 SAR Geometry.....	5
1.4 SAR Radiometric Correction.....	7
1.5 SAR Image Statistics.....	7
1.6 Differential Interferometric SAR (DInSAR).....	8
1.7 Coherency.....	12
1.8 Advanced DInSAR Techniques.....	14
1.9 SAR Polarimetry.....	16
1.10 Principles of SAR Polarimetry.....	16
1.11 Polarimetric SAR Interferometry (PolInSAR).....	18
1.12 Methodology.....	20
1.12.1 Co-registration.....	21
1.12.2 Baseline Estimation.....	21
1.12.3 Coherence Optimization.....	21

1.12.4 Interferogram Generation.....	23
1.12.5 Phase Unwrapping .....	23
1.12.6 Residual Orbital Error Correction.....	24
1.12.7 Multibaseline Analysis.....	25
1.13 Purpose of Study.....	26
1.14 Organization of Work .....	27
1.15 References.....	28
<b>Chapter 2 .....</b>	<b>33</b>
<b>2 Source model for the 2012 Ahar double earthquakes, Iran, from DInSAR analysis of RADARSAT-2 imagery .....</b>	<b>33</b>
2.1 Introduction.....	34
2.2 DInSAR Data .....	37
2.3 Slip Model from DInSAR Technique.....	39
2.4 Earthquake Triggering .....	58
2.5 Discussions .....	59
2.6 Conclusion .....	61
2.7 Acknowledgements.....	61
2.8 References.....	62
<b>Chapter 3 .....</b>	<b>67</b>
<b>3 Multibaseline PolInSAR using RADARSAT-2 Quad-pol data: improvements in interferometric phase analysis .....</b>	<b>67</b>
3.1 Introduction.....	68
3.2 Polarimetric SAR Interferometry (PolInSAR).....	69
3.3 Application of Coherence Optimization Technique .....	71
3.4 Performance of the Coherence Optimization Algorithm.....	73

3.5 Conclusion .....	79
3.6 Acknowledgments.....	80
3.7 References.....	80
<b>Chapter 4 .....</b>	<b>85</b>
<b>4 Short-term surface deformation on the northern Hayward fault, CA, and nearby landslides using Polarimetric SAR Interferometry (PolInSAR) .....</b>	<b>85</b>
4.1 Introduction.....	86
4.2 Region of Study .....	90
4.3 Polarimetric SAR Interferometry (PolInSAR).....	91
4.4 Application of PolInSAR.....	93
4.5 Results.....	97
4.5.1 Creep along North Hayward Fault .....	97
4.5.2 Landslide Motion .....	103
4.6 Discussions .....	107
4.7 Conclusion .....	111
4.8 Acknowledgements.....	111
4.9 References.....	112
<b>Chapter 5 .....</b>	<b>116</b>
<b>5 Conclusions .....</b>	<b>116</b>
5.1 Summary and Conclusions .....	116
5.2 Future Work.....	118
5.2 References.....	119
<b>A Glossary.....</b>	<b>120</b>

<b>B Computer Code</b> .....	121
B.1 run_ESM.cpp .....	121
B.2 complement.cpp .....	145
<b>C Curriculum Vitae</b> .....	151

## List of Tables

<b>Table 1.1</b> Space-borne SAR system characteristics .....	8
<b>Table 2.1</b> Source parameters and the associated errors for a single fault derived from the GA inversion.....	41
<b>Table 2.2</b> Fault slip inversion results for the single fault solution with different smoothing values as Figures 2.5-2.10.....	50
<b>Table 2.3</b> Fault slip inversion results for the two fault solution with different geometries as in Figures 2.11-2.14. ....	55
<b>Table S1</b> Spatial and temporal separation of interferograms .....	82

## List of Figures

<b>Figure 1.1</b> SAR image geometry and the location of pixels in range and azimuth direction (Massonnet & Feigl 1998) .....	3
<b>Figure 1.2</b> An example of SAR amplitude image of an area in Mojave Desert, CA (Bamler & Hartl 1998) .....	4
<b>Figure 1.3</b> Different imaging modes: (a) Stripmap, (b) ScanSAR and (c) Spotlight (Moreira et al. 2013) .....	5
<b>Figure 1.4</b> Summary of SAR processing steps where the range and azimuth compressed data result from a convolution of the raw data with the reference function (Moreira et al. 2013)....	6
<b>Figure 1.5</b> Satellite interferogram of Bam earthquake (Mw= 6.5, 26 December 2003). Each fringe represents 28 mm of displacement in the LOS satellite direction (Motagh et al. 2006).	9
<b>Figure 1.6</b> (a) Initial interferograms of Bam earthquake (Mw= 6.5, 26 December 2003) (b) the final interferogram after removal of orbital and topographic contribution and (c) the final displacement map showing the amount of deformation (Motagh et al. 2006) .....	12
<b>Figure 1.7</b> Coherence image of a RADARSAT-2 interferogram from the Ahar 2012 earthquakes .....	14
<b>Figure 1.8</b> The polarization ellipse decomposed into orthogonal components x (horizontal H) and y (vertical V) (Advanced Radar Polarimetry Tutorial, Canada Center for Remote Sensing).....	17

**Figure 2.1** The location of August 11, 2012 Ahar earthquakes and the corresponding focal mechanisms from Global CMT solutions. The aftershocks are recorded by IIEES (<http://www.iiees.ac.ir/English/>). The vectors are the GPS velocities with respect to the Central Iran block (Masson et al. 2007). NTF represents the North Tabriz Fault. The inset shows the location of our study area within the northwest Iran. ....36

**Figure 2.2** Observed DInSAR deformation without orbital errors removed .....38

**Figure 2.3** (a) Modeled displacement and (b) residual displacement from the GA solution for a single fault with a uniform-slip model. The surface expression of the modeled dislocations is shown by a black rectangle. ....40

**Figure 2.4** (a) Moment magnitude versus smoothing factor and (b) model roughness versus model residuals. The black square mark the location of the optimum smoothing factor and the red squares mark two examples of extreme smoothing factors considered for comparison .....41

**Figure 2.5** (a) Modeled displacement and (b) residual displacement on a single fault using a distributed-slip model (smoothing factor of 0.38). The surface expression of the modeled dislocations is shown by the black rectangle. ....44

**Figure 2.6** (a) Oblique slip, (b) strike slip and (c) dip slip on a single fault using a distributed slip model and smoothing factor of 0.38. The surface expression of the fault is shown in Figure 2.5. ....45

**Figure 2.7** (a) Modeled displacement and (b) residual displacement on a single fault using a distributed-slip model and a smoothing factor of 0.1. The surface expression of the modeled dislocations is shown by a black rectangle. ....46

**Figure 2.8** (a) Oblique slip, (b) strike slip and (c) dip slip on a single fault using a distributed slip model and a smoothing factor of 0.1. The surface expression of the fault is shown in Figure 2.7. ....47

**Figure 2.9** (a) Modeled displacement and the (b) residual displacement on a single fault using a distributed-slip model and a smoothing factor of 0.6. The surface expression of the modeled dislocations is shown by a black rectangle. ....48

**Figure 2.10** (a) Oblique slip, (b) strike slip and (c) dip slip on a single fault using a distributed slip model and a smoothing factor of 0.38. The surface expression of the fault is shown in Figure 2.9.....49

**Figure 2.11** (a) Modeled displacement and (b) residual displacement on two faults and using a distributed-slip model and a smoothing factor of 0.38. The surface expression of the modeled dislocations is shown by a black rectangle. ....52

**Figure 2.12** (a) Modeled displacement and the (b) residual displacement on two faults and using a distributed-slip model and a smoothing factor of 0.38. The surface expression of the modeled dislocations is shown by a black rectangle .....53

**Figure 2.13** Slip distribution on two faults using a distributed slip model and a smoothing factor of 0.38, on the (a) primary fault and (b) secondary fault. The surface expression of the fault is shown in Figure 2.11.....54

**Figure 2.14** Slip distribution on two faults using a distributed slip model and a smoothing factor of 0.38, on the (a) primary fault and (b) secondary fault. The surface expression of the fault is shown in Figure 2.12.....55

**Figure 2.15** Coulomb stress at (a) zero depth, (b) 5 km depth, (c) 10 km depth and (d) 15 km depth. At the middle of the fault and toward the east there is a decrease in the Coulomb stress .....57

**Figure 3.1** RGB amplitude image of San Francisco city acquired from RADARSAT-2 satellite (R: HH channel, G: VV channel, B: VH channel). The black line delineates the approximate trace of the Hayward fault. The red square shows the close up region used for interferometric analysis. The black and white figure shows the two subregions used for further analysis in Figures 3.3-3.4. White and gray colors represents urban the rural areas, respectively. ....71

**Figure 3.2** Mean coherence maps, (a) HH, (b) VV, (c) VH and (d) optimized images. Improvement of PolInSAR coherence (d) is clearly demonstrated with respect to single-pol channels (a-c). ....73

**Figure 3.3** (a-c) Histograms of the mean coherences for the HH and the optimized polarimetric channels associated with (a) the entire image, (b) rural and (c) urban subregions. (d-f) PCs increment after application of PolInSAR for an arbitrary coherence threshold. Here, the horizontal axis represents the coherence threshold and the vertical axis is the increase in the number of PCs from HH channel to the optimized channel, associated with (d) the entire image, (e) the rural subregion and (f) the urban subregion. Note that the percentage is with respect to the entire image pixels. (g-i) histogram of  $\alpha$  angle for the newly selected PCs in the optimized compared to HH channel (with coherence threshold of 0.3) for the (g) entire image pixels, (h) rural and (i) urban subregions, respectively. ....76

**Figure 3.4** (a-c) Relative mean coherence improvement (with respect to initial HH coherence) for individual interferograms of different spatial and temporal baseline, for (a) the entire image, (b) rural subregion and (c) urban subregion. ....77

**Figure 3.5** Example of an interfreogram formed between dates 2008/06/13-2011/03/18 for the close up region in Figure 3.1. (a-b) refer to the HH and optimized interferograms for pixels marked as PCs in each channel. (c-d) refer to the HH and optimized interferograms for pixels only marked as PCs in the optimized channel. Comparison of the interferograms shows that the main features of interferograms are preserved after application of PolInSAR technique. Comparing (c) and (d) shows that the quality of phase improves after application of PolInSAR technique. ....78

**Figure 4.1** SRTM Topography for the San Francisco region with RADARSAT-2 trajectories. The blue and green boxes mark the footprint of ascending and descending tracks, respectively. The red lines represent the faults in this region. ....88

**Figure 4.2** Linear deformation map derived from SBAS technique by using single-channel HH dataset for the (a) descending (d) ascending tracks. Linear deformation map derived from SBAS technique by using single-channel VV dataset for the (b) descending (e) ascending tracks. Linear deformation map derived from SBAS technique by using the optimized channel for the (c) descending (f) ascending tracks. Note that here the LOS shortening is represented by positive and LOS lengthening is represented by negative values. The black lines represent the faults in this region, as in Figure 4.1. The black squares in (c) and (f) mark the reference region for calibration of DInSAR images in the descending and ascending geometries, respectively. ....96

**Figure 4.3** Location of profiles in the PolInSAR deformation map marked by red lines and the numbers associated with each. The deformation rate along these profiles is presented in Figures 4.4-4.5. The black lines represent the faults in this region, as in Figure 4.1. The black line parallel to the Hayward fault in the north (identified by the black arrow) represents the location of a secondary fault that may experience creep events. ....98

**Figure 4.4** Linear rate of deformation along profiles in Figure 4.3, derived from descending images. The horizontal axis represents distance from Hayward fault. The red line marks the location of Hayward fault. The black line in profiles (1-4) might be another fault parallel to the Hayward fault in the north (the location is shown in Figure 4.3). ....99

**Figure 4.5** Linear rate of deformation along profiles in Figure 4.3, derived from ascending images. The horizontal axis represents distance from Hayward fault. The red line marks the location of Hayward fault. The black line in profiles (1-4) might be another fault parallel to the Hayward fault in the north (the location is shown in Figure 4.3). ....100

**Figure 4.6** Residual errors of linear deformation map derived from SBAS technique by using single-channel HH dataset for the (a) descending (d) ascending tracks. Residual errors of linear deformation map derived from SBAS technique by using single-channel VV dataset for the (b) descending (e) ascending tracks. Residual errors of linear deformation map

derived from SBAS technique by using the optimized channel for the (c) descending (f) ascending tracks. Note that here the LOS shortening is represented by positive and LOS lengthening is represented by negative values. The black lines represent the faults in this region, as in Figure 4.1. The black squares in (c) and (f) mark the reference region for calibration of DInSAR images in the descending and ascending geometries, respectively..102

**Figure 4.7** LOS linear displacement maps for the Berkeley landslides: Figures (a), (c) and (e) are the maps from ascending images derived from (a) the HH, (c) the VV and (e) the PolInSAR optimized channel. Figures (b), (d) and (f) show the corresponding maps from descending images derived from (b) the HH, (d) the VV and (f) the PolInSAR optimized channel. Note that positive displacement represents motion toward the satellite. The black and red polygons outline the location of moderately active and highly active slope instabilities (USGS Earthquake Hazard Program 1999). The black dashed lines represent the faults in this region, as in Figure 4.1.....104

**Figure 4.8** Optimized linear deformation maps for (a) ascending (b) descending tracks, overlaid on an aerial photography. The orange and red polygons outline the location of moderately active and highly active slope instabilities (USGS Earthquake Hazard Program 1999). The black lines represent the faults in this region, as in Figure 4.1. ....106

**Figure 4.9** Residual errors of linear deformation rate after application of the SBAS technique: (a), (c) and (e) are the maps from ascending images derived from (a) the HH, (c) the VV and (e) the PolInSAR optimized channel. Figure 4.9 (b), (d) and (f) show the corresponding maps from descending images derived from (b) the HH, (d) the VV and (f) the PolInSAR optimized channel. The black and red polygons outline the location of moderately active and highly active slope instabilities (USGS Earthquake Hazard Program 1999). The black dashed lines represent the faults in this region, as in Figure 4.1.....109

## Chapter 1

### 1 General Introduction

#### 1.1. Introduction

Differential Interferometric Synthetic Aperture Radar (DInSAR) is a remote sensing tool for measuring ground surface deformation induced by natural or man-made processes. The interferometric approach is based on the phase comparison of synthetic aperture radar (SAR) images gathered, via satellite, at different times with slightly different looking angles (Massonnet & Feigl 1998; Bamler & Hartl 1998). DInSAR has the advantage of mapping an area of hundreds of square kilometers with high spatial and temporal resolution. This technique has additional advantage of mapping in all-weather conditions. The deformation at the ground surface may reflect the distribution of stress in the subsurface and provide more detail on both the past and future behavior of the surface deformation and its associated causes. In this regard, inverse modeling is required to obtain knowledge about subsurface processes from these surface measurements. DInSAR has been used for monitoring volcano dynamics (Massonnet et al. 1995; Manconi et al. 2010), coseismic displacements (Massonnet et al. 1993; González et al. 2013), subsidence due to exploitation of ground-water and oil/gas (Amelung et al. 1999; Tiampo et al. 2012) and mining subsidence (Carnec & Delacourt 2000). Recently this technique also has been used for the monitoring of deformation associated with carbon sequestration and the melting of permafrost (Vasco et al. 2008; Short et al. 2012). Multi-baseline DInSAR techniques have also been developed which are able to measure surface deformation with milometer accuracy by using a larger number of SAR images (Sandwell & Price 1998; Bernardino et al. 2002; Feretti et al. 2001; Hooper et al. 2007; Samsonov & d'Oreye 2012).

The Ahar double earthquakes ( $M_w=6.4$  and  $6.2$ ) struck northwest Iran on August 11, 2012. The earthquakes are located 50 km north from the largest and the most hazardous strike-slip fault structure in this region. I implemented a standard DInSAR technique in

order to map the co-seismic deformation using RADARSAT-2 SAR images. Moreover, I applied inversion schemes to find the ruptured fault geometry and solve for its distributed slip. Modeling of the surface deformation not only shows that the two events occurred on one fault plane, it also provided important insights into the pattern of stress accumulation and release in this region.

One of the drawbacks of DInSAR is that the radar signal decorrelates in the presence of volume scattering such as vegetation cover and causes degradation of the interferometric phase. This was a limitation on the study in Ahar, above. New radar satellites have the capability of performing measurement in multi-polarizations, providing more observations of the ground surface. In this work I implement Polarimetric SAR Interferometry (PolInSAR), a technique for integrating polarimetry and interferometry in order to increase the precision of DInSAR measurements. In addition, I apply this technique to measure creep rate on Hayward fault, CA. This analysis demonstrates the efficiency of this technique for providing a more precise interferometric phase measurement.

In the following sections I will describe fully the basics of SAR, DInSAR and Advanced DInSAR and PolInSAR techniques.

## **1.2. Synthetic Aperture Radar (SAR)**

Synthetic Aperture Radar (SAR) is an imaging radar system onboard a moving platform. In this system, electromagnetic waves are transmitted and the backscattered echoes are collected. Due to the platform movement, each reception corresponds to different positions in a SAR scene and each single pixel is assigned an azimuth and range coordinate. The azimuth is the direction of platform movement and the range direction is the Line-of-Sight (LOS) direction, the distance from the moving platform to the ground. Figure 1.1 demonstrates that the 3-dimensional objects are projected to a 2-dimensional space in radar geometry (range and azimuth). Radar geometry is represented by circles

and hyperbola. The circles are the lines of equal-distance (range) and the hyperbola are the lines of equal-doppler (azimuth).

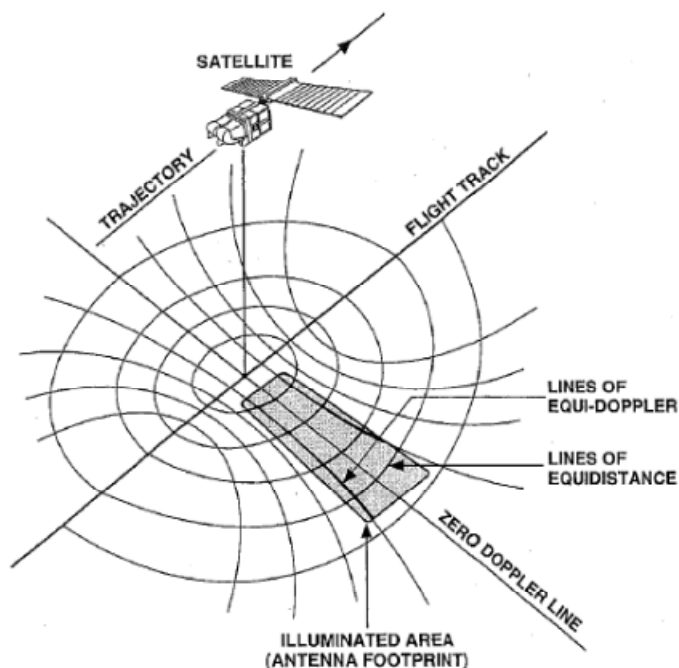


**Figure 1.1. SAR image geometry and the location of pixels in range and azimuth direction (Massonnet & Feigl 1998).**

A SAR image is a complex valued matrix, including amplitude and phase. Figure 1.2 is an example of a SAR amplitude image. The areas with higher reflectivity are brighter in this image. However, a SAR phase image looks like a random noise image with values ranging between 0-360 degrees. Each SAR image pixel represents the coherent sum of all scattering elements within a resolution cell.

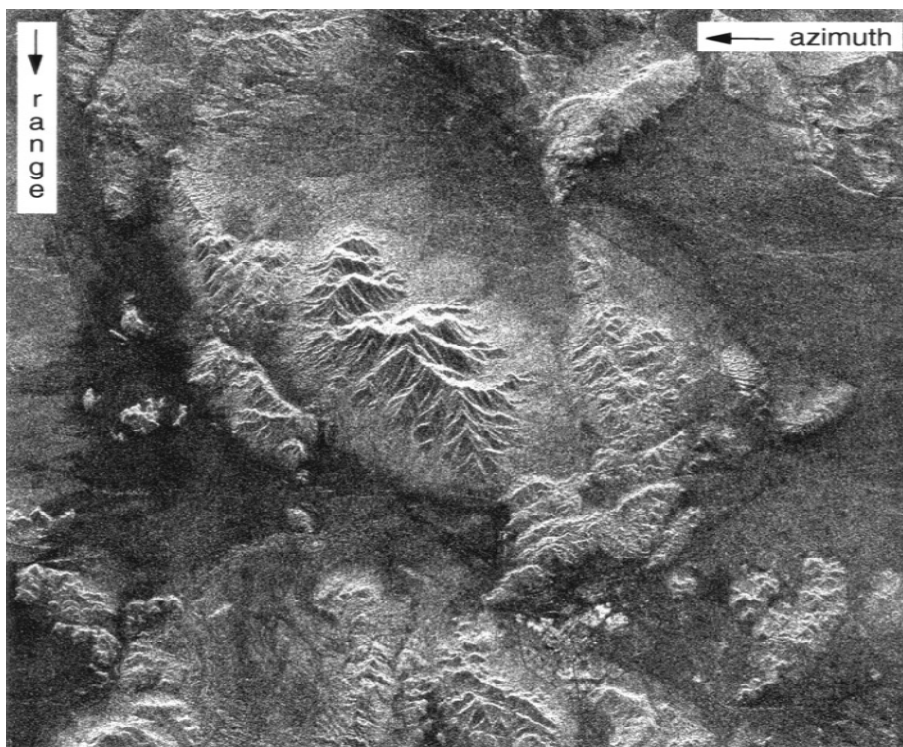


**Figure 1.2. An example of SAR amplitude image of an area in Mojave Desert, CA (Bamler & Hartl 1998)**

Space-borne SAR systems operate with different radar wavelengths. The advantages and disadvantages of choosing different wavelengths for interferometric applications will be discussed in section 1.7. Table 1.1 lists space-borne SAR systems with the corresponding imaging characteristics. SAR systems also operate in a variety of imaging modes. This is done by altering the SAR antenna radiation pattern. These imaging modes are: Stripmap, ScanSAR and Spotlight (Figure 1.3). For the Stripmap mode, the antenna illuminates one swath and creates one single strip of radar data (Moreira et al. 2013). For the ScanSAR mode the antenna illuminates different swaths with a shorter illumination time which degrades the azimuth resolution (Ahmed et al. 1990; Bamler & Eineder 1996). The Spotlight mode is designed so that the antenna is steered illuminating a certain location on ground, increasing the spatial resolution (Carrara et al. 1995).

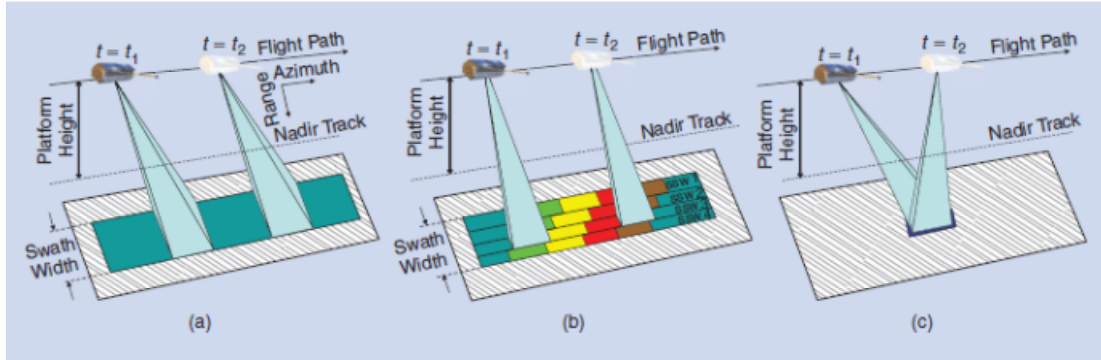


**Figure 1.3. Different imaging modes: (a) Stripmap, (b) ScanSAR and (c) Spotlight (Moreira et al. 2013).**

### 1.3. SAR Geometry

In radar system, the slant-range resolution ( $dr$ ) is dependent on the system bandwidth and is derived by (1.1)

$$dr = \frac{c_0}{2B} \quad (1.1)$$

where  $c_0$  is the speed of light and  $B$  is the system bandwidth (Elachi 1987).

Older radar systems had the drawback of lower resolution in the azimuth direction. This limitation has been overcome by the use of coherent radar and image processing techniques (Wiley 1985), leading to an improvement of the azimuth resolution. The resulting azimuth resolution ( $da$ ) is independent of the range distance and is equal to half the azimuth antenna length ( $dl$ ) (Elachi 1987),

$$da = \frac{dl}{2} \quad (1.2)$$

Raw radar images require initial processing in order to transform them into a single-look (SLC) image, as shown in Figure 1.1. This includes filtering at both the range and azimuth directions named as range compression and azimuth compression (Cumming & Wong 2005). As the radar travels along the flight track, the transmitted pulses are linear frequency modulated chirp signals. Range compression is applied with a filter on the raw

data in order to compress all the energy distributed over the chirp duration into as narrow as a possible time window (Moreira et al. 2013). In this process each range line is multiplied in the frequency domain by the complex conjugate of the spectrum of the transmitted chirp. Figure 1.4 demonstrates the range and azimuth compression applied to a raw radar data.

Because of the platform motion, the signal in the azimuth direction is modulated by the doppler frequency. The azimuth focusing can be achieved by correlating the azimuth line with a reference function in the frequency domain (Moreira et al. 2013). This will give a focused SAR image in both the range and azimuth directions.

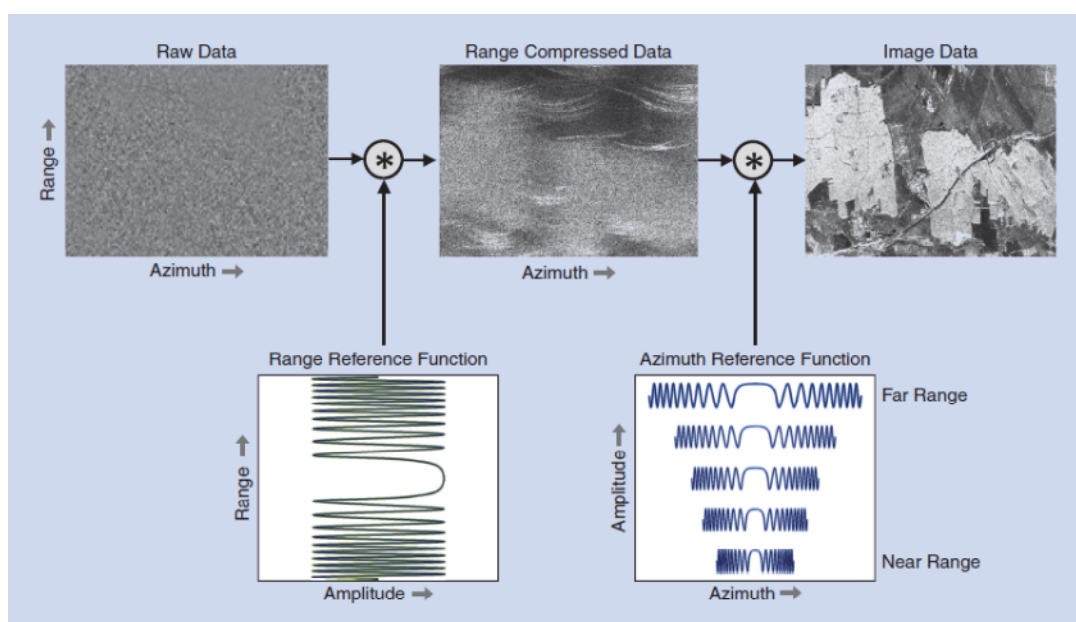


**Figure 1.4. Summary of SAR processing steps where the range and azimuth compressed data result from a convolution of the raw data with the reference function (Moreira et al. 2013).**

#### 1.4. SAR Radiometric Correction

The magnitude of the SAR image is not uniform over the entire image and is affected by different factors, such as the pattern of the antenna diagram, the longer traveling path of a wave in the far range compared to near range, etc. (Elachi 1987). In order to compensate for these effects a radiometric calibration is needed to derive the radar cross section normalized to the area. A calibrated SAR can be either in the  $\delta_0$  or in the  $\gamma_0$  form. In the  $\delta^0$  case the SAR image intensity corresponds to the backscattering coefficient normalized to the horizontal ground surface. In the case of  $\beta^0$  the SAR image intensity corresponds to the normalized backscattering coefficient in the range direction (Freeman 1992).

#### 1.5. SAR Image Statistics

One characteristic of SAR images is the speckle, which is caused by the presence of many independent scatterers within one resolution cell (Goodman 1976). The coherent sum of their amplitudes and phases results in strong fluctuations of the backscattering from one pixel to the other. The intensity and the phase of SAR image pixels are not deterministic, because of the presence of speckle noise, and follow an exponential and uniform distribution, respectively (Oliver & Quegan 2004). The total complex reflectivity ( $p'$ ) for each resolution cell is given by

$$p' = \sum_j \sqrt{\delta'_j} \exp(i\varphi_j^{scatt}) \cdot \exp(-i\frac{4\pi}{k'} r_j), \quad (1.3)$$

where  $\delta'$ ,  $\varphi$  and  $r$  is the radar cross section, phase and range distance for each individual scatterer.  $j$  is the number of the scatterer and  $k'$  is the wave number.

In order to decrease the effect of speckle, a common technique such as multilooking is applied. This technique is an averaging of the intensity image (Curlander & McDonough 1991; Oliver & Quegan 2004). One drawback of multilooking is that it decreases the

SAR image resolution. However, by using this technique a better understanding of target characteristics is achieved.

**Table 1.1. Space-borne SAR system characteristics**

Abbreviation	Launch Date	Band	Repetition Cycle	Maximum Resolution (meters)
SEASAT	1978	L	3	25
ERS-1	1991	C	3, 35, 168	30
ERS-2	1995	C	35	30
JERS-1	1992	L	44	18
Radarsat-1	1995	C	24	10
SIR-C	1994	X, C, L	Variable	18
ENVISAT	2002	C	35	30
SRTM	2000	C, X	35	12
ALOS	2006	L	46	10
TerraSAR-X	2007	X	11	1
TanDEM-X	2010	X	11	1
Radarsat-2	2007	C	24	1
COSMO –SkyMed-1/4	2007	X	16	1
RISAT-1	2012	C	25	3
HJ-1C	2012	S	4	5

### 1.6. Differential Interferometric Synthetic Aperture Radar (DInSAR)

An interferogram is formed by pixel-wise multiplication of the complex backscattering signals,  $V$ , of two SAR images (Bamler & Hartl 1998),

$$V(R, x) = V_1(R, x)V_2^*(R, x) = |V_1(R, x)||V_2(R, x)| \exp(j\phi(R, x)) \quad (1.4)$$

where \* denotes the complex conjugate,  $\phi = \phi_2 - \phi_1$  is the interferometric phase, and  $V(R, x)$  is the complex number corresponding to a SAR image.  $R$  and  $x$  are the range and

azimuth coordinates. Figure 1.5 displays an example of an interferogram from Bam earthquake, where each cycle represents 28 mm of displacement in LOS direction.

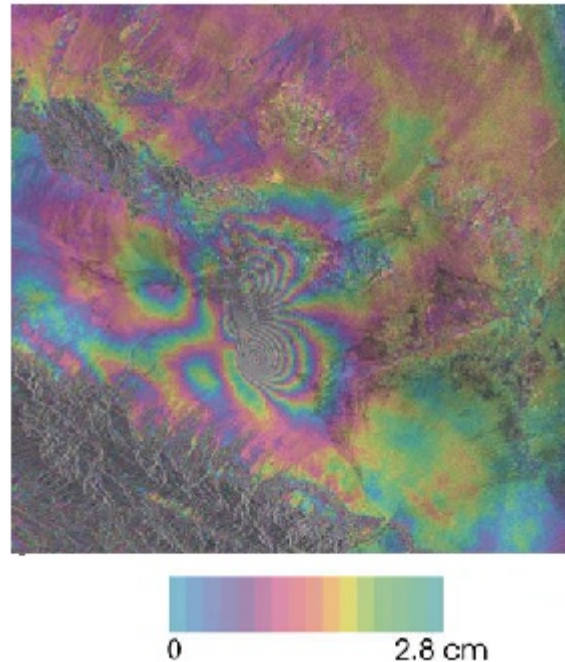


**Figure 1.5. Satellite interferogram of Bam earthquake (Mw= 6.5, 26 December 2003). Each fringe represents 28 mm of displacement in the LOS satellite direction for C-band which 56 mm (Motagh et al. 2006).**

The interferometric phase results from the following contributions determining differences in the propagation path length between the two images:

$$\phi = \phi_{flat} + \phi_{topo} + \phi_{dis} + \phi_{atm} + noise \quad (1.5)$$

where  $\phi_{flat}$  and  $\phi_{topo}$  are the phase differences associated with the flat earth and topography (Massonnet & Feigl 1998). Flat earth component is the effect of a distance between two satellite positions causing long-wavelength fringes. The topographic phase

is the effect of elevation, which depending on the perpendicular baseline ( $B_n$ ) produces additional phase component. The perpendicular baseline is the distance between two antenna positions, perpendicular to the LOS direction.

$\phi_{atm}$  is the phase difference due to changes in atmospheric propagation. The atmospheric phase variation is dominated by water vapour (Hanssen 2001). It is not possible to correct for atmospheric effects in a single interferogram without information on the state of the atmosphere from other data sources. The atmospheric delay gradient can be in the order of up to 1cm/km or more (Hanssen 2001).  $\phi_{dis}$  is the phase difference due to displacement of the observed surface element in LOS.

We can expand equation (1.5) to (1.6):

$$\phi = \frac{4\pi}{\lambda'} B_n + \frac{4\pi}{\lambda' r \sin \theta'} B_n \Delta q + \frac{4\pi}{\lambda'} d + \phi_{atm} + noise \quad (1.6)$$

$\Delta q$  is the surface elevation and  $\theta'$  is the radar look angle,  $d$  is the surface displacement, and  $\lambda'$  and  $r$  are the radar wavelength and satellite-ground distance, respectively.

Elimination of all the phase components (flat earth, topographic phase), will give the phase difference due to displacement. The topographic phase is eliminated using an external digital elevation model (DEM). Any inaccuracy in the external DEM translates into a phase error in the final interferograms. The displacement and its phase are related using the following formula:

$$\phi = \phi_2 - \phi_1 = \frac{4\pi}{\lambda'} (r_2 - r_1) \quad (1.7)$$

Subscripts 1 and 2 refer to two SAR images acquired at two different times. Accordingly, one complete phase cycle ( $2\pi$ ) corresponds to half a wavelength ( $\lambda'$ ) of displacement; e.g. if the radar system has a wavelength of 6 cm, one fringe is equivalent to 3 cm of deformation in LOS direction. Before conversion of phase to displacement, it should be noted that the resolved phase difference is a wrapped value and a phase unwrapping approach is implemented. In other words, the interferometric phase is a

number between  $[0, 2\pi]$ . The phase unwrapping algorithm starts from a random point in the image and integrates the phase values along a path to retrieve the absolute phase corresponding to each image pixel. Theoretically, phase unwrapping is not affected by the choice of its path. But this condition does not hold everywhere due to decorrelation noise or steep topography (Bamler & Hartl 1998).

The processing of DInSAR data starts by the selection of two images which have a reasonable spatial and temporal baseline. The maximum spatial baseline is on the order of several hundred meters. The correlation between the two complex SAR images decreases with increasing spatial baseline until it completely vanishes. This baseline is known as the critical baseline for flat surfaces (Rodriguez & Martin 1992). However, the maximum temporal baseline is a factor of any change in the ground cell, e.g. land cover change, soil moisture change. The temporal baseline varies from several days to few years. Figure 1.6 demonstrates the different steps of interferometric processing.

The first step of processing is the coregistration of the second image (slave) with respect to the first image (master). After the coregistration, the interferogram is made by subtracting the phase value of the two images using equation (1.5) (Figure 1.6 (a)). Later, different interferometric contributions are subtracted including the flat earth and topographic effects. The resulting image is the interferogram which shows the phase difference due to displacement, assuming that the atmospheric noise is negligible (Figure 1.6 (b)). The next step is the phase unwrapping and conversion of the phase to displacement using equation (1.7) (Figure 1.6 (c)).

DInSAR is sensitive to only the component of the velocity vector in the LOS (in slant range) and not to the component of motion along track. The LOS projection of deformation can be obtained as the scalar product of displacement ( $d$ ) and the DInSAR sensitivity vector ( $u$ ):

$$d_{LOS} = d \cdot u = \begin{bmatrix} d_{east} \\ d_{north} \\ d_{zenith} \end{bmatrix} \begin{bmatrix} u_{east} \\ u_{north} \\ u_{zenith} \end{bmatrix} = \begin{bmatrix} \sin \theta \cdot \cos \alpha \\ \sin \theta \cdot \sin \alpha \\ \cos \theta \end{bmatrix} \quad (1.8)$$

where  $\theta$  is the look angle and  $\alpha$  is the satellite heading angle. It is possible to retrieve more information about the ground movement by analyzing images from different ascending and descending geometries. In that case there will be more observations (LOS) available in order to invert for the three-dimensional components of surface displacement. When the incident angle is higher, the sensitivity to the vertical motion is decreased.

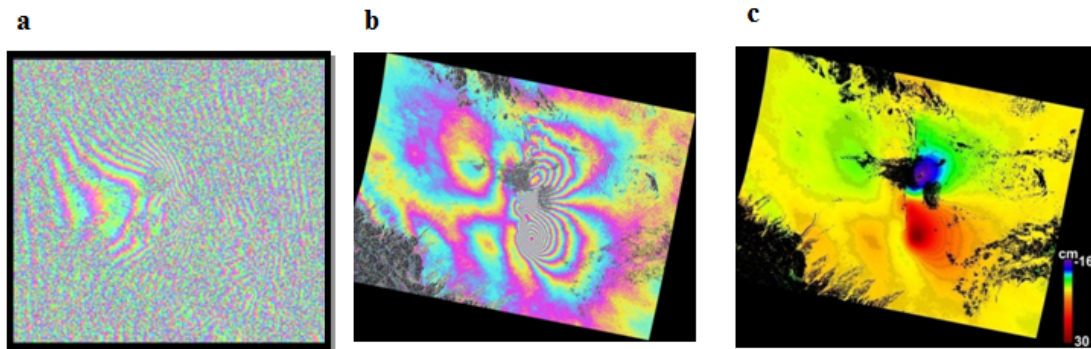


**Figure 1.6 (a) Initial interferograms of Bam earthquake (Mw= 6.5, 26 December 2003) (b) the final interferogram after removal of orbital and topographic contribution and (c) the final displacement map showing the amount of deformation (Motagh et al. 2006).**

### 1.7. Coherency

The interferometric coherence  $\gamma$  can be computed as (Bamler & Hartl 1998),

$$\gamma = \frac{E\{V_1 V_2^*\}}{\sqrt{E\{|V_1|^2\} E\{|V_2|^2\}}} \quad 0 \leq |\gamma| \leq 1 \quad (1.9)$$

where  $E\{ \cdot \}$  represents the expectation value. The module of the interferometric coherence  $|\gamma|$ , called the coherence (Figure 1.7), is a measure of the phase noise of the interferogram, while  $\arg(\gamma)$  is the resulting interferometric phase.

The relationship between the coherence and the phase variance was explored by many authors (Zebker & Villasenor 1992; Joughin et al. 1994; Rodriguez & Martin 1992). This relationship was expressed by Zebker & Villasenor (1992) as

$$\sigma^2 = \frac{1}{NM} \frac{1-\gamma^2}{\gamma^2} \quad (1.10)$$

where  $N$  and  $M$  are the number of looks in range and azimuth direction. In a practical sense, one can form a coherence map from the data and use equation (1.10) to quantify the phase and deformation errors.

Each pixel in a SAR image is composed of several scatterers with different reflectivity and the differential sensor-target path. If these values do not change in the time span between successive radar acquisitions, they are cancelled out from the interferometric phase. This is the basic assumption for carrying out interferometric measurements and corresponds to full coherence. The interferometric coherence can be formulated as a composition of the following contributions (Rodriguez & Martin 1992)

$$\gamma_{total} = \gamma_{processor} \cdot \gamma_{thermal} \cdot \gamma_{temporal} \cdot \gamma_{spatial} \quad (1.11)$$

where  $\gamma_{processor}$  refers to the phase errors introduced by SAR processing; these errors are usually small and  $\gamma_{processor}$  is close to one.  $\gamma_{thermal}$  is dependent on the signal-to-noise ratio of the SAR system.  $\gamma_{spatial}$  expresses the decorrelation due to changes caused by different reflectivity at the two ends of the baseline (Zebker & Villasenor 1992). In the case of pure surface scattering, the decorrelation can be eliminated by filtering of the range spectra (Gatelli et al. 1994). In this regard, optimum slope-adaptive spectral shift filtering can improve further interferogram quality (Bamler & Davidson 1997). Spectral shift increases with terrain slope to the point where it equals the range system bandwidth. Beyond the look angle spectral shift is negative due to layover (Gatelli et al. 1994).  $\gamma_{temporal}$  represents temporal decorrelation caused by changes in the distribution of scatterers within the resolution cell occurring during the time interval between the two acquisitions.

The main limitations for the application of DInSAR over long time intervals result from temporal decorrelation. In densely vegetated areas, such as forests and agricultural lands, the signal usually decorrelates within days. On the other hand, over areas with low vegetation or bare surfaces the signal may remain coherent over several years. The loss of coherence due to vegetation is most significant for short wavelengths (X and C band). Conversely, the longer wavelengths (L band) can penetrate deep into vegetation and result in less volume decorrelation.

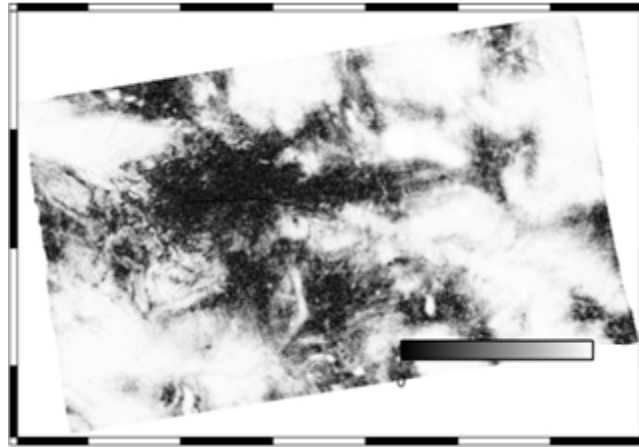


**Figure 1.7. Coherence image of a RADARSAT-2 interferogram from the Ahar 2012 earthquakes.**

### **1.8. Advanced DInSAR Techniques**

There exist a number of advanced DInSAR methods which are widely used to measure deformations of Earth's surface with higher accuracy than conventional DInSAR (Sandwell & Price 1998; Bernardino et al. 2002; Feretti et al. 2001; Hooper et al. 2007). One of the examples of these techniques is stacking (Sandwell & Price 1998), in which averaging over several interferograms reduces the effect of the unwanted signal.

Another widely used technique is the Small Baseline (SBAS) method (Bernardino et al. 2002; Samsonov et al. 2011). This methodology selects interferograms with small spatial and temporal baselines, assuming a minimum effect of decorrelation noise for these interferograms and a constant displacement velocity between subsequent acquisition times. Using Singular Value Decomposition (SVD), this technique solves for the deformation rate between subsequent radar images. Additionally, the residual topographic phase also is formulated as a function of perpendicular baseline and resolved in this technique. Later, the atmospheric phase is removed by applying a high pass filtering in time and low pass filtering in space.

Permanent Scatterer (PS) and Coherent Pixel method (CPM) (Ferretti et al. 2001; Hooper et al. 2007, 2008; Blanco-Sánchez et al. 2008) are also techniques to improve the quality of the interferograms. The idea is to select radar phase stable points within a radar scene, assuming that the effect of decorrelation noise is minimum for these objects. These points, called Pixel Candidates (PC), usually correspond to buildings, metallic objects, exposed rocks and other stable, reflective surfaces that exhibit a constant radar signature over time. After interferogram generation, the phase of the PCs can be decomposed into several contributions including displacement phase, atmospheric phase and residual topographic phase. The least squares method is applied in order to retrieve the absolute phase value corresponding to each radar scene and in the meantime solves for other phase components.

Multibaseline DInSAR techniques need a large number of coherent pixels to work properly (Ferretti et al. 2001). The quality criteria for selecting these coherent targets (Pixel Candidate (PC)) are the average coherence for the full set of interferograms. In this technique, the interferograms are formed and a thresholding is applied over the mean coherence to separate the pixels with the higher coherence value (Blanco-Sánchez et al. 2008). The second criterion is based on the amplitude dispersion index (Ferretti et al. 2001). The amplitude dispersion index is computed for the whole stack of single-look complex images from the following formula:

$$\textit{Amplitude Dispersion Index} = \frac{\delta}{\mu} \quad (1.12)$$

where  $\mu$  is the mean and  $\delta$  is the standard deviation of a pixel in different radar scenes. This value provides an indication about the phase stability of the corresponding pixel.

In the next sections, I will explain how the use of polarimetric information will increase the number of PCs for Advanced DInSAR. An example of this technique is the Polarization Phase Difference (PPD) method (Samsonov & Tiampo 2011) which selects pixels that demonstrate either even or odd bounce scattering properties, using a number of polarimetric images.

## **1.9. SAR Polarimetry**

A radar polarimetric system measures the polarization state of a wave backscattered by the media. The measured polarimetric signal depends on the type of scattering mechanisms (SM), which is a representation for polarization states in the transmitted or backscattered wave.

SAR polarimetry is a technique used for acquiring physical information from different land covers. Previous studies have used polarimetric scattering models to provide information about physical ground parameters such as soil moisture and surface roughness (Hajnsek et al. 2003; Hajnsek et al. 2007). Moreover, the temporal evolution of these observables provides information on the temporal changes of these parameters (Mattia et al. 2003). Unsupervised classification methods of polarimetric data identify different scatterer characteristics and target types (McNairn & Brisco 2004).

### **1.10. Principles of SAR polarimetry**

In satellite radar polarimetry we analyze the shape of the transmitted and received polarization ellipse, as shown in Figure 1.8. This figure shows the spatial helix resulting from a combination of horizontal (H, in green) and vertical (V, in blue) transmitted components. When a radar wave is transmitted in a horizontal polarization and received by horizontal or vertical polarizations, it is called HH or HV channels, respectively. If a

radar wave is transmitted with a vertical polarization and received with horizontal or vertical polarizations, it is called VH or VV channels.

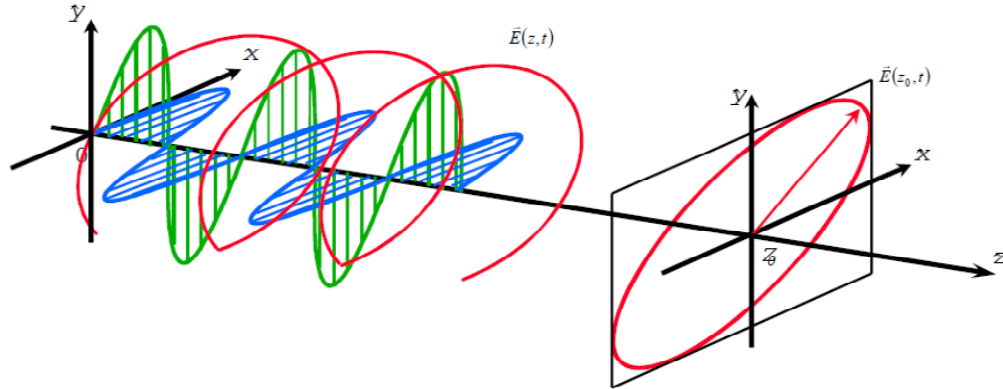


**Figure 1.8. The polarization ellipse decomposed into orthogonal components x (horizontal H) and y (vertical V) (<http://www.nrcan.gc.ca/earth-sciences/geography-boundary/remote-sensing/radar/1968>).**

A radar wave is described using a pair of complex numbers,  $e_x$  and  $e_y$  as shown in the following equation, in any polarimetric basis, corresponding to the horizontal and vertical component of the wave.

$$e_x + e_y \rightarrow E = \begin{bmatrix} e_x \\ e_y \end{bmatrix} \quad (1.13)$$

Fully polarimetric SAR (Pol-SAR) sensors acquire images in various polarimetric channels and ultimately can measure the  $2 \times 2$  scattering matrix,  $S$ , corresponding to the media, as

$$E^s = \frac{e^{jk'r}}{r} \begin{bmatrix} S_i^{HH} & S_i^{HV} \\ S_i^{VH} & S_i^{VV} \end{bmatrix} E^t, \quad (1.14)$$

$E^s$  is the scattered wave and  $E^t$  is the transmitted wave. Here  $r$  is the distance from the satellite to the ground point and  $k'$  is the wave number. The scattering matrix is independent of the transmitted polarimetric basis; it is a function of shape, orientation and dielectric properties of the scatterers. Under the reciprocity theorem, the off-diagonal elements are equal and  $S_{HV} = S_{VH}$ . The scattering matrix is expressed as a scattering vector ( $k$ ) using the Pauli basis as (Cloude & Papathanassiou 1987)

$$k_i = \frac{1}{\sqrt{2}} [S_i^{HH} + S_i^{VV}, S_i^{HH} - S_i^{VV}, 2S_i^{HV}]^T \quad (1.15)$$

SAR polarimetry has the capability of discriminating different types of scattering mechanisms within a resolution cell. The radar targets are categorized as deterministic and distributed targets. Deterministic targets are the point-wise scatterers and distributed scatterers are those composed of a large number of randomly distributed deterministic scatterers. The scattering matrix is able to completely describe deterministic scatterers. However, for the distributed targets, a second-order statistics is required, such as coherency [T] matrix (equation 1.16).

$$T = \langle k k^{*T} \rangle \quad (1.16)$$

where  $^{*T}$  represents conjugate transpose operator and  $\langle \rangle$  is the multilooking factor. Using a multilooking approach the effect of the single scatterers is decreased and the mean value is achieved for a group of pixels.

### 1.11. Polarimetric SAR Interferometry (PolInSAR)

In Polarimetric SAR Interferometry (PolInSAR), Interferometric SAR (InSAR) and polarimetric techniques are coherently combined to provide improved sensitivity to the vertical distribution of scattering mechanisms (Cloude & Papathanassiou 1998). Using the PolInSAR technique, it is possible to extract scatterers at different heights for a given resolution cell.

Coherence is the main observable of PolInSAR. Coherence optimization is a technique which attempts to find the best polarization base transformation corresponding to the scatterer with the maximum coherence (Neumann et al. 2008). When this transformation is applied to fully polarized satellite data, it will result in isolating the most dominant scattering mechanism of the corresponding pixel (Papathanassiou & Cloude 1998; Colin et al. 2006). Dominant scattering mechanisms provide each resolution cell with the highest coherence value.

The advantage of this technique is to increase the component corresponding to the most stable target, which is done by eigenvalue decomposition of the coherency matrices in an optimization solution. The correspondence between the backscattered power and stable radar targets is explained better in Section 1.8, where the amplitude dispersion index is used as a measure to separate the stable radar targets. These points have less spatial and temporal decorrelation noise.

In the previous studies, PolInSAR coherence optimization was employed to increase the number of interferometric coherent pixels for DInSAR studies. This is achieved by finding the optimum scattering mechanisms in a resolution cell through analysis of average target's coherency matrix (Navarro-Sanchez et al. 2010). As we use a number of SAR images for advanced DInSAR analysis, a multibaseline approach must be implemented. A multibaseline approach will guarantee that the scattering mechanism of a SAR image will remain the same between all the interferograms. Otherwise, each SAR image will have a different scattering center corresponding to each interferograms and a noise component will be added to the differential phase. The noise corresponds to the height difference between different phase centers.

There are two approaches to solve the multibaseline coherence optimization problem; Multi-Baseline Equal Scattering Mechanism (MB-ESM) and Multi-Baseline Multiple Scattering Mechanism (MB-MSM). In the case of MB-ESM as proposed by (Neumann et al. 2008), the scattering mechanisms of the images remain the same among all the baselines ( $\omega_i = \omega_j$ ). However, this condition is not met using MB-MSM technique ( $\omega_i \neq \omega_j$ ), and for every acquisition an individual optimal polarization is found which

correlates best to all others. MB-MSM technique can introduce an additional interferometric phase of the DInSAR method. While in reality some physical effects (e.g. change in soil moisture content, incident angle and atmospheric conditions) will modify the scattering mechanisms between acquisitions, leading to temporal decorrelation, the change of scattering mechanism between acquisitions might compensate for the temporal decorrelation in areas of less noise. If there is no meaningful change of the scattering mechanism, the MB-MSM technique may add a component to the interferometric phase. This additional phase component (noise) corresponds to the difference of the phase centers from assumption of the two different scattering mechanisms at two ends of the baseline.

Accordingly, in previous research, the MB-ESM has been applied instead of the MB-MSM technique (Navarro-Sanchez et al. 2010), even though in some cases, the choice of MB-MSM may provide better resolution of the interferometric phase. The technique to solve the coherence optimization problem will be presented in the next section 1.12.

### **1.12. Methodology**

Coherence optimization of polarimetric images is applied to reduce the interferometric phase noise. As mentioned in section 1.7, different components of decorrelation degrade the interferometric phase. PolInSAR coherence optimization is able to reduce the component of volume scattering by selection of an optimum polarimetric channel. In this technique the scattering mechanism corresponding to the highest coherence is retrieved, which insures less interferometric noise. In multibaseline interferometry, as explained before, mean coherence is an estimation of phase noise. Using the coherence optimization approach, the mean coherence over a stack of interferograms will increase. Accordingly, it will result in a higher number of coherent targets.

Here, I will explain in detail the processing steps employed in the multibaseline DInSAR analysis on the polarimetric images.

### **1.12.1. Co-registration**

The co-registration procedure aligns SAR images into the master image geometry. In the first step, the satellite orbits are used for initial image co-registration. A more accurate co-registration is performed by cross-correlation of the intensity images. The peak of the correlation function will resolve the range and azimuth offsets. A number of windows are distributed over the image and offset values for each patch are generated. A least squares polynomial fit is used in order to find the model of the pixel offsets for the entire slave image. Later, resampling of the slave image is performed using a complex sinc interpolator.

The processing starts with the collection of SAR images at different dates ( $i=1$  to  $N+1$ ). Each SAR image has three different polarimetric channels, assuming that the reciprocity theorem holds. The co-registration is performed in two steps. The first step is to co-register three different channels of the master image. In the next step, the remainder of the SAR images are co-registered with the master image of the corresponding polarimetric channel (HH,VV,VH).

### **1.12.2. Baseline Estimation**

The next step of the analysis is to form all the possible pairs between the SAR images. The condition to form an interferogram between two SAR images is dependent on the spatial and temporal baseline. Where these baselines exceed the critical limit, the displacement will be contaminated by decorrelation noise and the interferometric phase will not be reliable. The maximum temporal baseline is dependent on the atmospheric condition, land-cover change, soil moisture change, vegetation growth, etc. and can vary between a few months to several years. The maximum spatial baseline is a function of the look angle and the wavelength and distance from the satellite to the ground.

### **1.12.3. Coherence Optimization**

After the above steps are complete, I perform coherence optimization of the fully polarimetric images (Neumann et al., 2008). Here an Equal Scattering Mechanism (ESM)

optimization is applied in order to constrain the scattering mechanisms to be equal at both ends of the baseline. The optimization solves for the highest mean coherence among all the interferograms, as:

$$\max \sum_j \sum_i |\gamma_{ij(\omega)}| \quad (1.17)$$

$$\text{where } \omega_1 = \omega_2 = \dots = \omega_n$$

$\gamma_{ij(\omega)}$  is the interferometric coherence between images  $i$  and  $j$  corresponding to the scattering mechanism  $\omega$ . In the following equation, equality is achieved when the phase shift ( $\theta_{ij}$ ) is equal to the optimum coherence phase values.

$$\max \sum_{i=1}^n \sum_{j=1}^n \gamma_{ij(\omega)} e^{-i\theta_{ij}} \leq \max \sum_{i=1}^n \sum_{j=1}^n |\gamma_{ij(\omega)}| \quad (1.18)$$

Accordingly, an iterative numerical approach as presented below is applied in order to introduce an optimal phase shift:

$$Hw = \lambda w \quad H = \sum_i \sum_j \Pi_{ij} e^{-i\theta_{ij}} \quad (1.19)$$

$$\Pi_{ij} = T_e^{-1/2} \Omega_{ij} T_e^{-1/2} \quad (1.20)$$

$$T_e = \frac{1}{n} \sum_{i=1}^n T_{ii} \quad (1.21)$$

$$w = \frac{\sqrt{T_e} \omega}{\omega^\dagger \sqrt{T_e} \omega} \quad (1.22)$$

$$\theta_{ij} = \arg(w^\dagger \Pi_{ij} w) \quad (1.23)$$

In these equations, by iteratively changing  $\theta_{ij}$ , we get a better estimation of the optimal phase value. In accordance with Neumann et al., 2008, the optimization is performed as follows:

- 1) Initialization;  $\theta_{ij} = \arg(\text{trace} \Pi_{ij})$ ;  $\lambda = 0$ .
- 2) Derive  $H$  and  $w$ , and solve for the eigenvalue and the corresponding phase shift.
- 3) Improve the estimation of  $\theta_{ij}$ .
- 4) The process stops if the phase shift is below a certain threshold.
- 5) Use  $w$  in order to solve for the  $\omega$ .

The process is performed on a pixel-by-pixel basis. A processing window of  $5 \times 10$

pixels is selected in order to calculate the coherency matrices and the corresponding scattering mechanisms. When these mechanisms are found, they are converted from the linear basis (H,V) to the optimal basis. As a result, for each SAR image, instead of having three channels of (HH,VV,VH) data, one optimized channel is resolved.

#### **1.12.4. Interferogram Generation**

Before interferograms generation, common-band range and azimuth filtering is performed on the SAR images. The two SAR images are acquired from slightly different look angles and the slant range spectra of two images may not overlap completely. Moreover, if the squint angle of the two SAR images is different, there is a difference in the azimuth spectra. These effects will cause decorrelation and the filtering is applied before interferograms generation to remove the decorrelation effect at the price of reduced resolution.

Differential interferogram generation is formed by calculating the phase difference of two SAR images (1.4). The processing window size is consistent with the window size used for the coherence optimization. The choice of a  $5 \times 10$  pixel processing window is made to ensure that enough independent scatterers occur in a given resolution cell and produce an unbiased estimation of coherence (Touzi et al., 1999). For a smaller window size the scatterers might not be independent from each other. Moreover, there is a trade-off between the size of the processing window and spatial resolution. Selecting a small averaging window ensures higher spatial resolution, but biases the coherence estimation towards higher values.

Equations (1.5) and (1.6) are used to remove the topographic component and the flat earth component. Later, I will explain the procedure to remove the residual orbital components and the residual topographic components.

#### **1.12.5. Phase Unwrapping**

The next step in DInSAR analysis is to filter the interferograms to reduce the interferometric phase noise. After the interferometric generation and filtering, the interferograms were unwrapped, using the phase unwrapping technique known as

Minimum Cost Flow (MCF) (Costantini & Rosen, 1999). The steps of the phase unwrapping are as follows:

- 1) A set of coherent points above a certain threshold are selected and connected by a delaunay triangle network.
- 2) The minimum cost flow algorithm is employed in order to connect the residues. A residue is a point in the interferogram where the sum of the phase differences between pixels around a closed path is not 0.
- 3) Unwrapped phases are computed by integration.

The application of PolInSAR coherence optimization will result in different scattering mechanism for the neighboring pixels. However, the effect of polarimetric change from one pixel to another will not significantly change the performance of the phase unwrapping. Assuming that the relative position of the scatterers in a resolution cell does not change significantly, phase unwrapping can be applied to the neighboring pixels from different scattering mechanisms. Accordingly, the coherence optimization solves for the optimized scattering type, which is more stable in time, in order to give better deformation estimation. In the remainder of this research, the mean quality criterion is used for separation of the most stable targets. A coherence threshold of 0.3 is employed to separate the group of coherent and non-coherent pixels as explained in Section 1.8.

#### **1.12.6. Residual Orbital Error Correction**

In cases where there is an inaccuracy in the position of the satellite, there is a systematic error which remains after removal of the flat earth component. The systematic error is a long wavelength fringe pattern across a single interferograms. Removal of residual orbits is performed by fitting a plane to the phase measurements. The coefficients of a bilinear plane are derived using a regression technique, and the synthetic model of orbits is generated and removed from every single interferograms.

### 1.12.7. Multibaseline Analysis

The multibaseline DInSAR approach used in this thesis is the Small BASeline (SBAS) technique developed by Berardino (2002). In this technique only interferograms of small temporal baseline are selected in order to reduce the decorrelation noise. However, by choosing these interferograms, there is a possibility that no common image exists between some interferograms. In this problem, in order to avoid inversion singularity, the Singular Value Decomposition (SVD) technique is employed, as explained below. The technique solves for the residual topographic contribution and employs a Fast Fourier Transform approach to reduce atmospheric artifacts. Since atmospheric errors are long-wavelength features in the interferograms, we employ a low-pass filtering technique to remove these signals. The SBAS technique first performs phase unwrapping to solve for the absolute phase value. Then the unwrapped interferograms undergo a system of equations to retrieve deformation time series using the following procedure.

We assume that there are  $N+1$  images acquired at different times. The number of possible interferograms with small spatial and temporal baseline can be calculated based on the following:

$$\frac{N+1}{2} \leq M \leq N \left( \frac{N+1}{2} \right) \quad (1.24)$$

Accordingly, any phase difference between two SAR images, can be written as:

$$\Delta\phi = \phi_{t_{k+1}} - \phi_{t_k} = \frac{4\pi}{\lambda} (d_{t_{k+1}} - d_{t_k}) \quad (1.25)$$

Where  $d$  is the deformation regarding the time  $t$  or  $t+1$ . Assuming that the deformation at the first SAR image acquisition time is zero, the absolute phase at different SAR image acquisition times is a vector of  $N$  components. We can formulate the above equations in terms of surface velocity as:

$$\Delta\phi = \frac{4\pi}{\lambda} (t_{k+1} - t_k) \cdot V_{t_{k+1}, t_k} \quad (1.26)$$

The vector of unknown values is the velocity between two SAR image acquisitions, assuming the deformation for the first SAR image acquisition is zero, as:

$$v = [V_{t_1}, V_{t_2}, \dots, V_{t_N}] \quad (1.27)$$

The differential phase observations are as following:

$$\Delta\phi = [\Delta\phi_{t_1}, \Delta\phi_{t_2}, \dots, \Delta\phi_{t_M}] \quad (1.28)$$

The matrix form of these set of equations is formulated as:

$$Av = \Delta\phi \quad (1.29)$$

$A$  is the matrix of coefficients, composed of differences in time between SAR images. The solution to this system of equations depends on the number of interferograms and the rank of matrix  $A$ . If the interferograms are such that there is a link between each SAR image, then matrix  $A$  is not rank deficient and the problem can be solved by a least square technique. Otherwise,  $A$  is decomposed as following

$$A = USV^T \quad (1.30)$$

$U$  is an  $M \times M$  orthogonal matrix,  $S$  is  $M \times M$  diagonal matrix and  $V$  is orthogonal  $N \times M$  matrix. The solution is identified by minimum norm of the velocity (unknown) values.

Additional to the velocity vectors ( $v$ ), it is possible adding additional terms in order to remove the residual topographic errors ( $\delta Z$ ).

$$[A \ C][v \ \delta Z]^t = \Delta\phi \quad (1.31)$$

$$C = \left[ \frac{4\pi}{\lambda \left( \frac{B_{1\perp}}{R \sin(\theta)} \right)} \dots \frac{4\pi}{\lambda \left( \frac{B_{M\perp}}{R \sin(\theta)} \right)} \right]$$

In order to simplify the inversion, we can reduce the deformation rates only to a linear term. Accordingly, the problem is a linear regression to the observations, where we can simultaneously solve for the residual topographic errors. For this regression problem we derive the standard deviation of the observations from the model. In chapter 4, I will use this standard deviation as a measure to compare the performance of PolInSAR technique versus standard interferometry.

### 1.13. Purpose of study

The primary objective of my thesis is to develop tools aimed at increasing the usefulness of DInSAR measurements in modeling and understanding of earth processes by improving its accuracy and precision. This is achieved by incorporating fully polarimetric RADARSAT-2 data into the analysis and integrating this polarimetric

information with the DInSAR technique in Polarimetric SAR Interferometry (PolInSAR). A secondary objective was achieved through the application of a standard DInSAR analysis to the Ahar double earthquakes (August 11, 2012), in order to understand the patterns of stress accumulation and release associated with the ruptured fault. Unfortunately, fully polarimetric data was unavailable for this region, but this study has important implications for future seismic hazard assessments because the event occurred in the proximity North Tabriz Fault (NTF), the largest and the most hazardous strike-slip structure in NW Iran. Understanding the Ahar fault structure and its pattern of stress accumulation provides insights into its impact on the seismic activity of the regional faults. The limitations of this study inherent in the higher decorrelation arising from the standard InSAR method provide an important example of the necessity for employing polarimetric data.

I pursued these goals through the following studies:

- Measuring co-seismic deformation of Ahar earthquake using standard mode RADARSAT-2 interferograms. Advanced inversion methodologies were implemented in order to model the ruptured fault plane.
- Developing a general framework to exploit newly available polarimetric information of RADARSAT-2 in order to increase the number of coherent pixels for DInSAR analysis and assessing the accuracy of their interferometric phases.
- Application of the PolInSAR coherence optimization technique to the Hayward fault (San Francisco) in order to better assess the creep rate along this fault; measuring the velocity of the landslides on Berkeley hills and comparison of the deformation maps with the conventional DInSAR deformation.

#### **1.14. Organization of work**

This integrated thesis is presented in six chapters. The introductory chapter (Chapter 1) outlines the problem addressed and specific objectives of this work. Chapter 2 presents

the analysis of the Ahar double earthquakes derived from the standard DInSAR analysis. Chapter 3 presents the results of the PolInSAR coherence optimization and shows the improvements in terms of Pixel Candidates (PCs) and higher interferometric phase precision. Chapter 4 presents a detailed application of the PolInSAR technique for the Hayward fault and investigates the landslide motion in the Berkeley Hills. Finally, Chapter 5 presents the concluding remarks and suggestions for future research.

### 1.15. References

- Ahmed, S., Warren, H. R., Symonds, D. & Cox, R. P. 1990. The Radarsat system. *IEEE Trans. Geosci. Remote Sens.* **28**, 598-602
- Amelung, F. *et al.* 1999. Sensing the ups and downs of Las Vegas: InSAR reveals structural control of land subsidence and aquifer-system deformation. *Geology*, **27**, 483-486
- Bamler, R. & Davidson, G. W. 1997. Multiresolution signal representation for phase unwrapping and interferometric SAR processing. *Int. Geosci. Remote Sens. Symp. (IGARSS)*, Singapore, 865-8
- Bamler R. & Eineder, M. 1996. ScanSAR processing using standard high precision SAR algorithms. *IEEE Trans. Geosci. Remote Sens.* **34**, 212-18
- Bamler, R & Hartl, P. 1998. Synthetic aperture radar Interferometry. *Inverse Probl.* **14**, 1- 54
- Berardino, P. *et al.* 2002. A New algorithm for surface deformation monitoring based on small baseline differential SAR interferograms. *IEEE Trans. Geosci. Remote Sens.*, **40**, 2375-2383
- Blanco-Sánchez, P. *et al.* 2008. The Coherent Pixels Technique (CPT): and advanced DInSAR technique for non linear deformation monitoring. *Pure appl. Geophys.*, **165**, 6, 1167-1193

Carnece, C. & Delacourt, C. 2000. Three years of mining subsidence monitored by SAR interferometry, Gardanne, France. *App. Geophys.*, **43**, 43-54

Carrara, W. G., Goodman, R. S. & Majewski, R. M. 1995. Spotlight Synthetic Aperture Radar: Signal Processing Algorithms. *Boston, MA: Artech House*

Cloude, S. R. & Papathanassiou, K. P. 1998. Polarimetric SAR Interferometry. *IEEE Trans. Geosci. Remote Sens.*, **36**, 5, 1551-1565

Colin, E. *et al.* 2006. An interferometric coherence optimization method in radar polarimetry for high-resolution imagery. *IEEE Trans. Geosci. Remote Sens.*, **44**, 1, 167-175

Curlander, J. C. & McDonough, R. N. 1991. Synthetic Aperture Radar: Systems and Signal Processing. *New York: Wiley*

Cumming, I. G. & Wong, F. H. 2005. Digital Processing of Synthetic Aperture Radar Data: Algorithms and Implementation. *Norwood, MA: Artech House*

Elachi, C. 1987. Spaceborne Radar Remote Sensing: Applications and Techniques. *New York: IEEE Press*, **255**

Ferretti, A. *et al.* 2001. Permanent Scatterers in SAR Interferometry, *IEEE Trans. Geosci. Remote Sens.*, **39**, 1

Freeman, A. 1992. SAR calibration: An overview. *IEEE Trans. Geosci. Remote Sens.*, **30**, 6, 1107-1121

Gatelli, F. *et al.* 1994. The wavenumber shift in SAR Interferometry. *IEEE Trans. Geosci. Remote Sens.*, **32**, 855-65

González, P. J., Tiampo, K. T., Palano, M., Cannavó, F., Fernández, F. 2012. The 2011 Lorca earthquake slip distribution controlled by groundwater crustal unloading. *Nature Geoscience.*, **5**, 821-825

Goodman, J.W. 1976. Some fundamental properties of speckle. *Journal of the Optical Society of America*, **66**, 11, 1145-1150

Hanssen, R. F. 2001. Radar Interferometry: Data Interpretation and Error Analysis. *Kluwer Academic Publishers, Dordrecht*, 308

Hajnsek, I. *et al.* 2007. Potentials and limitations of estimating soil moisture under vegetation cover by means of PolSAR. *Proceedings of the 5<sup>th</sup> International Symposium on Retrieval of Bio- and Geophysical Parameters from SAR Data for Land Applications*, Eur. Space Agency, Bari, Italy

Hajnsek, I., Pottier, E. & Cloude, S. R. 2003. Inversion of surface parameters from polarimetric SAR. *IEEE Trans. Geosci. Remote Sens.*, **41**, 4, 727-744

Hooper, A. *et al.* 2007. Persistent Scatterer InSAR for Crustal Deformation Analysis, with Application to Volcán Alcedo, Galápagos, *J. Geophys. Res.*, **112**, B07407, doi:10.1029/2006JB004763

Joughin, I. R., Winebrenner, D. P. & Percival, D. B. 1994. Probability density functions for multi look polarimetric signatures. *IEEE Trans. Geosci. Remote Sens.* **32**, 562-74

Massonnet, D. & Rabaute, T. 1993. Radar interferometry: limits and potential. *IEEE Trans. Geosci. Remot. Sens.* **31**, 455-464

Massonnet, D. *et al.* 1995. Deflation of Mount Etna monitored by spaceborne radar Interferometry. *Nature*, **375**, 567-570

Massonnet, D. & Feigl, K. L. 1998. Radar interferometry and its application to changes in the earth's surface. *Rev. Geophys.* **36**, 441-500

Manconi, A. *et al.* 2010. On the effects of 3-D mechanical heterogeneities at Campi Flegrei caldera, southern Italy. *J. Geophys. Res.*, **115**, B08405, doi :10.1029/2009JB007099.

Mattia, F., *et al.* 2003. Multitemporal C-band radar measurements on wheat fields. *IEEE Trans. Geosci. Remote Sens.*, **41**, 7, 1551-1560

McNairn, H. & Brisco, B. 2004. The application of C-band polarimetric SAR for agriculture: A review. *Can. J. Remote Sens.*, **30**, 3

Moreira, A. *et al.* 2013. A tutorial on Synthetic Aperture Radar. *IEEE Geosci. Remote Sens. Magazine*, Microwaves and Radar Institute of the German Aerospace Center (DLR), Germany

Motagh, M., *et al.* 2006. Combination of precise leveling and InSAR data to constrain source parameters of the Mw= 6.5, 26 December 2003 Bam earthquake. *Pure appl. Geophys.*, **163**, 1, 1-18

Navarro-Sanchez, V.D., Lopez-Sanchez, J. M. & Vicente-Guijalba, F. 2010. A Contribution of Polarimetry to Satellite Differential SAR Interferometry: Increasing the Number of Pixel Candidates. *IEEE Trans. Geosci. Remote Sens. Lett.*, **7**, 2, 276-280

Neumann, M. *et al.* 2008. Multibaseline polarimetric SAR interferometry coherence optimization. *IEEE Geosci. Remote Sens. Lett.*, **5**, 1, 93-97

Oliver, C. & Quegan, S. 2004. Understanding Synthetic Aperture Radar Images. Herndon, VA: SciTech Publishing

Rodriguez, E. & Martin, J. M. 1992. Theory and design of interferometric synthetic aperture radars. *IEEE Proceeding*, **139**, 147-59

Samsonov, S & d'Oreye, N. 2012. Multidimensional time series analysis of ground deformation from multiple InSAR data sets applied to Virunga Volcanic Province, *Geophys. J. Int.*, **191**, 3, 1095-1108, doi: 10.1111/j.1365-246X.2012.05669.x

Samsonov, S & Tiampo K. 2011. Polarization phase difference analysis for selection of persistent scatterers in SAR Interferometry. *IEEE Geosci. Remote Sens. Lett.*, **8**, 2, 331-335

Samsonov, S., van der Kooij, M & Tiampo, K. F. 2011. A simultaneous inversion for deformation rates and topographic errors of DInSAR data utilizing linear least square inversion technique. *Computers & Geosciences*, **37**, 8, 1083-1091

Sandwell, D. T. & Price, E. J. 1998. Phase gradient approach to stacking interferograms. *J. Geophys. Res.: Solid Earth*, **103**, B12, 30183-302

Short, N., Brisco, B. & Murnaghan, K. 2012. Monitoring permafrost environments with InSAR and polarimetry, case studies from Canada. *Geosci. Remote Sens. Sym. (IGARSS)*, 4034-4037, doi:10.1109/IGARSS.2012.6350524

Tiampo, K.F., Ouegnin, F. A., Valluri, S., Samsonov, S., Fernández, J. & Kapp, G. 2012. An Elliptical Model for Deformation Due to Groundwater Fluctuations. *Pure appl. Geophys.*, **169**, 8, 1443-1456

Touzi, R., Lopes, A., Bruniquel, J. & Vachon, P. W. 1999. Coherence estimation for SAR imagery. *IEEE Trans. Geosci. Remote Sens.*, **37**, 1, 135-149

Vasco, D. W. *et al.* 2008. Reservoir monitoring and characterization using satellite geodetic data: Interferometric synthetic aperture radar observations from the Krechba field, Algeri. *Geophys.*, **73**, 6, doi:10.1190/1.2981184

Wiley, C. 1985. Synthetic aperture radars: A paradigm for technology evolution. *IEEE Trans. Aerosp. Electron. Syst.*, **21**, 3, 440-443

Zebker, H. A. & Villasenor. J. 1992. Decorrelation in interferometric radar echoes, *IEEE Trans. Geosci. Remote Sens. Lett.*, **30**, 5

## Chapter 2

### 2 Source model for the 2012 Ahar double earthquakes, Iran, from DInSAR analysis of RADARSAT-2 imagery<sup>1</sup>

*In this chapter, we present the results of a DInSAR application on the Ahar double earthquakes ( $M_w=6.4$  and  $6.2$ ) in northwest Iran. This is the first time that these earthquakes have been studied using geodetic data. Here, we used a pair of RADARSAT-2 images in order to produce the coseismic surface deformation map. We applied advanced inversion techniques to find the geometry of the ruptured fault plane. We tested the hypothesis that two earthquakes ruptured the same fault plane against the hypothesis that they ruptured different fault planes. Our analysis shows that the two earthquakes occurred on a single fault structure. The results of this study provide us with a better understanding of stress accumulation and release in northwest Iran.*

---

<sup>1</sup> This manuscript has been submitted to the Geophysical Journal International

## 2.1. Introduction

The tectonics of NW Iran is dominated mainly by the convergence of Arabia and Eurasia plates at a rate of ~17mm/year (Jackson & McKenzie 1984). The North Tabriz Fault (NTF) is the main strike-slip fault in this region. It transfers tectonic stress from the Alborz range in the south Caspian Sea to the North Anatolian range in the west (Figure 2.1). Based on the geodetic observations, the NTF accommodates right-lateral interseismic slip rate of 8 mm/year (Masson et al. 2007). In addition to the strike-slip mechanism, velocity vectors show extension further north from NTF and in the Talesh block. This extensional kinematics is not explained by the convergence of Arabia and Eurasia plates. Subduction of the South Caspian Sea beneath central Caspian is most probably the driving force behind this motion (Reilinger et al. 2006; Jackson et al. 2002). Numerical models in this region express that additional forces such as slab pull are required to explain the extension between NTF and Talesh blocks (Vernet & Cherry 2006). The occurrence of earthquakes at depth of 30-75 km in this region confirms a northward dipping subduction (Jackson et al. 2002).

On August 11, 2012, northwest Iran was struck by two consecutive earthquakes at 12:23 and 12:34 UTC with moment magnitudes estimated 6.4  $M_w$  and 6.2  $M_w$ , respectively, by the US Geological Survey (USGS). The epicenters were located at 38.358°N, 46.812°E and 38.390°N, 46.741°E, respectively, approximately 20 km southwest of Ahar city and 50 km northwest of Tabriz city, the most populated metropolitan area in northwest Iran. The earthquakes resulted in widespread property damage, more than 300 casualties, and the total destruction of twenty villages. Figure 2.1 shows the location of the two events and the associated aftershock distribution. Vectors illustrate the interseismic velocities of local GPS stations with respect to central Iran from 2002-2004 (Masson et al. 2007). According to the focal mechanism solutions by the Global Centroid-Moment-Tensor (GCMT), the first event ruptured a strike slip fault with a small dip slip component and the second event ruptured an oblique-slip fault with mainly thrust component. A field survey conducted by the Iran Geological Survey (IGS)

found evidence of horizontal and vertical surface displacements of 65 cm and 25 cm, respectively (<http://supersites.earthobservations.org/ahar.php>). The resolved fault plane solution for the first event strikes roughly east-west and dips 80 degrees. One of the nodal fault planes for the second event strikes 256 degrees and dips 65 degrees. The aftershock distribution and the geomorphology of the region support a north dipping, east-west striking fault geometry.

Here we use Differential Interferometric SAR (DInSAR) analysis to invert for the ruptured fault planes and derive associated slip distribution models in order to better understand the interrelationship between the two events and gain a better understanding of the local and regional stress release. In the next section we will describe about the data and details of DInSAR processing. In section 2.3, we will present the results for fault modeling. Section 2.4 and 2.5 will present Coulomb stress results and further discussions, respectively.

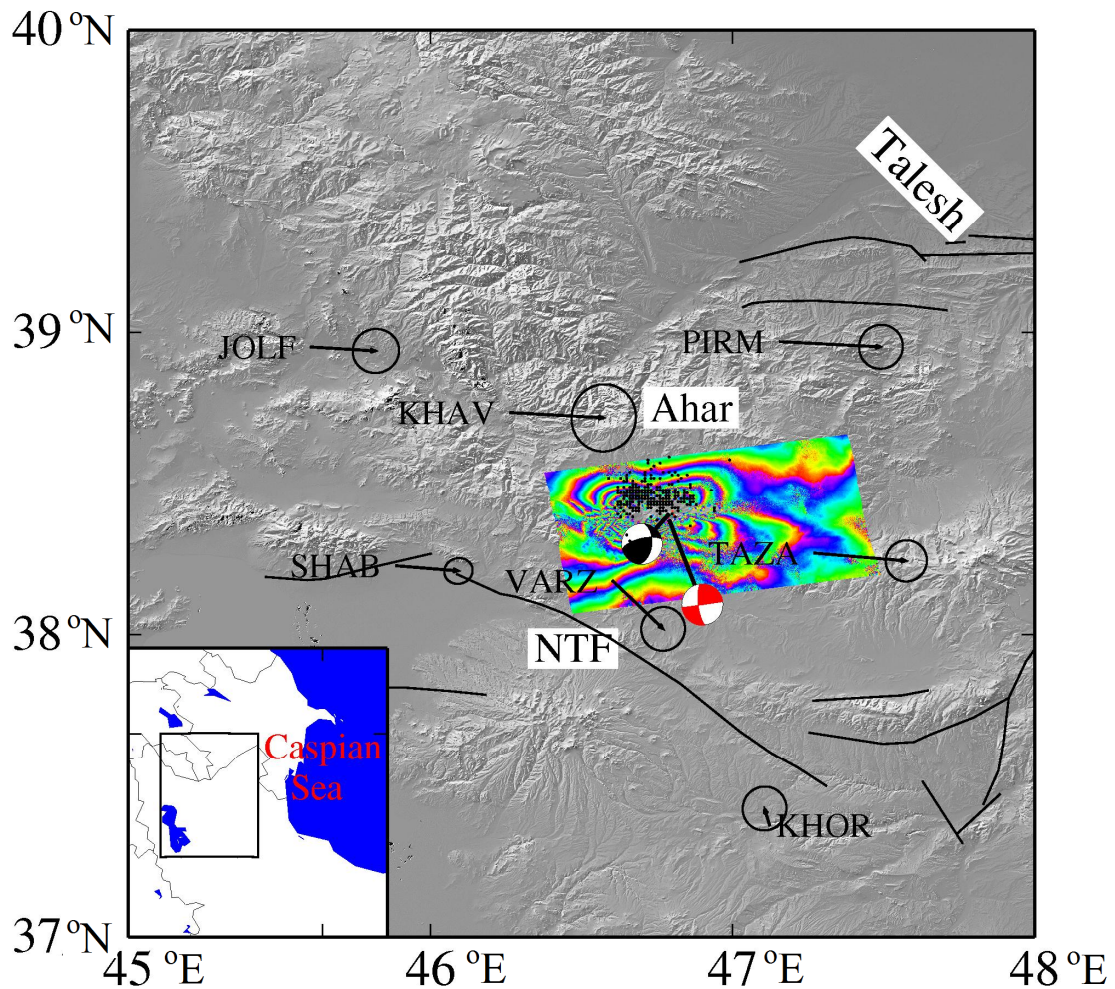


**Figure 2.1. The location of August 11, 2012 Ahhar earthquakes and the corresponding focal mechanisms from Global CMT solutions. The aftershocks are recorded by IIEES (<http://www.iiees.ac.ir/English/>). The vectors are the GPS velocities with respect to the Central Iran block (Masson et al. 2007). NTF represents the North Tabriz Fault. The inset shows the location of our study area within the northwest Iran.**

## 2.2. DInSAR data

Differential Interferometric Synthetic Aperture Radar (DInSAR) is a technique for measuring ground deformation induced by natural or man-made processes (Massonnet & Feigl 1998; Bamler & Hartl 1998). DInSAR has the advantage of mapping an area of hundreds of square kilometers with high spatial and temporal resolution. The technique has been proved to be a powerful tool to measure deformation with centimeter accuracy over periods of days or years. DInSAR has been used for monitoring volcano dynamics (Massonnet et al. 1995; Manconi et al. 2010), coseismic displacements (Massonnet et al. 1993), subsidence due to exploitation of ground-water and oil/gas (Amelung et al. 1999) and mining subsidence (Carnec & Delacourt 2000). Recently this technique is used for monitoring of deformation associated with carbon sequestration and the melting of permafrost (Vasco et al. 2008; Short et al. 2012). Multi-baseline DInSAR technique have also been developed which are able to measure with milometer accuracy by using a larger number of SAR images (Sandwell & Price 1998; Feretti et al. 2001; Hooper et al. 2007; Berardino et al. 2002).

We apply DInSAR technique in order to measure the surface deformation from Ahar earthquakes. We used a pair of RADARSAT-2 images of fine-quad mode acquired on 13 April 2012 and 4 September 2012, to measure the deformation of August 2012 earthquakes. These scenes were processed using GAMMA (Wegmuller & Werner 1997) to form an interferogram with spatial normal baseline of 95 meters. Topographic phase was removed with the 90m Shuttle Radar Topography Mission (SRTM) DEM (Farr et al. 2007), then the interferogram was filtered (Goldstein & Werner 1998) and unwrapped using Minimum Cost Flow (MCF) (Costantini & Rosen 1999). A quadratic (bilinear) function (ramp) is removed to account for satellite orbit uncertainty. Figure 2.1 displays the produced interferogram featuring the coseismic signal. We removed the phase offset of the interferograms by assigning zero deformation to a low elevation region in the east where is not affected by the coseismic signal. Figure 2.2 shows the deformation map from the interferograms which has both the orbital and deformation component.

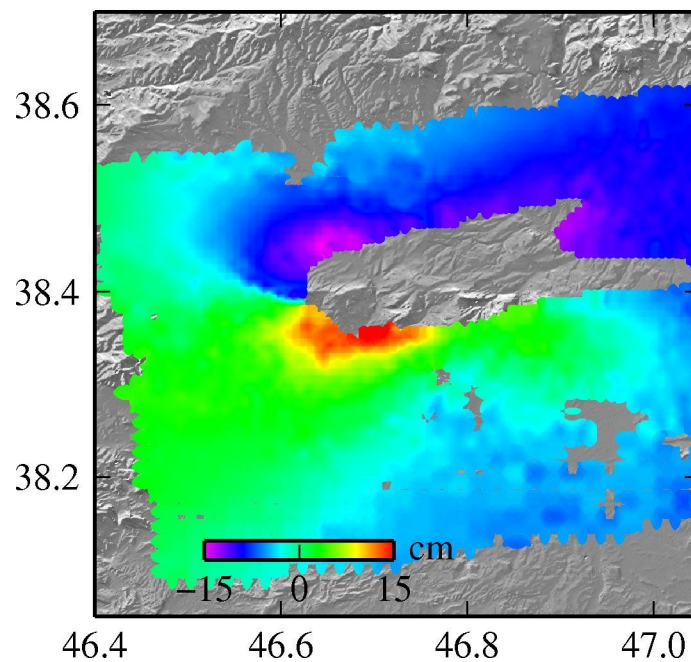


**Figure 2.2. Observed DInSAR deformation without orbital errors removed.**

The interferogram in Figure 2.1 is affected by decorrelation noise in area of the highest deformation, mainly caused by high fringe rates. Due to the lack of measurements in this region, we performed azimuth offset analysis. Azimuth offset analysis solves for the deformation by cross-correlating the amplitude images in the azimuth direction (Strozzi et al. 2002). However, the accuracy of azimuth offset products is only a fraction of the pixel spacing, much less than DInSAR product. Accordingly, the deformation signal should be large enough to be captured by this technique. Here our analysis to measure azimuth offset products was inconclusive due to the lower fringe density which makes the deformation rate below the sensitivity limit for this technique. The necessary condition for Interferometry implies maximum detectable deformation gradient is one fringe per pixel (Massonnet & Feigl, 1998). The Azimuth offset products have been found more informative when a shallow earthquake leaves a higher deformation on the ground

surface example of which is the 2003, 6.6  $M_w$  Bam earthquake (Funning et al. 2005; González et al. 2009).

### **2.3. Slip model from DInSAR technique**

The DInSAR deformation was used to derive the source models for the double earthquakes. Here, we started modeling the two earthquakes using a single elastic dislocation formulation in a half-space (Okada 1985; 1992) for modeling the ruptured fault. For the inversion scheme, we first applied a nonlinear approach which solves for a single uniform slip fault plane. This gives basic information about the location, geometry and the amount of slip on the fault. Later, we use this geometry and apply a distributed slip model to find the details of the slip pattern on the modeled plane. Furthermore, we will investigate the possibility that the two events occurred on two separate fault planes.

The best fitting single fault uniform slip model was derived using a genetic algorithm (GA) technique. A GA is a nonlinear optimization technique which is inspired by the process of natural evolution (Holland 1975; 1992; Tiampo et al. 2000; Sen & Stoffa 1992; Winchester et al. 1993). GA optimization starts by randomly forming a population of candidate solutions corresponding to the unknown parameter and evolves to a best solution through an iterative approach where the best candidates are altered or combined to form the population of solutions for the next iteration. The criterion for solution goodness is the misfit between the observations and the synthetic model. This process ends when the best solution in terms of model fitness to the observations is achieved.

We impose prior knowledge of Ahar earthquake on this inversion in order to narrow down the model parameter search space. Based on IGS reports (<http://supersites.earthobservations.org/ahar.php>), surface ruptures were observed on the ground, implying that the fault was not buried. As a result, we constrain the inversion to solve for a fault that reaches the surface and slip propagates to shallow depths. Another constraint on this inversion was to impose the sense of slip to be right-lateral and thrust based on the focal mechanisms solutions. We ran the GA inversion thirty times, to get a

distribution of the resolved parameters. The resolved fault plane parameters with the associated errors are listed in Table 2.1.

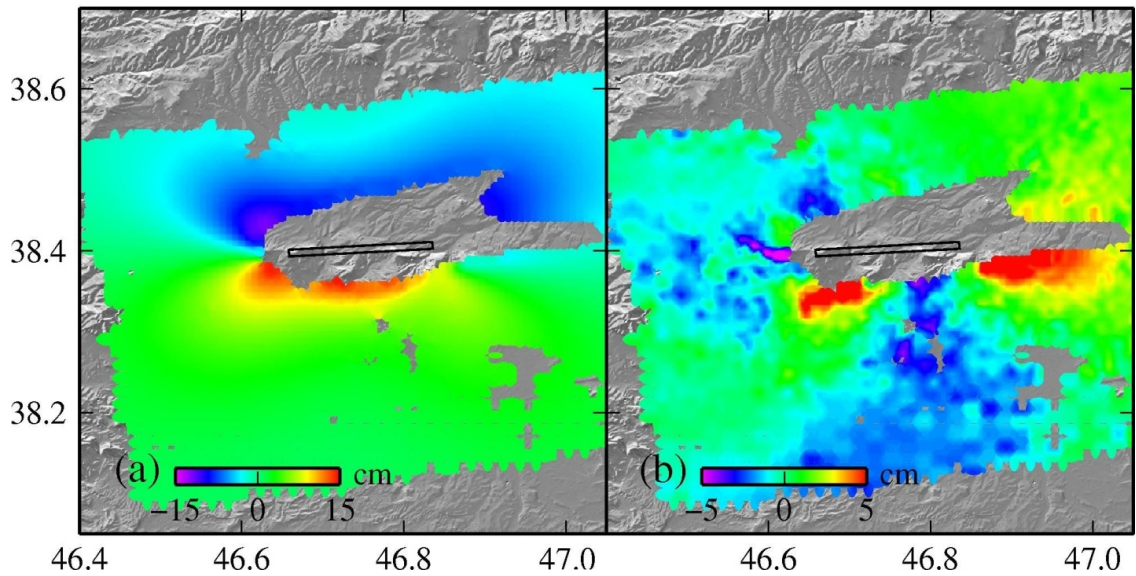


**Figure 2.3. (a) Modeled displacement and (b) residual displacement from the GA solution for a single fault with a uniform-slip model. The surface expression of the modeled dislocations is shown by a black rectangle.**

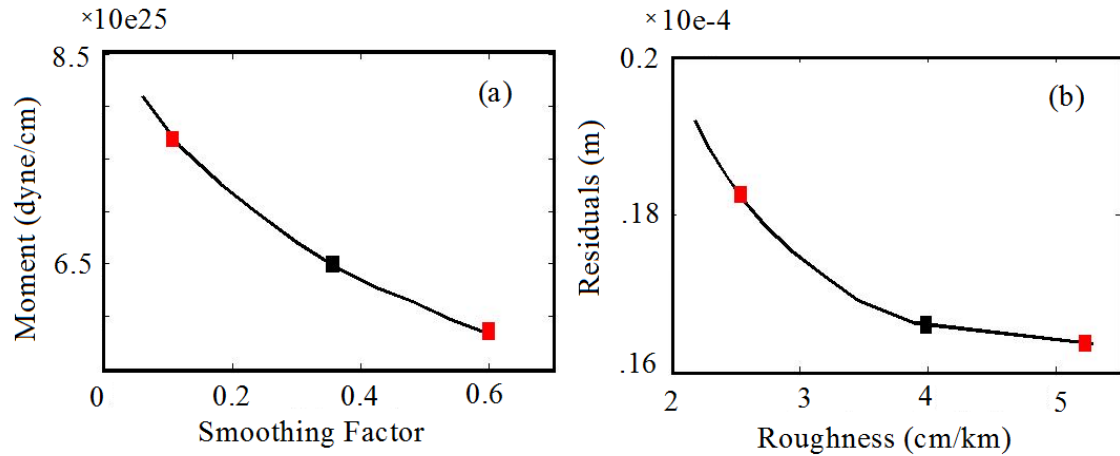


**Figure 2.4. (a) Moment magnitude versus smoothing factor and (b) model roughness versus model residuals. The black square mark the location of the optimum smoothing factor and the red squares mark two examples of extreme smoothing factors considered for comparison.**

**Table 2.1. Source parameters and the associated errors for a single fault derived from the GA inversion**

	Strike	Dip	Length (km)	Width (km)	Depth (km)	Strike Slip (cm)	Dip Slip (cm)
Parameter	263°	85°	15.5	10.5	12	128	25
Parameter Errors	±3°	±2°	±0.4	±0.5	±0.5	±5	±3

As seen in Table 2.1, the amplitude of the dip-slip component is very small in comparison with the strike-slip component. This is consistent with the GCMT focal mechanisms solution of the first event, which was the larger event and primarily a right-lateral strike-slip earthquake. Based on the earthquake magnitude relationship for fault area and slip (Wells & Coppersmith 1994), the geodetic moment of this model is estimated at  $6.6e+25$  dyne/cm which is equivalent to 6.5  $M_w$  event. Note that the magnitude of the cumulative moment for the double earthquakes is 6.48  $M_w$ . This model overestimates the cumulative seismic moment magnitude from the twin earthquakes by 10%. Assuming that the DInSAR error is 1 cm, the  $\chi^2$  test value for this model is 2.6.

Figure 2.3 (a-b) shows the modeled deformation and the corresponding residuals for this uniform slip plane. The rectangle outlines the surface projection of the fault. This model is a rough approximation of the deformation field of the ruptured fault, with localized residuals on the order of 15 cm in the most near-field region. Not unexpectedly, the deformation field is not completely represented by a single uniform-slip fault, prompting us to investigate a distributed-slip model in order to more accurately describe the observed surface displacements.

To obtain a detailed model for the ruptured plane, we performed a distributed slip inversion which solves for the slip on the geometry described above (Table 2.1). We assume that the uniform slip fault is only an initial approximation of the solution. Accordingly, the geometry derived from GA solution was discretized into patches of 3 km size in length and width, where each patch has a strike and dip slip component to be found in a process of linear inversion as described below. The observed surface displacements  $d$  are related to slip components  $m$  as a function  $G$ :

$$d = Gm + \varepsilon \quad (2.1)$$

where  $G$  is the Green's function and  $\varepsilon$  is the observational error. As mentioned earlier, this is a linear inversion and our aim is to find the slip model ( $m$ ) that minimizes the L2-norm of the misfit function,  $\phi'$ :

$$\phi' = ||d - Gm||_2 \quad (2.2)$$

To derive a realistic slip distribution pattern, we apply the Laplacian smoothing criteria (Tikhonov & Arsenin 1977; Beavan et al. 2011; González et al. 2012) and boundary conditions on the modeled slip by constraining the displacement at the borders of the fault to be zero, except for the surface. The smoothing criterion is applied by minimizing the two-dimensional second derivative of the slip pattern. We include smoothing by solving for the following set of equations:

$$\begin{bmatrix} d \\ 0 \end{bmatrix} = \begin{bmatrix} G \\ k^2 D \end{bmatrix} m, \quad (2.3)$$

where  $D$  is a second-order finite difference operator.  $k^2$  is the weight of smoothing. The smoothing parameter  $k^2$  depends on data weighting and on the number of data points (Jónsson et al. 2002). We also use surface roughness as another indicator of smoothness for the slip model in order to better determine the smoothing value. The solution roughness ( $\rho$ ) is calculated as:

$$\rho = \frac{\sum_i |p_i|}{2N} \quad (2.4)$$

where  $p = Dm$  and  $N$  is the number of fault patches.

The smoothing value ( $k^2$ ) must be set appropriately to give a realistic slip model. In finding the best smoothing value, there is a tradeoff between a detailed model (lower residuals) and released moment (Bürgmann et al. 2002). By choosing a lower smoothing value, a more detailed slip model is derived with lower residuals, but the released moment is higher. A higher smoothing value results in a smoother model with higher residuals and smaller moment. For this purpose, we run the inversion with different smoothing factors ranging between [0.05 0.6]. For each run, we invert for the fault slip and the orbital trend parameters which are defined by three coefficients. Figure 2.4 shows (a) moment magnitude versus smoothing factor and (b) model roughness versus model residuals. The corner point in these plots which correspond to the smoothing factor of 0.38 (roughness of 4), is chosen as an optimum value. As mentioned earlier, different smoothing values cause the details of the model to vary. To better investigate the

variation in the slip model, we chose two extreme smoothing values of 0.1 and 0.6, as noted in Figure 2.4. Results are detailed later in this section.

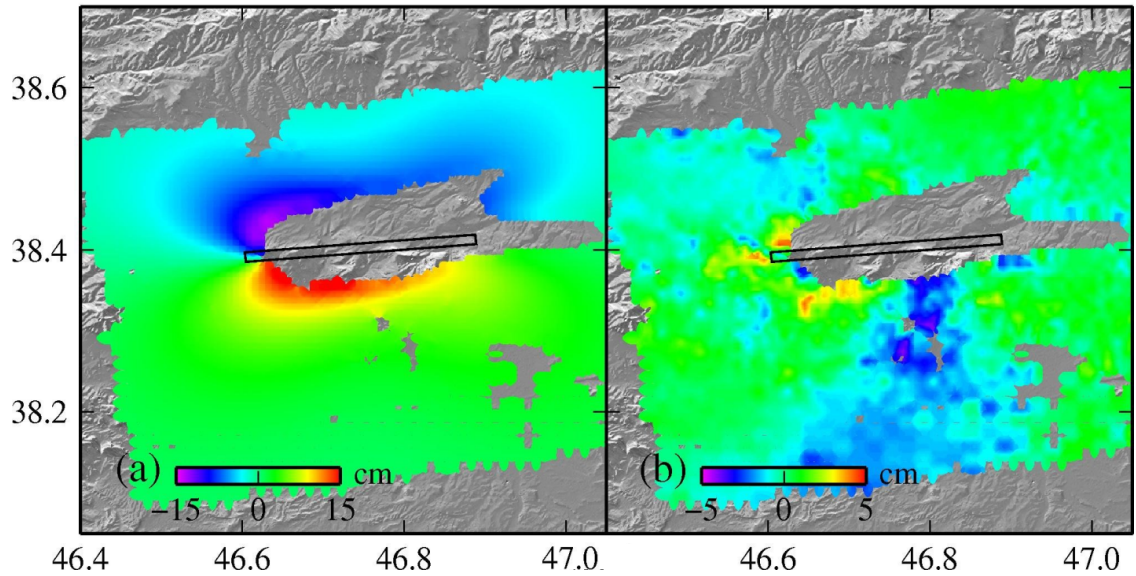


**Figure 2.5. (a) Modeled displacement and (b) residual displacement on a single fault using a distributed-slip model (smoothing factor of 0.38). The surface expression of the modeled dislocations is shown by the black rectangle.**

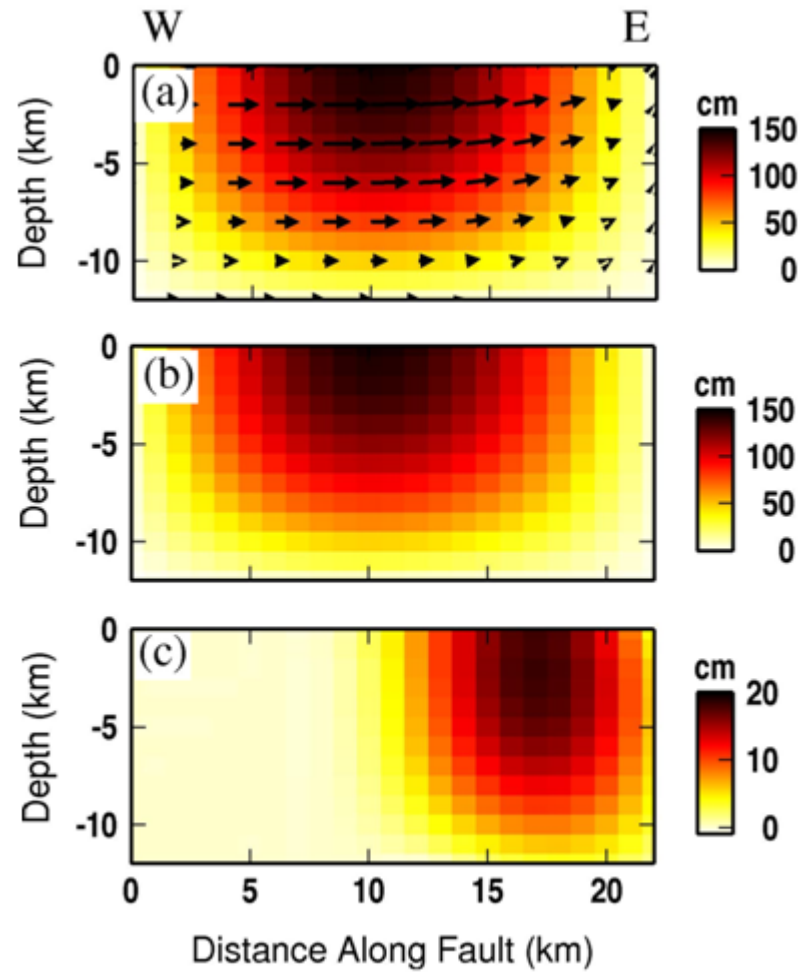


**Figure 2.6. (a) Oblique slip, (b) strike slip and (c) dip slip on a single fault using a distributed slip model and smoothing factor of 0.38. The surface expression of the fault is shown in Figure 2.5.**

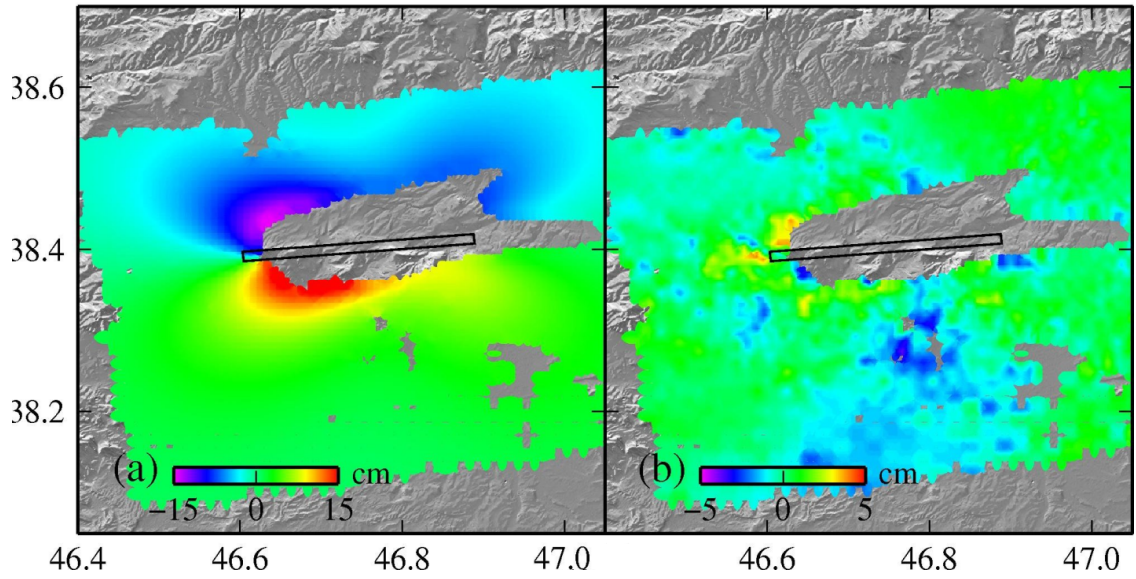


**Figure 2.7. (a) Modeled displacement and (b) residual displacement on a single fault using a distributed-slip model and a smoothing factor of 0.1. The surface expression of the modeled dislocations is shown by a black rectangle.**

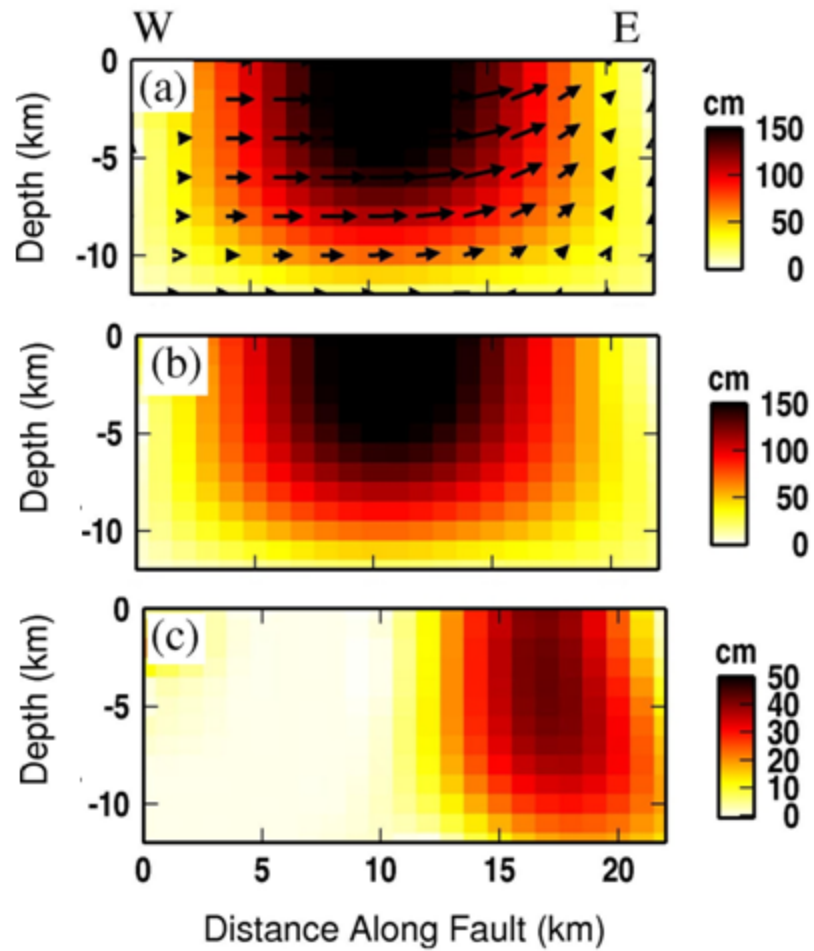


**Figure 2.8. (a) Oblique slip, (b) strike slip and (c) dip slip on a single fault using a distributed slip model and a smoothing factor of 0.1. The surface expression of the fault is shown in Figure 2.7.**

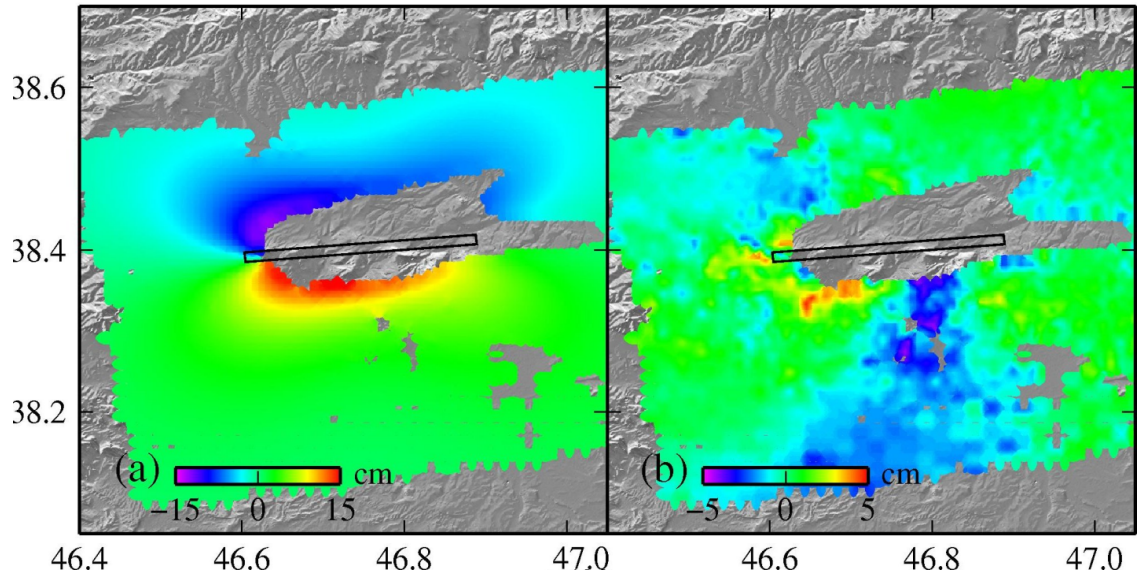


**Figure 2.9. (a) Modeled displacement and the (b) residual displacement on a single fault using a distributed-slip model and a smoothing factor of 0.6. The surface expression of the modeled dislocations is shown by a black rectangle.**

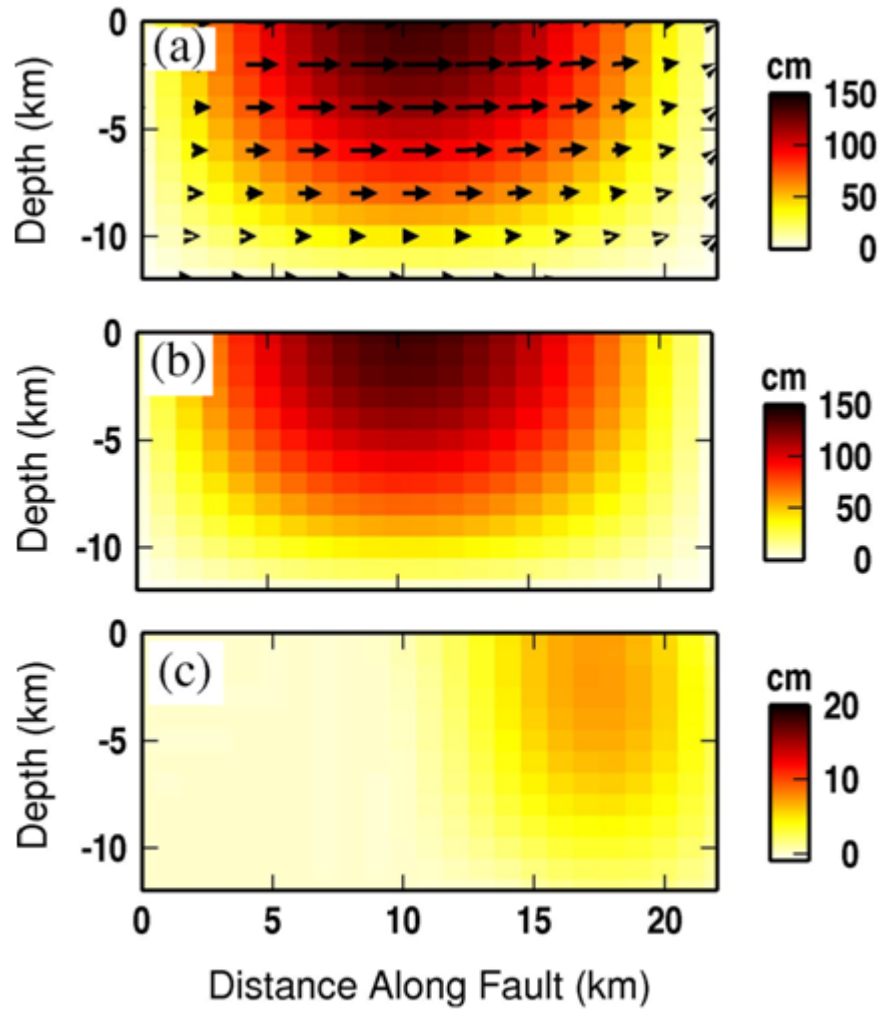


**Figure 2.10. (a) Oblique slip, (b) strike slip and (c) dip slip on a single fault using a distributed slip model and a smoothing factor of 0.6. The surface expression of the fault is shown in Figure 2.9.**

Figure 2.5 (a-b) shows the modeled displacement fields and the residuals for a distributed slip model with roughness of 4 (smoothing of 0.38), respectively. The residuals are decreased significantly with respect to the uniform-slip model. Figure 2.6 shows (a) the oblique slip, (b) the strike slip and (c) the dip slip on a single fault using the same model. The strike-slip component is much higher than the dip-slip component, where most of the strike-slip motion is located at a shallow depth of 15 km. Moreover, we observe that the two patches representing the dip-slip and strike-slip maxima do not coincide at a single location.

The moment magnitude of this model is  $6.30\text{e}+25$  dyne/cm, 5% higher than the cumulative released moment recorded from the USGS (<http://comcat.cr.usgs.gov/>) and the mean  $\chi^2$  test result is 1.7 (Table 2.2). With this model, we successfully reduce the residuals and retrieve a better solution than a uniform-slip model.

**Table 2.2. Fault slip inversion results for the single fault solution with different smoothing values as Figures 2.5-2.10.**

<b>Smoothing Factor</b>	<b><math>\chi^2</math> test</b>	<b>Moment (Dyne/cm)</b>	<b>Magnitude</b>
0.38	1.7	$6.3\text{e}+25$	6.49
0.1	1.6	$7.7\text{e}+25$	6.56
0.6	1.8	$5.8\text{e}+25$	6.47

In an attempt to separately distinguish the patches on the fault, we run the inversion with one rougher and one smoother model, by assigning smoothing criteria of 0.1 and 0.6, as indicated in Figure 2.4. Figure 2.7 (a) shows the modeled displacement and (b) the

residual displacement on a single fault by using a smoothing factor of 0.1. Figure 2.8 demonstrates (a) the oblique slip, (b) the strike slip and (c) the dip slip on a single fault using the smoothing factor of 0.1. For this model the moment magnitude is  $7.7e+25$  dyne/cm, equivalent to a magnitude 6.56  $M_w$  earthquake (Table 2.2) (~30% higher than the cumulative moment). Figure 2.9 (a) shows the modeled displacement and (b) the residual displacement on a single fault using a smoothing factor of 0.6. Figure 2.10 demonstrates (a) the oblique slip, (b) the strike slip and (c) the dip slip on a single fault using the smoothing factor of 0.6. For this model the moment magnitude is  $5.8e+25$  dyne/cm, equivalent to a magnitude 6.47  $M_w$  earthquake (Table 2.2) (~3% lower than the cumulative moment). For both cases, the same patches reside at the same location. Decreasing the smoothing also does not result in more patches. We conclude that for a single fault, two patches are identified as the most probable sources of failure: one primarily strike-slip and dominating most of the fault length and a second dip-slip patch that only resides on the western half of the fault. We associate each of these patches to each of the Ahar double earthquakes.

In the next step, we explored the possibility that the two earthquakes ruptured two separate fault planes. Inversion for two faults resulted in the convergence to a single fault solution. However, this might be due to the decorrelation of the interferogram in the near field. Consequently, we chose the location and the geometry of the second fault subjectively, based on morphological features, focal mechanism solutions and the associated residuals from the single dislocation modeling. We set the dip angle of the second fault to  $65^\circ$ , as derived from the focal mechanism solutions. The location of the fault is chosen in the region of higher residuals, southwest of the first fault. For the strike angle, we investigated the possibility of two faults: one striking southwest in alignment with the topographic and morphological features (Figure 2.11) and one almost parallel to the first fault according to the focal mechanism solutions (Figure 2.12).

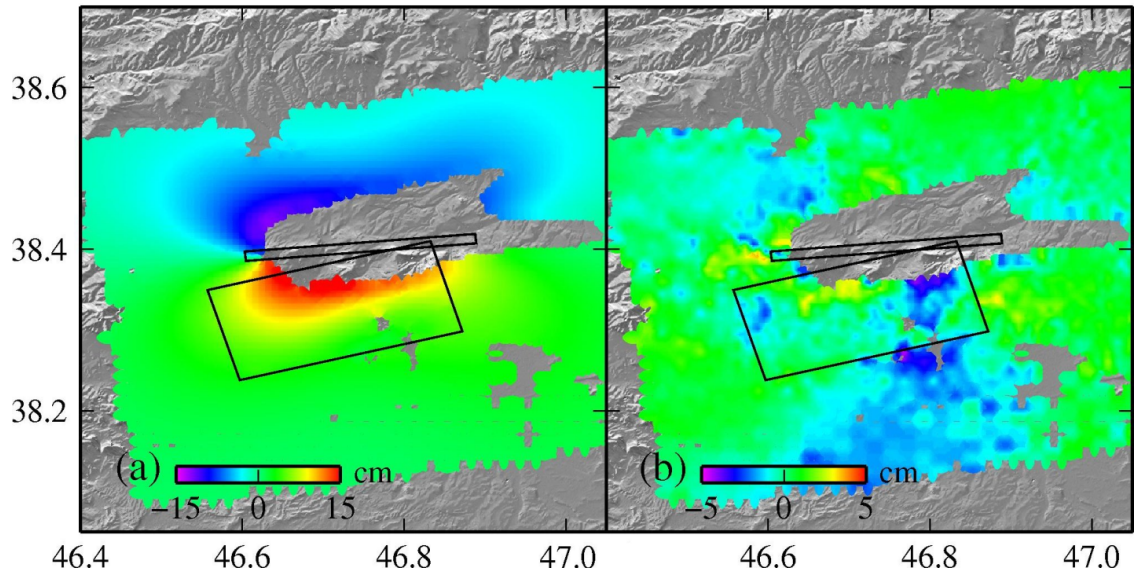


**Figure 2.11. (a) Modeled displacement and (b) residual displacement on two faults and using a distributed-slip model and a smoothing factor of 0.38. The surface expression of the modeled dislocations is shown by a black rectangle. The second fault is striking southwest.**

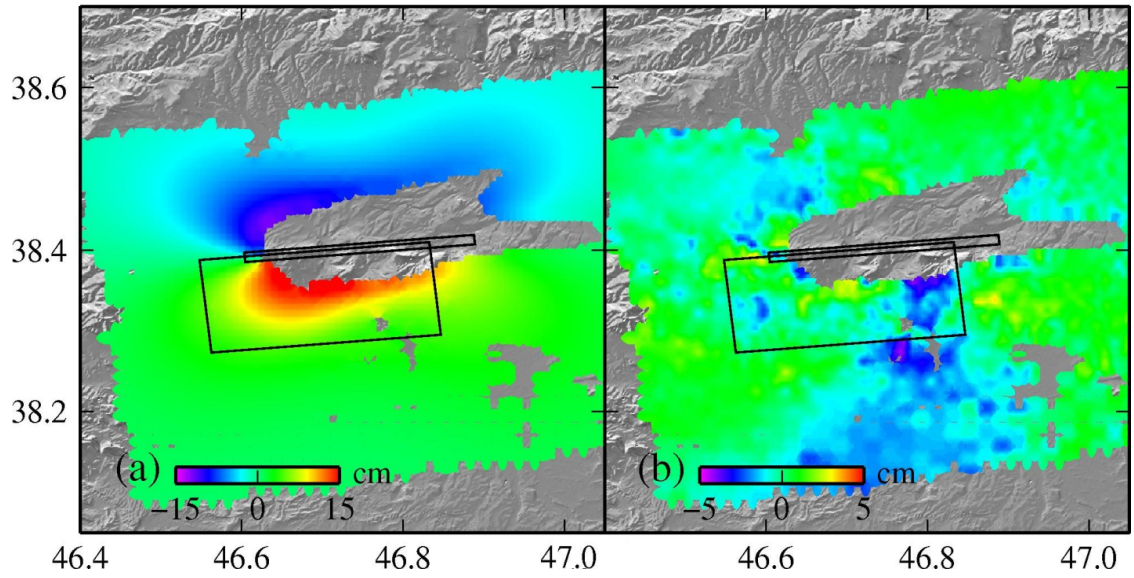


**Figure 2.12. (a) Modeled displacement and the (b) residual displacement on two faults and using a distributed-slip model and a smoothing factor of 0.38. The surface expression of the modeled dislocations is shown by a black rectangle. The second fault is parallel to the first fault.**

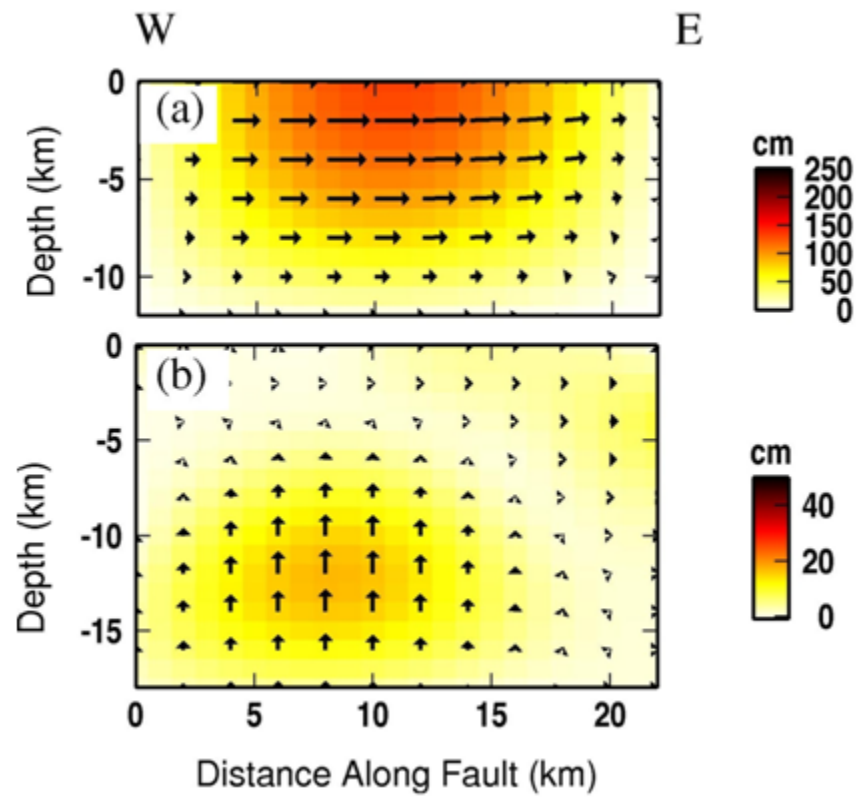


**Figure 2.13.** Slip distribution on two faults using a distributed slip model and a smoothing factor of 0.38, on the (a) primary fault and (b) secondary fault. The surface expression of the fault is shown in Figure 2.11.

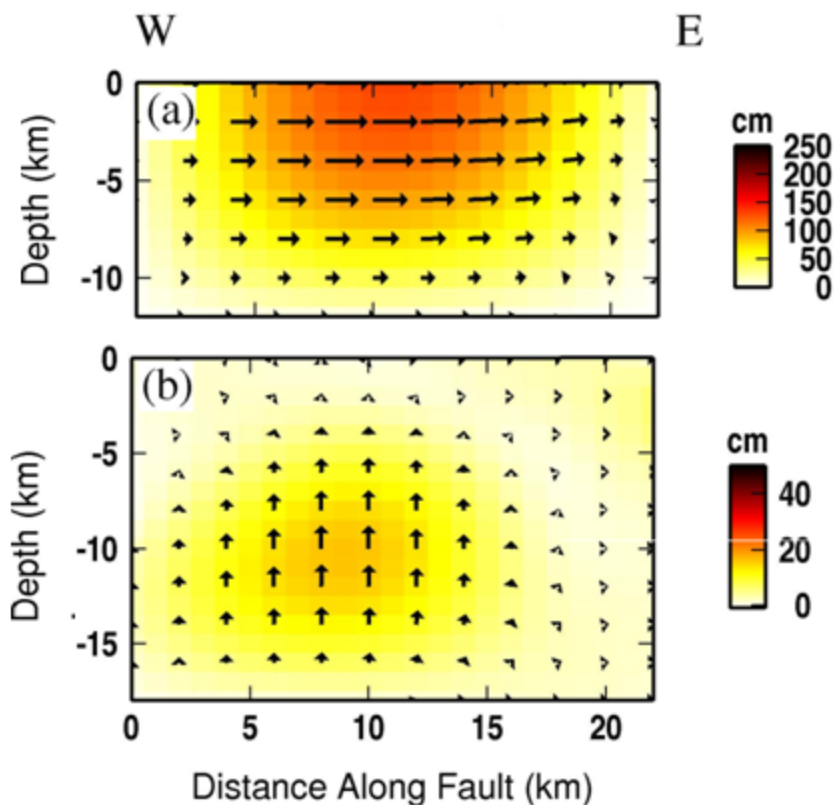


**Figure 2.14.** Slip distribution on two faults using a distributed slip model and a smoothing factor of 0.38, on the (a) primary fault and (b) secondary fault. The surface expression of the fault is shown in Figure 2.12.

**Table 2.3.** Fault slip inversion results for the two fault solution with different geometries as in Figures 2.11-2.14.

	$\chi^2$ test	Moment (Dyne/cm)	Magnitude
1	2	7.9e+25	6.56
2	1.9	7.6e+25	6.55

Figure 2.11 and Figure 2.12 show the models and the residuals for these faults. Figure 2.13 and Figure 2.14 demonstrate the slip on both faults for the geometries presented in Figure 2.11 and Figure 2.12, respectively. In both cases, the slip on the first fault is primarily strike-slip and on the second fault is primarily dip-slip. In either case, the residuals decrease locally but the change is not significant (Table 2.3). The mean residuals for these models are higher than those from a single fault solution (Table 2.2). The cumulative moments in both cases are  $7.9 \times 10^{25}$  dyne/cm and  $7.6 \times 10^{25}$  dyne/cm, 27-32% higher than the cumulative moment from the USGS for the two earthquakes. In addition, the moment release for the second Ahar earthquake is  $1.9 \times 10^{25}$  dyne/cm ( $6.2 M_w$ ), while in the two-fault model, only  $1.0 \times 10^{25}$  dyne/cm of the moment which is 45% lower, is associated with the second fault.

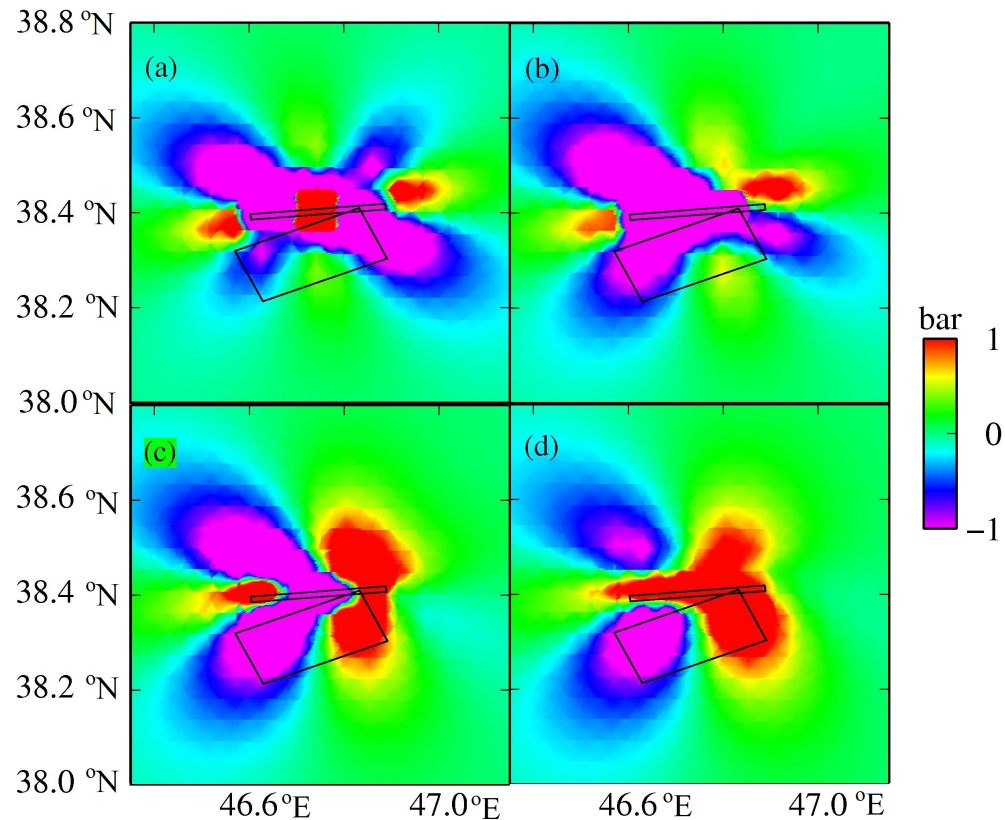


**Figure 2.15. Coulomb stress at (a) zero depth, (b) 5 km depth, (c) 10 km depth and (d) 15 km depth. At the middle of the fault and toward the east there is a decrease in the Coulomb stress.**

#### **2.4. Earthquake Triggering**

We also investigated the possibility that the Ahar earthquakes were two distinct ruptures and that the first triggered the second by analyzing the contribution of the static stress changes from the main fault plane on the surrounding region (Scholz 1990; Stein 1999). Accordingly, we investigate the Coulomb stress change using Coulomb 3.0 (<http://www.coulombstress.org>) (Lin & Stein 2004) in order to better understand the static stress change from the occurrence of the first earthquake. The Coulomb failure

criterion is a measure which explains the induced stresses are encouraging or discouraging for failure on an assumed fault plane (King et al. 1994; Stein 1999). The static stress change is calculated as below,

$$\Delta\sigma_c = \Delta\tau - \mu(\Delta\sigma_n - \Delta p) \quad (2.5)$$

where  $\Delta\tau$  is shear stress changes parallel to the slip direction,  $\Delta\sigma_n$  is normal stress changes,  $\Delta p$  is pore fluid pressure change, and  $\mu$  is the coefficient of friction. A higher pore fluid pressure reduces the normal stress, leading to a higher coulomb stress change.

A simplified form of the above equation is expressed as (King et al. 1994; Reasenber & Simpson 1992).

$$\Delta\sigma_c = \Delta\tau - \mu'\Delta\sigma_n \quad \mu' = \mu(1 - B). \quad (2.6)$$

Here  $B$  is Skempton coefficient and  $\mu'$  is the modified coefficient of friction. The areas of positive Coulomb stress change encouraged failure and areas of negative Coulomb stress change discourage failure on optimally oriented fault planes.

We assumed purely strike-slip motion on the primary fault and investigated the Coulomb failure changes and whether they could trigger a thrust event for the receiver fault geometries demonstrated in Figure 2.11. Figure 2.15 shows the Coulomb stress at (a) zero depth, (b) 5 km depth, (c) 10 km depth and (d) 15 km depth. At shallow depths, the Coulomb stress discourages the occurrence of a thrust event at both the northern or southern portions of the fault. Deeper and towards the east there is an increase in the Coulomb stress. This implies that Coulomb stresses produce an encouraging condition for thrusting at the eastern part of the fault. However, to the west there is no encouraging Coulomb stress change. This again provides support for the rejection of the two-fault scenario, in which each ruptures initiates and propagated along a separate fault plane from the first event.

## 2.5. Discussion

We inverted for the slip distribution of the consecutive Ahar earthquakes of August 11, 2012, 6.4  $M_w$  and 6.2  $M_w$ , using DInSAR data. Our analysis show that although there were two separate events, 11 minutes apart, the two ruptures originated most likely on the same fault plane. Initially, the ruptured plane geometry was constrained by the parameters of the nonlinear inversion for a uniform slip distribution. A more detailed distributed slip inversion was performed and the resulting model has two asperities. One patch dominates the fault plane at shallow depth, propagating to the surface, and a second is located slightly deeper at the eastern half of the fault (Figure 2.6(b-c)). The shallower asperity is mainly strike-slip, with a minor dip-slip component. The deeper asperity is primarily thrust in nature. Applying different smoothing criteria to the resolved model shows that these two asperities are stable and consistent and each corresponds to one of the two distinct Ahar earthquakes.

The cumulative seismic moment for both events is equivalent to  $6.3e+25$  dyne/cm. This is slightly larger than the estimated seismic moment, but this is not unexpected. Geodetic moment is generally higher than seismic moment because some part of the released moment occurs aseismically (Calais et al. 2008). Geodetic measurements from DInSAR also could capture some part of the post-seismic deformation due to the relaxation of the lower crust or afterslip, in addition to the occurrence of aftershock sequences. The moment release from the single dip-slip event at depth is equivalent to an earthquake of magnitude of 6.2  $M_w$ , which agrees well with the USGS solutions. Moreover, as reported by USGS, the depth of the magnitude 6.4  $M_w$  event is shallower than the magnitude 6.2  $M_w$  event. The moment release from the first event is equivalent to an earthquake of magnitude of 6.38  $M_w$ .

We did explore the possibility that the two earthquakes rupture two separate fault planes. This hypothesis prompted us to test various geometries. However, we were not able to find a specific geometry which also agrees with the seismic information and produces smaller residuals. Moreover, the seismic moment released by the second fault for the two fault solution is very small (a difference of almost  $1+25$  dyne/cm), which

corresponds to an event of magnitude 5.9  $M_w$ , not 6.2  $M_w$ . Additionally, Coulomb failure analysis demonstrates that the first event did not encourage rupture initiation at the most likely locations for the second event.

Modeling of the Ahar earthquake is important for the estimation of local and regional seismic hazard. Locating the active faults which are accumulating interseismic stress is a key factor in the earthquake studies. To do so, it is necessary to accurately map those geological structures that are more favorable for rupture under the current stress field in NW Iran. Moreover, the partial stress released by earthquakes such as the Ahar event can affect the magnitude and rupture extent of the next large earthquake in NW Iran. Figure 2.1 shows the interseismic velocity vectors from GPS measurements for the 2002-2004 time periods with respect to the Central Iran block (Masson et al. 2007). We observe that north of NTF and close to Ahar, most of these stations have an E-W velocity component. This is in agreement with the geometry of the ruptured fault from our solution and its right-lateral coseismic slip.

Previous studies (Masson et al. 2007) suggest that almost all of the shear stress is relieved by the NTF in NW Iran. Our results indicate that there are secondary strike-slip faults other than the NTF and that they account for a significant portion of the remnant tectonic stress. We infer that structures such as the one ruptured by the Ahar earthquakes are playing a role in the interseismic stress accumulation in NW Iran. Studies by (Moradi et al. 2011) show that north of the NTF, the clusters of seismicity are more distributed further from the NTF. Scattered seismicity is related to the presence of small fault structures, which diffuse the concentration of seismic energy away from the NTF fault. Fault block models derived from GPS measurements (Djamour et al. 2011) in which contributions from secondary faults are assumed to be minimal and most of the strike-slip is attributed to the NTF result in residuals at the Ahar GPS station on the order of 3-4 mm. Our results suggest that in order to reduce the residual, other faulting mechanisms should be added in this region and that detailed models should take into account independent slip on minor faults in NW Iran.

## 2.6. Conclusion

We have investigated the source models of the double Ahar earthquakes (6.4  $M_w$  and 6.2  $M_w$ ), Iran, which occurred on August 11, 2012. First, we used a nonlinear GA inversion technique to derive the geometry of a single uniform slip model corresponding to these earthquakes. Furthermore, we used this geometry and inverted for the distributed slip model to resolve a detailed slip pattern which accounts for both earthquakes. In addition, we investigated the possibility of the second Ahar earthquake occurring on a separate fault plane. The results of our analysis show that there was only one ruptured fault plane for both ruptures. This single fault plane is an E-W oriented structure with one major strike-slip component dominating the fault and a second, minor dip-slip component localized at its western portion. Moreover, the Coulomb stress analyses do not show any encouraging stress change to support rupture on a secondary fault, as described by the focal mechanism solutions.

Identification of this an E-W trending fault structure shows that tectonic stresses do not accumulate only along the NW-SE trending NTF, demonstrating that there are secondary structures that should be taken into consideration to assess the seismic hazard in this region.

## 2.7. Acknowledgements

We acknowledge the contribution of the Canadian Space Agency that provided the RADARSAT-2 data. The work of S. Alipour and P. J. González was supported by an Ontario Early Researcher Award and the NSERC and Aon Benfield/ICLR Industrial Research Chair in Earthquake Hazard Assessment. The work of K. F. Tiampo was supported by the NSERC and Aon Benfield/ICLR Industrial Research Chair in Earthquake Hazard Assessment. GMT software (Wessel & Smith 1998) was used to create the figures. We are thankful to the USGS for use of the Coulomb 3 software.

## 2.8. References

- Amelung, F., Galloway, D. L., Bell, J.W., Zebker, H. A. & Lacznik, R. J., 1999. Sensing the ups and downs of Las Vegas: InSAR reveals structural control of land subsidence and aquifer-system deformation. *Geology*, **27**, 483-486
- Bamler, R. & Hartl, P., 1998. Synthetic aperture radar interferometry. *Inverse Probl.* **14**, 1- 54
- Beavan, J., Fielding, E., Motagh, M., Samsonov, S. & Donnelly, N. 2011. Fault location and slip distribution of the 22 February 2011 Mw 6.2 Christchurch, New Zealand, earthquake from geodetic data. *Seis. Res. Letts.*, **82**, 789-799, doi:10.1785/gssrl.82.6.789
- Berardino, P., Lanari, R. & Sansosti, E., 2002. A New algorithm for surface deformation monitoring based on small baseline differential SAR interferograms. *IEEE Trans. Geosci. Remote Sens.*, **40**, 2375-2383
- Bürgmann, R. *et al.*, 2002. Deformation during the 12 November 1999 Düzce, Turkey, earthquake from GPS and InSAR data. *Bull. Seismol. Soc. Am.*, **92**, 161-171
- Calais, E. *et al.*, 2008. Strain accommodation by slow slip and dyking in a youthful continental rift, East Africa. *Nature*, **456**, 783-787
- Carnec, C. & Delacourt, C., 2000. Three years of mining subsidence monitored by SAR interferometry, Gardanne, France. *App. Geophys.*, **43**, 43-54
- Costantini, M. & Rosen, P. A., 1999. A Generalized Phase Unwrapping Approach for Sparse Data. *IEEE Geosci. Remote Sens. Sym.* Hamburg, Germany, 267-269
- Djamour, Y., Vernant, P., Nankali, H. R. & Tavakoli, F., 2011. NW Iran-eastern Turkey present-day kinematics: Results from the Iranian permanent GPS network. *Earth planet. Sci. Lett.* **307**, 27-34, doi:10.1016/j.epsl.2011.04.029

Farr, T. G. *et al.*, 2007. The Shuttle Radar Topography Mission, *Rev. Geophys.*, **45**, 2, doi:10.1029/2005RG000183

Ferretti, A. *et al.*, 2001. Permanent Scatters in SAR Interferometry. *IEEE Trans. Geosci. Remote Sens.*, **39**, 1

Funning, G. J., Parsons, B., Wright, T. J., Jackson, J. A. & Fielding, J. A., 2005. Surface displacements and source parameters of the 2003 Bam (Iran) earthquake from Envisat advanced synthetic aperture radar imagery. *J. Geophys. Res.*, **110**, B09406, doi:10.1029/2004JB003338

González, P.J., Camacho, A.G. & Fernández J. 2009. Co-seismic three dimensional displacements determined using SAR data: theory and an application test. *Pure and Applied Geophysics*, **166**, doi:10.1007/s00024-009-0500-7

Holland, J. H., 1975. *Adaptation in natural and artificial systems*. Univ. Michigan Press, Michigan

Holland, J. H., 1992. *Adaptation in natural and artificial systems: An Introductory Analysis with Applications to Biology, Control, and Artificial Intelligence*, M.I.T. Press Cambridge, Massachusetts

Hooper, A., Segall, P. & Zebker, H., 2007. Persistent Scatterer InSAR for Crustal Deformation Analysis, with Application to Volcán Alcedo, Galápagos. *J. Geophys. Res.*, **112**, B07407, doi:10.1029/2006JB004763

Goldstein, R. M. & Werner, C. L., 1998. Radar interferogram filtering for geophysical applications. *Geophys. Res. Lett.*, **25**, 4035-4038, doi:10.1029/1998GL900033

González, P. J., Tiampo, K. F., Palano, M., Cannavó, F. & Fernández, F. 2012. The 2011 Lorca earthquake slip distribution controlled by groundwater crustal unloading, *Nature Geoscience*, **5**, 821-825, doi:10.1038/ngeo1610

Jackson, J. & McKenzie, D., 1984. Active tectonics of the Alpine-Himalayan belt between western Turkey and Pakistan. *Geophys. J. Roy. Astron. Soc.*, **77**, 185-264

Jackson, J. A., Priestley, K., Allen, M. & Berberian, M., 2002. Active tectonics of the South Caspian Basin. *Geophys. J. Int.* **148**, 214-245

Jónsson, S., Zebker, H., Segall, P. & Amelung, F., 2002. Fault Slip Distribution of the 1999 Mw7.1 Hector Mine Earthquake, California, estimated from Satellite Radar and GPS Measurements, *Bull. Seismol. Soc. Am.*, **92**, 1377-1389

King, G. C. P., Stein, R. S. & Lin, J., 1994. Static stress changes and the triggering of earthquakes. *Bull. Seismol. Soc. Am.* **84**, 935-93

Lin, J. & R. S. Stein, 2004. Stress triggering in thrust and subduction earthquakes and stress interaction between the southern San Andreas and nearby thrust and strike-slip faults. *J. Geophys. Res.*, **109**, B02303, doi:10.1029/2003JB002607

Manconi, A., Walter, T. R., Manzo, M., Zeni, G., Tizzani, P., Sansosti, E. & Lanari, R., 2010. On the effects of 3-D mechanical heterogeneities at Campi Flegrei caldera, southern Italy. *J. Geophys. Res.*, **115**, B08405, doi:10.1029/2009JB007099

Masson, F., Anvari, M., Djamour, Y., Walpersdorf, A., Tavakoli, F., Daignières, M., Nankali, H. & Gorp, S. V., 2007. Large-scale velocity field and strain tensor in Iran inferred from GPS measurements: new insight for the present-day deformation pattern within NE Iran, *Geophys. J. Int.* **170**, 436–440

Massonnet, D., Briole, P. & Arnaud, A., 1995. Deflation of Mount Etna monitored by spaceborne radar Interferometry, *Nature*, **375**, 567-570

Massonnet, D. & Feigl, K. L., 1998. Radar interferometry and its application to changes in the earth's surface. *Rev. Geophys.* **36**, 441-500

Massonnet, D. & Rabaute, T., 1993. Radar interferometry: limits and potential, *IEEE Trans. Geosci. Remote Sen.*, **31**, 455-464

Moradi, A. S., Hatzfeld, D. & Tatar, M., 2011. Microseismicity and seismotectonics of the North Tabriz fault (Iran), *Tectonophysics*, **506**, 22-30, doi:10.1016/j.tecto.2011.04.00

- Okada, Y., 1985. Surface deformation due to shear and tensile faults in a half-space. *Bull. Seism. Soc. Am.*, **75**, 1435-1154
- Okada, Y., 1992. Internal deformation due to shear and tensile faults in a half-space. *Bull. Seism. Soc. Am.*, **82**, 1018-1040
- Reasenber, P. A. & Simpson, R.W., 1992. Response of regional seismicity to the static stress change produced by the Loma Prieta earthquake. *Science*. **255**, 1687-1690
- Reilinger, R., McClusky, S., Vernant, P., Lawrence, S. & Ergintav, S., 2006. GPS constraints on continental deformation in the Africa-Arabia-Eurasia continental collision zone and implications for the dynamics of plate interactions. *J. Geophys. Res.* **111**, doi:10.1029/2005JB004051
- Sandwell, D. T. & Price, E. J., 1998. Phase gradient approach to stacking interferograms. *J. Geophys. Res.-Solid Earth*, **103**, 30183-302
- Scholz, C.H., 1990. *The Mechanics of Earthquakes and Faulting*. Cambridge Univ. Press, New York
- Sen, M.K. & Stoffa, P.L. 1992. Rapid sampling of model space using genetic algorithms: examples from seismic waveform inversion. *Geophys. J. Int.* **108**, 281-292
- Short, N., Brisco, B. & Murnaghan, K., 2012. Monitoring permafrost environments with InSAR and polarimetry, case studies from Canada. *IEEE Geosci. Remote Sens. Sym.* 4034-4037, doi:10.1109/IGARSS.2012.6350524
- Stein, R. S., 1999. The role of stress transfer in earthquake occurrence. *Nature*, **402**, 605-609
- Strozzi, T., Luckman, A., Murray, T., Wegmuller, U. & Werner, C., 2002. Glacier motion estimation using SAR offset-tracking procedures. *IEEE Trans. Geosc. Remote Sens.*, **40**

Tiampo, K. F., Rundle, J. B., Fernandez, J. & Langbein, J. O. 2000. Spherical and ellipsoidal volcanic sources at Long Valley caldera, California, using a genetic algorithm inversion technique, *Journal of Volcanology and Geothermal Research*, **102**, 3, 189-206

Tikhonov, A.N. & Arsenin, V.Y., 1977. *Solution of Ill-posed Problems*. Winston & Sons Washington

Vasco, D. W., Ferretti, A. & Novali, F., 2008. Reservoir monitoring and characterization using satellite geodetic data: Interferometric synthetic aperture radar observations from the Krechba field, Algeri. *Geophys.*, **73**, doi:10.1190/1.2981184

Vernant, P. & Chery, J., 2006. Low fault friction in Iran implies localized deformation for the Arabia Eurasia collision zone, *Earth planet. Sci Lett.*, **246**, 197-206

Wegmuller, U. & Werner, C. 1997. Gamma SAR processor and interferometry software. *3<sup>rd</sup> ERS symposium on space at the service of our environment*, Florence, Italy

Wells, D. L. & Coppersmith, K. J., 1994. New empirical relationships among magnitude, rupture length, rupture width, rupture area, and surface displacement, *Bull. Seism. Soc. Am.*, **84**, 974-1002

Wessel, P. & Smith, W. H. F. 1998. New, improved version of Generic Mapping Tools released. *EOS Trans. Am. Geophys. Union*, **79**, 579

Winchester, J.P., Creager, K.C. & McSweeney, T.J. 1993. Better alignment through better breeding: Phase alignment using genetic algorithms and cross-correlation techniques. *EOS Trans. AGU*, **74**, 394

## Chapter 3

### 3 Multibaseline PolInSAR using RADARSAT-2 Quad-pol data: improvements in interferometric phase analysis<sup>2</sup>

*In this chapter, a method of multibaseline coherence optimization is applied for the first time to quad-pol RADARSAT-2 data. The three channels of SAR images, HH, VV and VH, were integrated to select the optimized scattering mechanism and convert the SAR images from a linear polarimetric basis to the optimized basis. In order to analyze our results, we first generated interferograms for both HH and for the optimized channels. Moreover, we assessed the performance of PolInSAR both in terms of the number of coherent pixels and phase quality. The RADARSAT-2 images were contaminated by residual orbital errors. As a result, the orbital ramp was used to visually assess the quality of interferometric and the performance of coherence optimization technique. The result of this study showed that not only the number of coherent pixels increases significantly by using quad-pol optimization but that the quality of the interferometric phase improves considerably as well.*

---

<sup>2</sup> © [2013], IEEE. Reprinted, from Geosciences and Remote Sensing Letters

### 3.1.Introduction

Differential Interferometric Synthetic Aperture Radar (DInSAR) is a technique for measuring ground surface deformation. However, standard DInSAR is subject to decorrelation effects. Decorrelation of the signal can obscure the deformation phase and degrade the precision of DInSAR results. In recent years, the acquisition of large quantities of SAR data has led to the development of multibaseline DInSAR techniques (Berardino et al. 2002; Hooper et al. 2007; Ferretti et al. 2001). These methods perform DInSAR analysis on a subset of pixels, as in the case of the Persistent Scatterers (PS) technique (Hooper et al. 2007). Ideally, the PS pixels return a stable backscatter signal through time. As a result, the phase signature of PS pixels is less affected by spatial and temporal decorrelation, resulting in a more reliable estimate of ground deformation. However, in order to identify PS pixels, a group of Pixel Candidates (PCs) with a higher S/N ratio must be selected, normally based on an amplitude dispersion index (Ferretti et al. 2001) or coherence criterion (Adam et al. 2005). Accordingly, PS pixels are the PCs for which the phase stability criterion holds e.g. with respect to nearby candidates (Hooper et al. 2007). This higher density of PCs and associated PS pixels provides a better estimate of the deformation over the relevant time periods.

Full polarimetric SAR data provides additional information that can be used to increase the number of reliable points in an interferogram (Navarro-Sanchez et al. 2010). The choice of the best polarimetric channel reduces decorrelation noise and increases the number of pixels with increased coherence, one potential measure of the phase noise of an interferogram. Coherence optimization of polarimetric SAR data is a technique which can be used to resolve dominant scatterers in a vertically structured media (Papathanassiou & Cloude 2001). The first coherence optimization technique was presented by Cloude and Papathanassiou (1998) and later expanded by others (Colin et al. 2006; Qong et al. 2005). Subsequently this technique was extended to optimize the coherence of multibaseline interferograms simultaneously (Neumann et al. 2008).

In this paper, for the first time, a multibaseline coherence optimization approach proposed by (Neumann et al. 2008) is applied to fully polarimetric space-borne satellite

data. Here we use fifteen images of RADARSAT-2 satellite. These images which are acquired in quad-pol mode are used to investigate the performance of multibaseline Polarimetric SAR Interferometry (PolInSAR) coherence optimization. The study region is San Francisco Bay area, adjacent to both the San Andreas and the Hayward faults, the region with the highest seismic hazard in northern California. Previous studies employed DInSAR and advanced DInSAR techniques on single channel data in order to study deformation along this fault (Bürgmann et al. 1998; Lanari et al. 2007). However, our objective is to use fully polarimetric data and integrate polarimetric and interferometric techniques in order to improve the quality of the resulting interferograms. In addition, we will investigate how the application of this technique enhances the number of PCs for multibaseline InSAR processing. The effects of variations in the spatial and temporal baselines interferograms also will be investigated.

### 3.2. Polarimetric SAR Interferometry (PolInSAR)

Fully polarimetric SAR (Pol-SAR) sensors measure the  $2 \times 2$  scattering matrix,  $S$ , corresponding to each pixel. Under the reciprocity theorem, the off-diagonal elements are equal and  $S_{HV} = S_{VH}$ . The scattering matrix is expressed as a vector using the Pauli basis as (Cloude & Papathanassiou 1998)

$$k_i = \frac{1}{\sqrt{2}} [S_i^{HH} + S_i^{VV}, S_i^{HH} - S_i^{VV}, 2S_i^{HV}]^T \quad (3.1)$$

where the  $S_i^{HH}$  and  $S_i^{VV}$  are co-polar terms and  $S_i^{HV}$  is the cross-polar term.  $i$  is the number of each set of quad-pol images and  $T$  is the transpose operator.

PolInSAR forms an interferogram by projecting each SAR image pixel,  $k$ , on a corresponding scattering mechanism,  $\omega$ , resulting in a new pixel value,  $\lambda$ . Performing this operation on a pixel by pixel basis will result in a new SAR image. By changing the polarization basis for both SAR images following (3.2), the corresponding interferogram is given by (3.3)

$$\lambda_i = \omega_i^{*T} k_i \quad (3.2)$$

$$\varphi_{ij(\omega_i, \omega_j)} = \arg(\lambda_i \lambda_j^{*T}) = \arg(\omega_i^{*T} \Omega_{ij} \omega_j), \quad (3.3)$$

$$\Omega_{ij} = \langle k_i k_j^{*T} \rangle, \quad T_{ii} = \langle k_i k_i^{*T} \rangle$$

where \* represents conjugate operator and  $\langle \rangle$  is the multilooking factor.  $T_{ii}$  is the coherency matrix for SAR image  $i$  and  $\Omega_{ij}$  is the coherency matrix between two images  $i$  and  $j$ . Accordingly  $\varphi_{ij(\omega_i, \omega_j)}$  is the interferometric phase in the new polarimetric basis. Interferometric coherence,  $\gamma_{ij(\omega_i, \omega_j)}$ , is calculated for two sets of SAR images in any arbitrary polarimetric basis defined by  $\omega_i$  and  $\omega_j$  as (3.4)

$$\gamma_{ij(\omega_i, \omega_j)} = \frac{\omega_i^{*T} \Omega_{ij} \omega_j}{\sqrt{\omega_i^{*T} T_{ii} \omega_i \omega_j^{*T} T_{jj} \omega_j}} \quad (3.4)$$

Coherence optimization consists of selecting those scattering mechanisms which provide the maximum coherence value. In the case of Equal Scattering Mechanism Multibaseline (ESM-MB) as proposed by (Neumann et al. 2008), the scattering mechanisms of the images remain the same among all the baselines ( $\omega_i = \omega_j$ ). However, this condition is not met using a Multiple Scattering Mechanism Multibaseline technique (MSM-MB), ( $\omega_i \neq \omega_j$ ) and for every acquisition an individual optimal polarization is found which correlates best to all others.

In previous research on DInSAR applications, the ESM has been applied in lieu of the MSM technique (Navarro-Sanchez et al. 2010), for the primary reason that the MSM technique chooses various scattering mechanism for each SAR acquisition. This can introduce an additional interferometric phase of the DInSAR method. While in reality some physical effects (e.g. change in soil moisture content, incident angle and atmospheric conditions) will modify the scattering mechanisms between acquisitions, leading to temporal decorrelation, the change of scattering mechanism between acquisitions might compensate for the temporal decorrelation in areas of less noise. Therefore, in some cases, the choice of MSM may provide better resolution of the interferometric phase. However, this is not guaranteed and the choice of MSM can lead to amplification of interferometric phase noise. As a result, for this study, ESM-MB was

applied in order to provide a better understanding of the role of decorrelation in space and time.

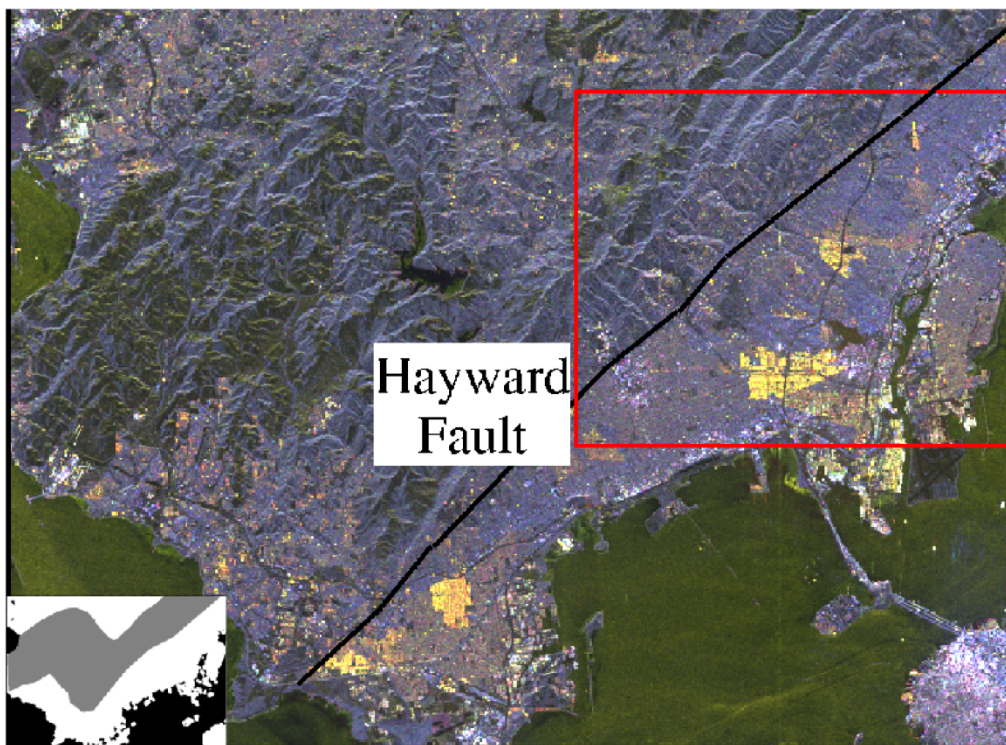


**Figure 3.1. RGB amplitude image of San Francisco city acquired from RADARSAT-2 satellite (R: HH channel, G: VV channel, B: VH channel). The black line delineates the approximate trace of the Hayward fault. The red square shows the close up region used for interferometric analysis. The black and white figure shows the two subregions used for further analysis in Figures 3.3-3.4. White and gray colors represents urban the rural areas, respectively.**

### **3.3. Application of Coherence Optimization Technique**

We applied the ESM-MB coherence optimization algorithm proposed by (Neumann et al. 2008) for the first time to space-borne SAR images acquired by the RADARSAT-2 satellite. The nominal height of the satellite is 798 km with swath width of approximately 25 km. Polarimetric acquisition halves the swath width of the imaging SAR. The region

is imaged from incident angle of 28 degrees with spatial resolution of ~5 meters. The performance of coherence optimization greatly depends on the configuration of acquisition system, e.g. baseline lengths, acquisition times and frequency (Neumann et al. 2008). Here, quad-pol optimization will be assessed on C-band imagery with a large number of baselines and wider range of spatial and temporal separations. The study area is shown in Figure 3.1. The black line approximately delineates the trace of the Hayward fault. The RGB image in this figure is representative of the amplitude images from three polarimetric channels (HH, VV and VH), respectively. This area is covered by dense vegetation and rough topography in the middle of the image. The lower parts of this image are mainly composed of man-made structures.

As a proof of the concept, we chose fifteen images, a subset of which was employed previously in a Polarization Phase Difference analysis (Samsonov & Tiampo 2011). The SAR images were acquired at the following dates: 2008/04/26, 2008/06/13, 2008/07/07, 2008/07/31, 2008/12/22, 2009/01/15, 2010/09/07, 2010/10/01, 2010/10/25, 2010/11/18, 2010/12/12, 2011/01/05, 2011/01/29, 2011/02/22, and 2011/03/18. First, the polarimetric SAR images were co-registered to sub-pixel accuracy. Later, all possible SAR pairs for interferogram formation were selected corresponding to three polarimetric channels (HH, VV, and VH). The number of possible interferograms corresponding to each polarimetric channel is 105 (see Table S1, Supplemental Material). The spatial perpendicular baselines vary between 1 and 384 meters, while the temporal baselines vary from 24 days to 3 years. Interferograms are formed with a multilooking factor of five in range and ten in azimuth ( $5 \times 10$ ), resulting in final ground resolution of  $24 \times 47$  meters. Coherences are calculated by using a correlation window of  $5 \times 10$  pixels.

Multibaseline coherence optimization was applied to the polarimetric SAR images. The code is written in C++ language using the Lapack library<sup>3</sup> for efficient complex matrix operations. First, optimum scattering mechanisms ( $\omega$ ) were estimated, and then applied using (3.2) to transform the pixels from linear to the optimized polarimetric basis.

---

<sup>3</sup> <http://www.netlib.org/lapack/>

Once this processing step was complete, the optimized SAR images were used to produce the coherences and interferograms between the same pairs, as detailed above for SAR images in (H,V) polarization basis, using (3.3) and (3.4). Then, the estimated optimized interferograms and coherences were compared with interferograms produced from single polarimetric channels.

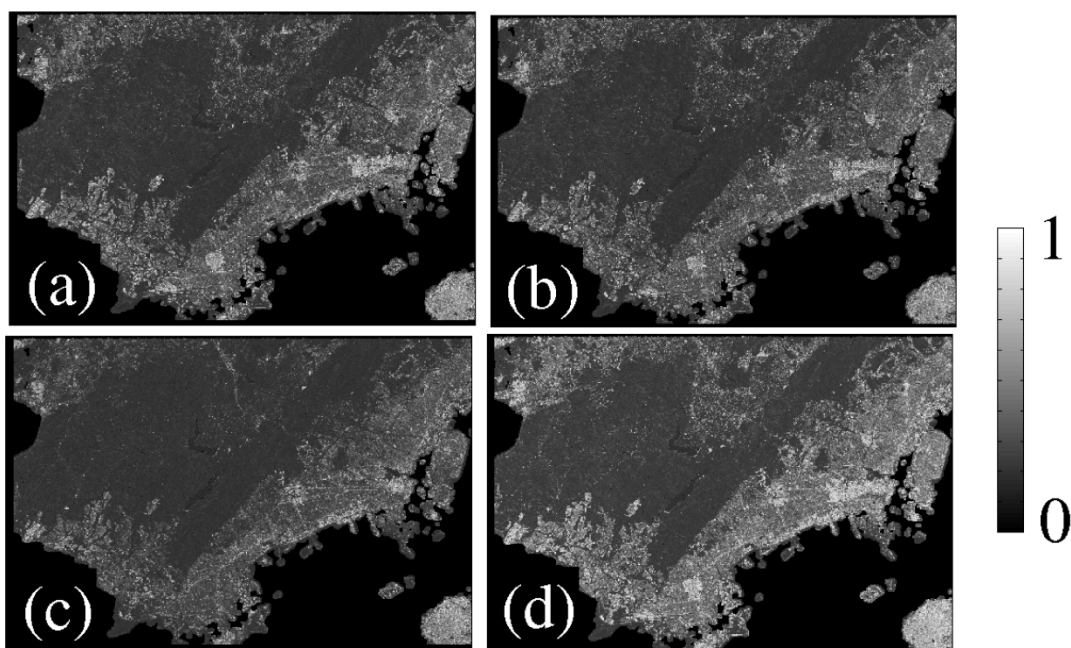


**Figure 3.2. Mean coherence maps, (a) HH, (b) VV, (c) VH and (d) optimized images. Improvement of PolInSAR coherence (d) is clearly demonstrated with respect to single-pol channels (a-c).**

### 3.4. Performance of the Coherence Optimization Algorithm

Figure 3.2 (a-d) displays the mean coherence images retrieved from interferometric stack of HH, VV, VH and the optimized channel, respectively. Visual inspection of these figures confirms that coherence is enhanced significantly with respect to the single polarization estimates.

We divided the images in two subregions; rural and urban, identified in Figure 3.1 by white and gray colors, respectively. Figure 3.3 (a-c) compares the mean coherences of the optimized and the HH channel associated with the entire image and the rural and urban subregions. Note that in Figure 3.3, the histogram of the urban region after optimization changes significantly, with most of the pixels tending to form a second peak at a much higher coherence than their initial HH coherences. This is the result of the abundance of man-made structures. The scarcity of these features for rural regions results in a modest coherence increment (Figure 3.3 (b)).

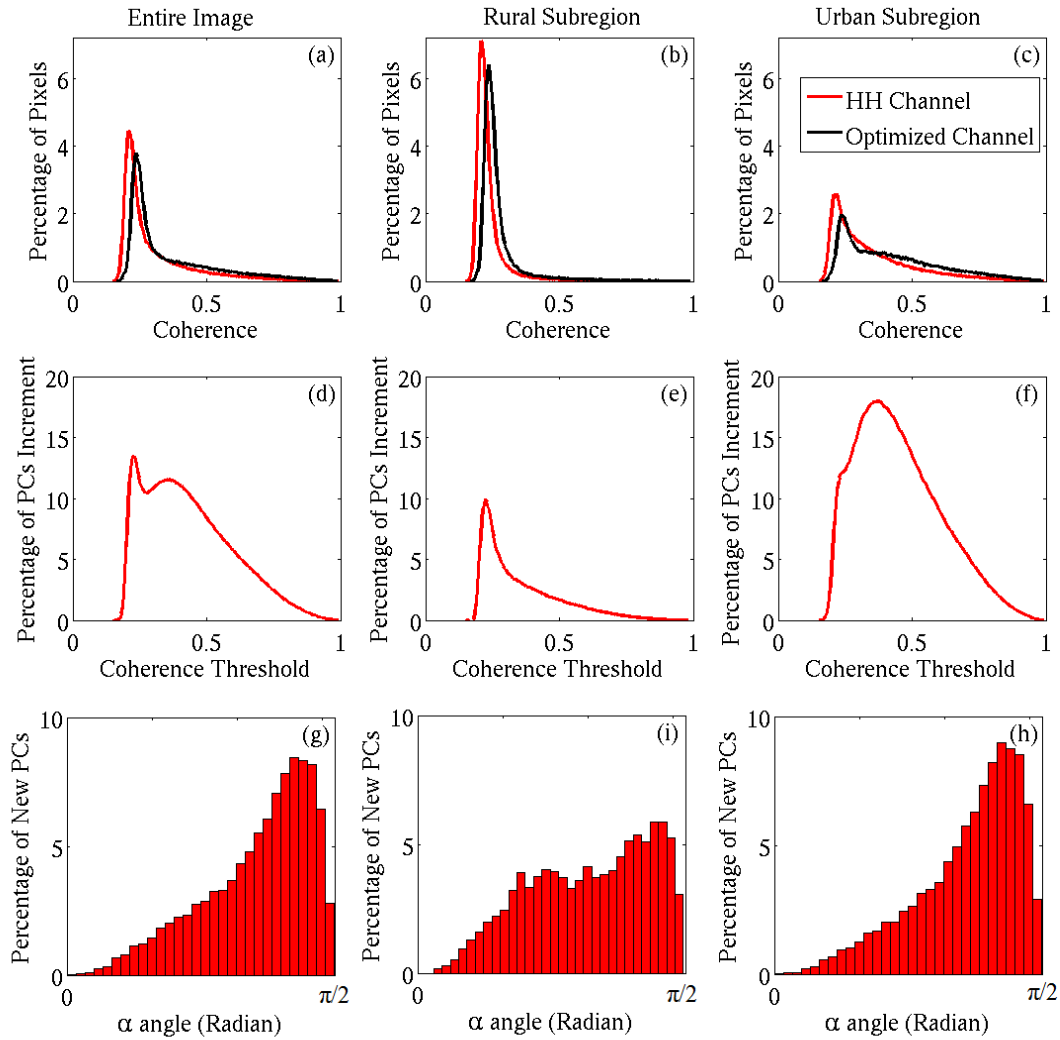
Figure 3.3 (d-f) investigates the coherence improvement in terms of the number of PCs. The quality criterion used here for selection of PCs is the mean coherence value computed over the interferometric stack. Here, the horizontal axis represents the coherence threshold and the vertical axis represents the increment from HH to the optimized channel in the percentage of PCs with respect to the total number of pixels in the entire image. Again, the percentage increase in PCs is calculated with respect to the entire image pixels, not with respect to those identified by the HH channel. For the urban area, the maximum increment in the percentage of PCs is ~18%. For the rural area with higher topography and increased volume scattering from vegetation, the maximum increase in PCs reaches 10%. Note that many of these PCs are not detected in any single polarimetric channel, including HH, VV or VH; e.g. by using a coherence threshold of 0.3 for the entire image, this percentage increase is 7%. If we make the same comparison between the optimized channel with the average of three single polarimetric channels (HH, VH, VV), we get 10% increase in the number of newly selected PCs by applying the optimization procedure.

Figure 3.3 (g-i) displays the histogram of  $\alpha$  angle for the newly detected PCs in the optimized compared to the HH channel, using a coherence threshold of 0.3. The  $\alpha$  angle represents types of the optimum scattering mechanisms derived from parameterization of the optimized scattering vectors (Cloude & Pottier 1997). According to (3.5), the scattering vector is described by scattering mechanism ( $\alpha$ ), orientation angle ( $\beta$ ),  $\varepsilon'$  and  $\mu'$  as target phase angles. Here, we specifically consider the  $\alpha$  which ranges between [0

90] degrees. Roughly speaking,  $\alpha$  angles close to 0, 45 and 90 degrees correspond to surface scattering, volume scattering and double bounce scattering, respectively.

$$\omega = [\cos \alpha, \sin \alpha \cos \beta e^{i\varepsilon'}, \sin \alpha \sin \beta e^{i\mu'}] \quad (3.5)$$

The results are shown for (g) the entire image pixels, (h) rural and (i) the urban subregions. Analysis of the results shows that histograms are mostly skewed toward higher  $\alpha$  angles, representing pixels of double or even bounce scattering mechanisms. These scattering types are present in both the rural and urban subregions as e.g. man-made structures. Moreover, the histogram of rural subregion owns a secondary peak at lower  $\alpha$  angles. This corresponds to scattering mechanisms from e.g. rough surfaces where the optimization could differentiate some pixels as possible PC targets.



**Figure 3.3 (a-c) Histograms of the mean coherences for the HH and the optimized polarimetric channels associated with (a) the entire image, (b) rural and (c) urban subregions. (d-f) PCs increment after application of PolInSAR for an arbitrary coherence threshold. Here, the horizontal axis represents the coherence threshold and the vertical axis is the increase in the number of PCs from HH channel to the optimized channel, associated with (d) the entire image, (e) the rural subregion and (f) the urban subregion. Note that the percentage is with respect to the entire image pixels. (g-i) histogram of  $\alpha$  angle for the newly selected PCs in the optimized compared to HH channel (with coherence threshold of 0.3) for the (g) entire image pixels, (h) rural and (i) urban subregions, respectively.**

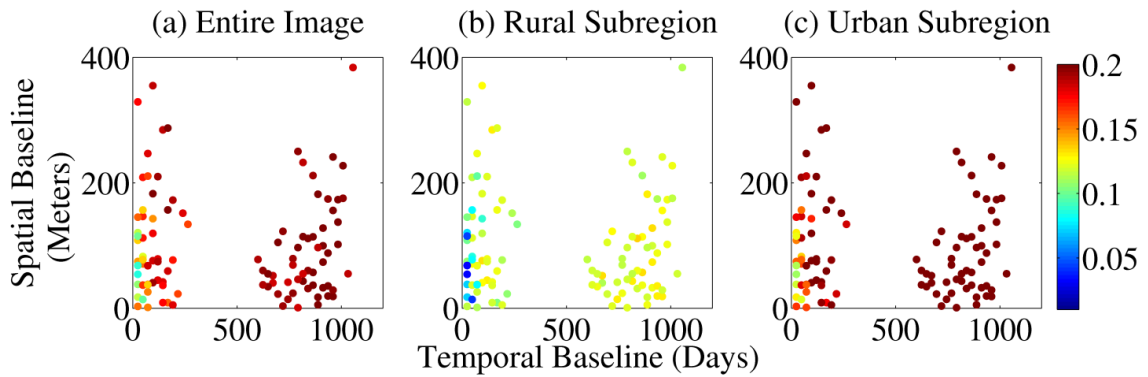


**Figure 3.4 (a-c) Relative mean coherence improvement (with respect to initial HH coherence) for individual interferograms of different spatial and temporal baseline, for (a) the entire image, (b) rural subregion and (c) urban subregion.**

Figure 3.4 shows the relationship between relative coherence increment with respect to HH channel for each individual spatial and temporal baseline corresponding to (a) entire image, (b) rural subregion, and (c) urban subregion. In these figures, there is clear relationship with the temporal and spatial separation of interferograms. Generally, for a very short temporal and spatial baseline interferograms, we observe a smaller coherence increment. That the relative coherence improvement is stronger over larger baselines is related to lower initial coherence level.

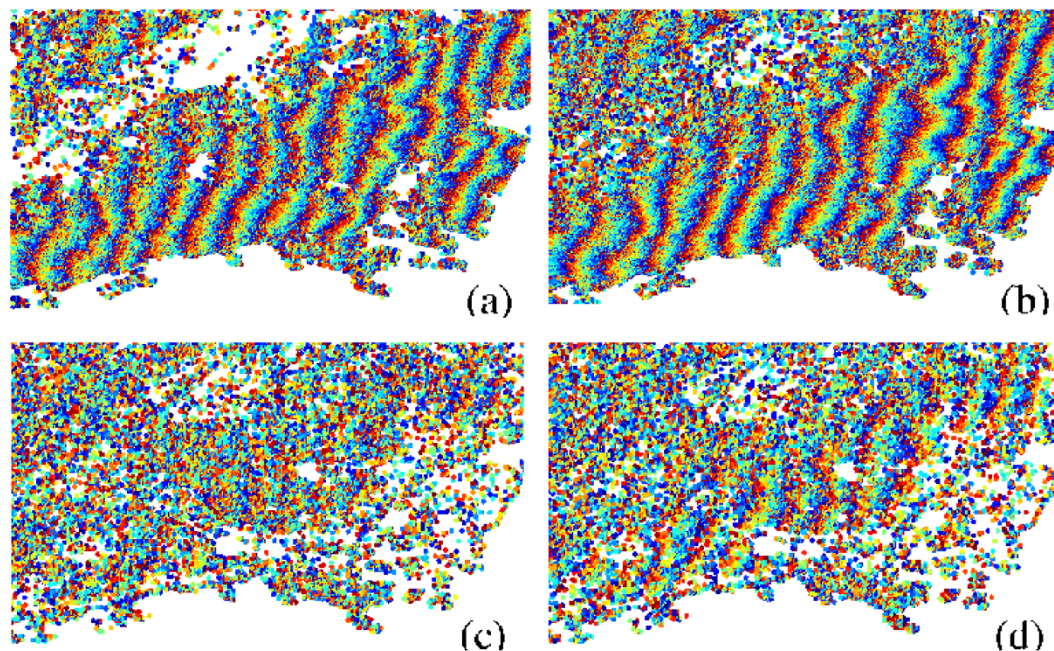


**Figure 3.5. Example of an interferogram formed between dates 2008/06/13-2011/03/18 for the close up region in Figure 3.1. (a-b) refer to the HH and optimized interferograms for pixels marked as PCs in each channel. (c-d) refer to the HH and optimized interferograms for pixels only marked as PCs in the optimized channel. Comparison of the interferograms shows that the main features of interferograms are preserved after application of PolInSAR technique. Comparing (c) and (d) shows that the quality of phase improves after application of PolInSAR technique.**

Figure 3.5 shows an interferogram between dates 2008/06/13-2011/03/18 for the enclosed region displayed in Figure 3.1. This interferogram has a perpendicular baseline of 227 meters and a temporal baseline of 1008 days. After removal of topographic and flat earth phase components, the interferogram is dominated by a residual orbital component. To test the influence of the technique on the phase stability, we analyze the phase pattern, e.g. the residual orbital ramps.

Figure 3.5 (a-b) depicts the phase map for a segment of urban region with HH average coherence above 0.3, retrieved from the HH and optimized channels, respectively. These

results show that the main interferogram features are well-preserved after coherence optimization. In addition, the optimized phase patterns are slightly improved. To better show the phase quality improvement, we display the HH and optimized phases for pixels with average optimized coherence above 0.3 that were not selected with the previous HH coherence mask (Figure 3.5 (c-d)). Here we clearly observe that the optimized interferograms increase the quality of the phase patterns with respect to HH phases. As a result, the apparent increase in phase stability of the PolInSAR phase enhances the performance of multibaseline DInSAR, e.g. for better phase unwrapping

### 3.5. Conclusion

Here, for the first time, we have applied the ESM-MB coherence optimization technique to satellite quad-pol images in order to increase the quality of the interferograms and retrieve a higher number of coherent pixel candidates. The optimized interferograms provide a higher number of PCs which are not detected in any single-pol channels. In addition, we separately investigated the performance of the technique for urban and rural subregions. This improvement of coherence is shown to be dependant on the interferometric spatial and temporal baselines, and this varies with subregion. Generally, for a very short temporal or spatial baseline interferograms, we observe a smaller coherence increment. Moreover, analysis of the optimized scattering mechanisms shows that most of the newly detected PCs in both rural and urban subregions correspond to the even bounce scattering types. These features are from man-made structures, which are more abundant in urban than rural subregions. Coherence optimization further improves scattering types in rural subregion which are associated with rough surfaces.

The presented technique provides a promising method to recover more stable phase patterns (e.g., ground deformation) through the exploitation of fully polarized SAR images. In the future, we will compare the PolInSAR – ESM-MB and classical DInSAR techniques using single pol-SAR data in order to fully illustrate the benefits of the proposed technique for ground deformation applications.

### 3.6. Acknowledgment

Images were acquired under SOAR-E project 5024 from the Canadian Space Agency. This research was funded by the NSERC and Aon Benfield/ICLR IRC in Earthquake Hazard Assessment, an NSERC Discovery Grant, and an Ontario Early Researcher Award.

### 3.7. References

- Adam, N., Kampes, B. & Eineder, M. 2005. Development of a scientific permanent scatterer system: Modifications for mixed ERS/ENVISAT time series. *Eur. Space Agency Spec. Publ.*, ESA SP-572, 457-465
- Berardino, P., Fornaro, G., Lanari, R. & Sansosti, E. 2002. A new algorithm for surface deformation monitoring based on small baseline differential SAR interferograms. *IEEE Trans. Geosci. Remote Sens.* **40**, 11, 2375-2383
- Bürgmann, R., Fielding, E. & Sukhatme, J. 1998. Slip along the Hayward fault, California, estimated from space-based synthetic aperture radar Interferometry. *Geology*, **26**, **6**, 559-562
- Cloude, S. R. & Papathanassiou, K. P. 1998. Polarimetric SAR Interferometry. *IEEE Trans. Geosci. Remote Sens.*, **36**, 5, 1551-1565
- Cloude, S.R. & Pottier, E. 1997. An entropy based classification scheme for land applications of polarimetric SAR. *IEEE Trans. Geosci. Remote Sensing*, **35**, 68-78
- Colin, E., Titin-Schnaider, C. & Tabbara, W. 2006. An interferometric coherence optimization method in radar polarimetry for high-resolution imagery. *IEEE Trans. Geosci. Remote Sens.*, **44**, 1, 167-175

- Ferretti, A., Prati, C. & Rocca, F. 2001. Permanent scatterers in SAR interferometry. *IEEE Trans. Geosci. Remote Sens.*, **39**, 1, 8-20
- Hooper, A., Segall, P. & Zebker, H. 2007. Persistent Scatterer InSAR for Crustal Deformation Analysis, with Application to Volcán Alcedo, Galápagos. *J. Geophys. Res.*, **112**, B07407, doi:10.1029/2006JB004763
- Lanari, R., Casu, F., Manzo, M. & Lundgren, P. 2007. Application of SBAS DInSAR technique to fault creep: A case study of the Hayward Fault, California. *Remote Sens. Environ.*, **109**, 1, 20-28
- Navarro-Sanchez, V.D., Lopez-Sanchez, J. M. & Vicente-Guijalba, F. 2010. A Contribution of Polarimetry to Satellite Differential SAR Interferometry: Increasing the Number of Pixel Candidates. *IEEE Geosci. Remote Sens. Lett.*, **7**, 2, 276-280
- Neumann, M., Ferro-Famil, L. & Reigber, A. 2008. Multibaseline polarimetric SAR interferometric coherence optimization. *IEEE Geosci. Remote Sens. Lett.*, **5**, 1, 93-97
- Papathanassiou, K. P. & Cloude, S.R. 2001. Single-baseline polarimetric SAR Interferometry. *IEEE Trans. Geosci. Remote Sens.*, **39**, 11, 2352-2363
- Qong, M. 2005. Coherence Optimization Using the Polarization State Conformation in PolInSAR. *IEEE Geosci. Remote Sens. Lett.*, **2**, 3, 301-305
- Samsonov, S. & Tiampo, K. 2011. Polarization phase difference analysis for selection of persistent scatterers in SAR Interferometry. *IEEE Geosci. Remote Sens. Lett.*, **8**, 2, 331-335

**Table S1. Spatial and temporal separation of Interferograms**

Master	Slave	Spatial Baseline (Meters)	Temporal Baseline (Days)
20080426	20080613	156.6570	48
20080426	20080707	210.7796	72
20080426	20080731	142.7326	96
20080426	20081222	151.5336	240
20080426	20090115	133.8975	264
20080426	20100907	211.6105	864
20080426	20101001	96.7075	888
20080426	20101025	99.5746	912
20080426	20101118	174.0925	936
20080426	20101212	28.9372	960
20080426	20110105	137.3321	984
20080426	20110129	175.3234	1008
20080426	20110222	54.8600	1032
20080426	20110318	383.9870	1056
20080613	20080707	54.1226	24
20080613	20080731	13.9244	48
20080613	20081222	5.1234	192
20080613	20090115	22.7595	216
20080613	20100907	54.9535	816
20080613	20101001	59.9495	840
20080613	20101025	57.0824	864
20080613	20101118	17.4355	888
20080613	20101212	127.7198	912
20080613	20110105	19.3249	936
20080613	20110129	18.6664	960
20080613	20110222	101.7970	984
20080613	20110318	227.3300	1008
20080707	20080731	68.0470	24
20080707	20081222	59.2460	168
20080707	20090115	76.8821	192
20080707	20100907	0.8309	792
20080707	20101001	114.0721	816
20080707	20101025	111.2050	840
20080707	20101118	36.6871	864
20080707	20101212	181.8424	888

Table S1 (Continued)

Master	Slave	Spatial Baseline (Meters)	Temporal Baseline (Days)
20080707	20110105	73.4475	912
20080707	20110129	35.4562	936
20080707	20110222	155.9196	960
20080707	20110318	173.2074	984
20080731	20081222	8.8010	144
20080731	20090115	8.8351	168
20080731	20100907	68.8779	768
20080731	20101001	46.0251	792
20080731	20101025	43.1580	816
20080731	20101118	31.3599	840
20080731	20101212	113.7954	864
20080731	20110105	5.4005	888
20080731	20110129	32.5908	912
20080731	20110222	87.8726	936
20080731	20110318	241.2544	960
20081222	20090115	17.6361	24
20081222	20100907	60.0769	624
20081222	20101001	54.8261	648
20081222	20101025	51.9590	672
20081222	20101118	22.5589	696
20081222	20101212	122.5964	720
20081222	20110105	14.2015	744
20081222	20110129	23.7898	768
20081222	20110222	96.6736	792
20081222	20110318	232.4534	816
20090115	20100907	77.7130	600
20090115	20101001	37.1900	624
20090115	20101025	34.3229	648
20090115	20101118	40.1950	672
20090115	20101212	104.9603	696
20090115	20110105	3.4346	720
20090115	20110129	41.4259	744
20090115	20110222	79.0375	768
20090115	20110318	250.0895	792
20100907	20101001	114.9030	24

Table S1 (Continued)

Master	Slave	Spatial Baseline (Meters)	Temporal Baseline (Days)
20100907	20101025	112.0359	48
20100907	20101118	37.5180	72
20100907	20101212	182.6733	96
20100907	20110105	74.2784	120
20100907	20110129	36.2871	144
20100907	20110222	156.7505	168
20100907	20110318	172.3765	192
20101001	20101025	2.8671	24
20101001	20101118	77.3850	48
20101001	20101212	67.7703	72
20101001	20110105	40.6246	96
20101001	20110129	78.6159	120
20101001	20110222	41.8475	144
20101001	20110318	287.2795	168
20101025	20101118	74.5179	24
20101025	20101212	70.6374	48
20101025	20110105	37.7575	72
20101025	20110129	75.7488	96
20101025	20110222	44.7146	120
20101025	20110318	284.4124	144
20101118	20101212	145.1553	24
20101118	20110105	36.7604	48
20101118	20110129	1.2309	72
20101118	20110222	119.2325	96
20101118	20110318	209.8945	120
20101212	20110105	108.3949	24
20101212	20110129	146.3862	48
20101212	20110222	25.9228	72
20101212	20110318	355.0498	96
20110105	20110129	37.9913	24
20110105	20110222	82.4721	48
20110105	20110318	246.6549	72
20110129	20110222	120.4634	24
20110129	20110318	208.6636	48
20110222	20110318	329.1270	24

## Chapter 4

### 4 Short-term surface deformation on the northern Hayward fault, CA, and nearby landslides using Polarimetric SAR Interferometry (PolInSAR)<sup>4</sup>

*In this chapter we use a polarimetric coherence optimization technique on RADARSAT-2 images in order to generate deformation maps which measure the creep on the Hayward fault and landslide motions near Berkeley, CA. This is the first application of multibaseline coherence optimization that compares the deformation map from quad-pol optimization with those of single-channel interferograms.*

*In this study, we apply the technique on SAR images from both ascending and descending geometries and use a Small Baseline (SBAS) technique to generate linear deformation maps for the region. Our results are in agreement with both earlier creep estimates and also the analysis of single-channel interferograms. With this technique, we resolve a greater quantity of reliable DInSAR measurement points. We further assess the quality of these newly selected coherent points. Our results demonstrate that PolInSAR is an effective method to increase the interferometric coherence and provide improved resolution of deformation features associated with natural hazards.*

---

<sup>4</sup> This manuscript has been accepted by the journal Pure and Applied Geophysics

#### 4.1. Introduction

The Hayward fault is a right-lateral strike-slip fault, part of the transform boundary in California, which is accommodating approximately twenty percent of the tectonic motion occurring between the Pacific and North American plates (Figure 4.1). According to paleoseismic studies performed along this fault, the northern section of Hayward fault has been inactive for more than three centuries. However, the southern section last ruptured in an  $M_w$  6.8 earthquake in 1886. Because the Hayward fault has been accumulating interseismic stress for such a long period of time, it is considered one of the greatest seismic hazards in the San Francisco region (Bürgmann et al. 1998).

One well-studied feature of Hayward fault is the creep phenomenon observed by the offset of man-made structures across the fault using alignment arrays (Lienkaemper et al. 1991). Those ground-based geodetic observations estimated the creep rates of 3-6 mm/year along most of the parts of the fault except for a segment near its south end that creeps at about 9 mm/year (Lienkaemper & Galehouse 1997). Geological observations based on the paleoseismic data indicate a larger long-term interseismic rate of 9 mm/year (Lienkaemper et al. 1991). Aseismic creep contributes to the release of tectonic stress which otherwise might be released during a big coseismic rupture. In order to better quantify the amount of stress released by fault creep, knowledge of a detailed fault friction structure (velocity-strengthening patches) at depth and their creeping rates are required. Subtraction of these rates from the long-term geological creep rates could provide the estimate of the slip deficit along the fault. This might be an upper bound for the next coseismic rupture on Hayward fault.

Various modeling techniques have been applied in order to link the depth and rate of creep events to those observations on the surface (Schmidt et al. 2005; Simpson et al. 2001; Malservisi et al. 2003; Evans et al. 2012; Tiampo et al. 2013; Shirzaei & Bürgmann 2013). By using only the small number of conventional geodetic techniques very general picture of fault slip is determined at depth. Additional constraints from the near- and far-field deformation is required in order to map in detail the subsurface fault behavior along the full seismogenic zone.

Another feature of the Hayward fault which is of importance in terms of hazard assessment arises from landslides along the Berkeley hills. The landslides may be exacerbated by slope changes due to tectonic movement of the Hayward fault in this region (Hilley et al. 2004). Hilley et al. (2004) used Coulomb Failure Function (CFF) and incorporated groundwater modifications due to the tectonic uplift in order to find the detachment zone. The simulated detachment zone correlates well with the location of the observed landslides mapped by interferometric technique.

Slope instabilities pose a significant threat to the urban infrastructure. As a result locating their exact position and monitoring their ongoing movement is of great importance. Furthermore, categorizing the type of landslide will have implications for the purpose of mitigation or prevention. A better strategy for the management of these hazards will be made if the kinematics of the slides is understood well.

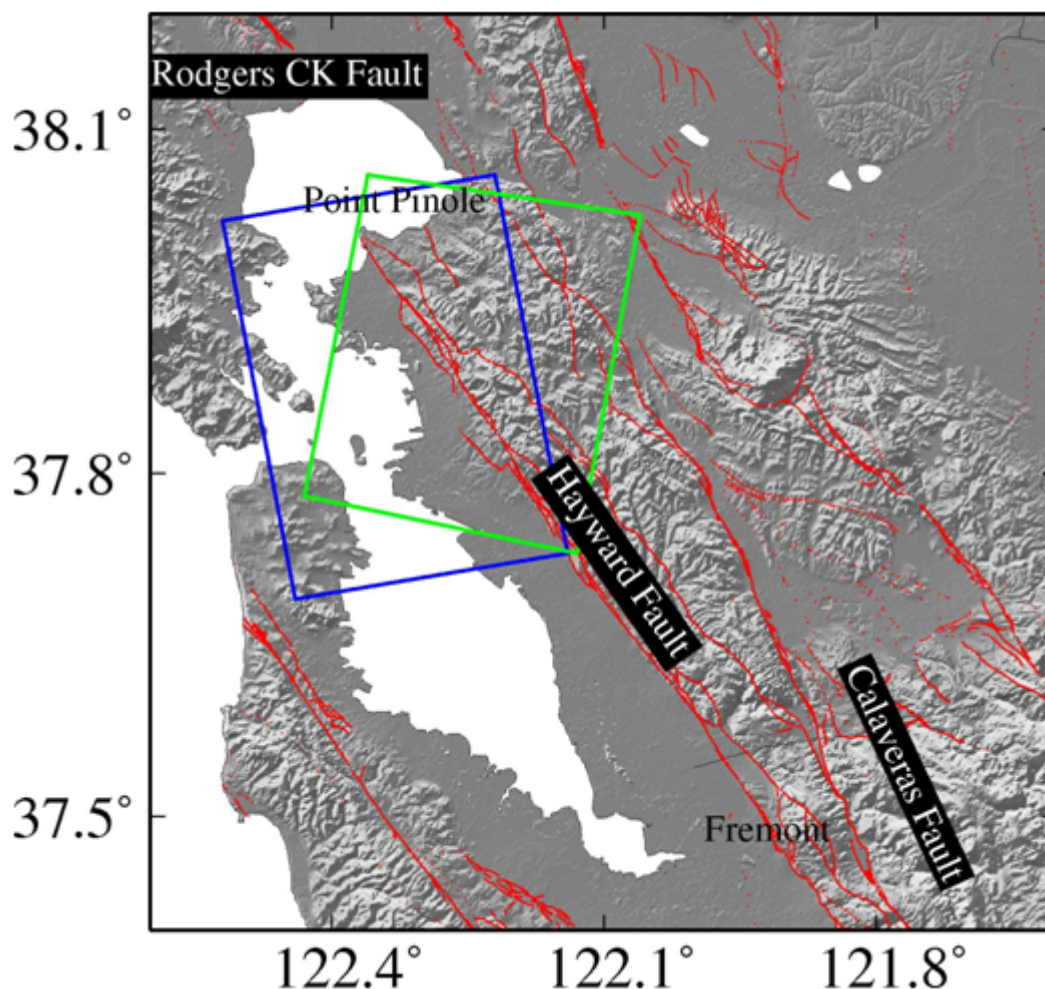


**Figure 4.1. SRTM Topography for the San Francisco region with RADARSAT-2 trajectories. The blue and green boxes mark the footprint of ascending and descending tracks, respectively. The red lines represent the faults in this region.**

Differential SAR Interferometry (DInSAR) was first applied by (Bürgman et al. 1998) to the Hayward fault in order to map the creep rate on a larger region of this fault. The technique has proven to be very powerful in providing the data for modeling the subsurface extent of Hayward fault in more detail (Schmidt et al. 2005). However, one limitation of DInSAR for deformation mapping in this region is the vegetation cover to the east of the fault. Temporal decorrelation which is caused by the instability of the scatterers in a resolution cell, from vegetated land cover limits our ability to obtain

reliable measurements. In the past decade, more sophisticated DInSAR algorithms also were applied for mapping of the Hayward fault regional deformation, including Permanent Scatterer Interferometric SAR (PS-InSAR) (Bürgmann et al. 2006). The technique solves for the temporal deformation rates on single scatterers which preserve a high backscattering properties over time. For example, the Berkeley landslides were first mapped by satellite imagery using PS-InSAR technique (Hilley et al. 2004).

In this paper, we present the results of Polarimetric SAR Interferometry (PolInSAR) for the first time on Hayward fault. PolInSAR is an advanced Interferometric SAR (InSAR) technique which can be used to maximize the interferometric coherence by combining the polarimetric and interferometric information of SAR imagery (Cloude & Papathanassiou 1998). The objective is to enhance the quality of DInSAR interferograms in the locations of higher decorrelation from vegetation. PolInSAR contributes to the increase of coherence, because the effect of the volume scattering can be minimized by selecting the optimum scattering mechanism while maximizing the backscattered power of the most coherent scatterers in a resolution cell. This is the first application of the technique for deformation studies using satellite quad polarization (quad-pol) imagery, which is only possible at present time by RADARSAT-2 satellite. We apply this technique in order to retrieve more measurement points for the regions which are mixed with vegetation. PolInSAR optimization is able to find the dominant and most coherent pixels in such mixed environments, resulting in less interferometric noise. In this approach we use twenty-five RADARSAT-2 images from 2008-2011 acquired in fine quad-pol mode and from ascending and descending geometries. Tiampo et al. (2013) employed a subset of these in separate, Polarization Phase Difference (PPD) incorporating phase information of the co-pol channels. Here we use both the amplitude and phase information by applying PolInSAR technique and compare our results with conventional interferometry using the same dataset of single-channel polarimetry. The results will be presented both for fault creep rates and landslide movement.

## 4.2. Region of Study

The Hayward fault is assigned the highest seismic hazard zone in the San Francisco Bay area. The fault is 100 km long and is connected in the north to Rodgers Creek fault and toward the south to the Calaveras fault (Lienkaemper et al. 1991). The fault accommodates 20% of the tectonic stress in San Francisco fault system. Seismic observations imply that Hayward dips to east and connect with Calaveras fault at depth (Williams et al. 2005). The observed creep rate is not uniform on the surface, being on the order of 3-5 mm/year in the north and 8mm/year to the south. The higher rates observed in the south might be linked to the connection of Hayward fault to the Calaveras fault and the slip transfer from the adjacent faults (Williams et al. 2005).

Several studies have inverted geodetic data and simulated dynamic models in order to better understand the pattern of locked and creeping patches on the fault at depth (Schmidt et al. 2005; Simpson et al. 2001; Malservisi et al. 2003; Evans et al. 2012; Tiampo et al. 2013; Shirzaei & Bürgmann 2013). Most of these studies commonly point at a locked patch starting from San Leandro in the north to Fremont in the south, which is assigned a minimal creep rate compared to its surrounding. They further imply that this locked patch coincides with the location of  $M_w$  6.8, 1868 earthquake (Evans et al. 2012).

Important questions remain regarding the potential hazard along the Hayward fault. Savage & Lisowski (1993) estimated that Hayward fault is capable of generating one  $M_w$  6.8 event per century. However, Lienkaemper & Galehouse (1998) estimated a larger  $M_w$  7 for the next possible seismic event on the Hayward fault. Furthermore, it is unclear whether the rupture in such an event also will propagate into the creeping sections or only will be limited to the locking patches of the fault (Simpson et al. 2001). Time-dependant inversion of InSAR data show that the magnitude of the next seismic event varies between 6.3  $M_w$  to 6.8  $M_w$ , depending on the extent of the rupture propagation (Shirzaei & Bürgmann 2013).

Aside from the seismic hazard of the Hayward fault, landslides pose an additional threat to the infrastructure in the urban region of Berkeley. Berkeley landslides are

located along the Hayward fault to the west and show a NE-SW direction. These landslides have been documented already by field investigations (USGS Earthquake Hazard Program 1999) and have been categorized as highly active and moderately active based on their previous movement. PS-InSAR (Hilley et al. 2004) was applied to these landslides to map their movement over a 9 year period from 1999-2001. According to that study, the landslide movements may be exacerbated by slope changes due to tectonic movement of the Hayward fault in this region (Hilley et al. 2004). They further suggest that there is a nonlinear relationship between the rate of landslide movement and the seasonal precipitation.

Here we investigate the creep rate along the northern 35 km of the Hayward fault from Point Pinole to San Leandro. We use a PolInSAR coherence optimization technique and compare our results with the conventional DInSAR in order to measure the fault creep rate and the rate of movement of the Berkeley landslides.

### 4.3. Polarimetric SAR Interferometry (PolInSAR)

Coherence optimization of Polarimetric SAR Interferometry (PolInSAR) was introduced by Cloude & Papathanassiou (1998) and expanded by others (Colin et al. 2006; Qong 2005). In recent years, PolInSAR has been applied to the field of DInSAR for measuring ground deformation (Navarro-Sanchez et al. 2010; Navarro-Sanchez & Lopez-Sanchez 2012). In these studies, the goal was to increase the number of coherent pixels by finding the optimum scattering mechanisms in a resolution cell through analysis of an average target's coherency matrix. Recent PolInSAR studies have shown that selecting optimum polarimetric channels reduces interferometric decorrelation noise and gives a more precise estimation of surface deformation (Alipour et al. 2013).

In polarimetric SAR, the scattering matrix ( $k$ ) is expressed as a vector using the Pauli basis (Cloude & Papathanassiou 1998),

$$k_i = \frac{1}{\sqrt{2}} [S_i^{HH} + S_i^{VV}, S_i^{HH} - S_i^{VV}, 2S_i^{HV}]^T \quad (4.1)$$

where the  $S_i^{HH}$  and  $S_i^{VV}$  are co-polar terms and  $S_i^{HV}$  is the cross-polar term of the  $2 \times 2$  scattering matrix, measured by fully polarimetric sensors.  $i$  is the number corresponding to each quad-pol set and  $T$  is the transpose operator.

Coherence optimization is a technique applied to polarimetric SAR data, where the optimum scattering mechanisms ( $\omega$ ) are resolved from average target's coherency matrices. By changing the polarization basis for the SAR images following (4.2), the new SAR image is given by ( $\lambda$ )

$$\lambda_i = \omega_i^{*T} k_i \quad (4.2)$$

In these equations  $*$  is the complex conjugate operator. Interferometric coherence,  $\gamma_{ij}(\omega_i, \omega_j)$ , is calculated for two sets of SAR images in any arbitrary polarimetric basis defined by  $\omega_i$  and  $\omega_j$  as (4.3) (Neumann et al., 2008)

$$\gamma_{ij}(\omega_i, \omega_j) = \frac{\omega_i^{*T} \Omega_{ij} \omega_j}{\sqrt{\omega_i^{*T} T_{ii} \omega_i \omega_j^{*T} T_{jj} \omega_j}} \quad (4.3)$$

$T_{ii}$  is the coherency matrix for a polarimetric SAR image  $i$  and  $\Omega_{ij}$  is the coherency matrix between two SAR images of  $i$  and  $j$ . In a coherence optimization problem, we find  $\omega_i$  and  $\omega_j$  such that the corresponding coherence is maximized.

Coherence optimization in the field of Multi-Baseline DInSAR (MB-DInSAR) can only be implemented by an optimization procedure which insures the consistency of the optimum scattering mechanisms of a target for a single SAR scene among different interferograms. Otherwise, a residual phase will be added which will bias the interferometric phase due to ground deformation. The approach presented in Neumann et al. (2008) solves this problem and is known as Multi-Baseline PolInSAR (MB-PolInSAR) coherence optimization. This methodology optimizes scattering mechanisms by a simultaneous inversion among multiple interferograms and accordingly can be applied to multibaseline DInSAR applications. The maximization of coherence is done by selecting those scatterers in the resolution cell which maintain the highest mean coherence over a number of interferograms.

According to (Neumann et al. 2008), there are two approaches to solve a MB-PolInSAR coherence optimization problem; Equal Scattering Mechanism (ESM) and Multiple Scattering Mechanism (MSM) solution. The former case constrains the two scattering mechanisms to be equal, at both ends of baseline ( $\omega_1 = \omega_2$ ), while the later is a generalized form of coherence optimization problem where no constraint on the equality of two scattering mechanisms is imposed (Neumann et al. 2008).

We applied the ESM technique for the first time on a quad-pol dataset of RADARSAT-2 and showed that the technique increases the number of coherent points in an interferogram and enhances the accuracy of the interferometric phase (Alipour et al. 2013). The ESM technique is preferred to the MSM technique for DInSAR applications because the selection of different scattering mechanisms for the latter can lead to amplification of noise, generating a bias for the interferometric phase. Here we continue the previous study and present our new results on the implementation of the MB-ESM technique to obtain the deformation rates in the northern Hayward fault region.

#### **4.4. Application of PolInSAR**

Here we apply the multibaseline ESM technique on 25 quad-pol images of RADARSAT-2. Details of the processing are the same as those found in Alipour et al. (2013), where we only used the descending subset of these images for analysis. These images cover only the northern 35 km of the Hayward fault from Point Pinole in the north to San Leonardo in the south (Figure 4.1). The images are acquired from two tracks with ascending and descending geometries between 2008 and 2011. The ascending and descending geometries are acquired with incident angles of  $36^\circ$  and  $28^\circ$ , respectively. Fifteen SAR images in descending trajectory were acquired at the following dates: 2008/04/26, 2008/06/13, 2008/07/07, 2008/07/31, 2008/12/22, 2009/01/15, 2010/09/07, 2010/10/01, 2010/10/25, 2010/11/18, 2010/12/12, 2011/01/05, 2011/01/29, 2011/02/22, and 2011/03/18. Ten ascending SAR images were acquired on: 2008/06/13, 2008/07/07, 2008/07/31, 2008/12/22, 2009/01/15, 2010/08/14, 2010/09/07, 2010/10/01, 2010/11/18 and 2010/12/12. PPD, a Polarimetric Phase Difference technique, was applied to the descending subset of these images in order to study the creep rate from 2008-2011

(Tiampo et al. 2013). Here we use the SAR images corrected for precise orbits and apply the PolInSAR coherence optimization in order to map the current fault creep and landslide motions in this region.

Because of the orientation of the Hayward fault and the sense of motion along that (strike-slip fault), deformation signals are mapped onto the Line-of-Sight (LOS) of descending interferograms. The ascending interferograms are less sensitive to the fault motion because the ground surface moves mainly perpendicular to the LOS of polar orbit satellite. However, we used ascending data for mapping the rate of landslide motion. Multiple view angles would allow understanding better the landslide kinematics.

In the first step, we used HH and VV images in order to form the interferograms in both sets of ascending and descending geometries. The total numbers of interferograms for each channel in the descending and ascending geometries are 105 and 45, respectively. The precise orbits for the images are provided by Canadian Space Agency (CSA). The interferograms were formed by using a window of  $5 \times 10$  pixels in range and azimuth direction, resulting in final ground resolution of  $24 \times 47$  meters. We used an SRTM Digital Elevation Model (DEM) with 30 meters of spatial resolution to correct for the topographic phase. In order to separate the coherent pixels with good phase quality, we use the mean coherence criterion among all the interferograms (Adam et al. 2005). A coherence threshold of 0.3 was assigned for separation of the coherent and incoherent pixels. Later, we applied a Small Baseline (SBAS) technique, as developed by (Berardino et al. 2002) and modified by (Samsonov et al. 2011), to the generated interferograms in order to produce the linear velocity maps from the time series results and solve for the topographic errors. As we have three years of SAR data, the assumption of a linear velocity is justified for the short-term creep rates on the Hayward fault (Tiampo et al., 2013).

The deformation velocities have an additional long-term component of interseismic stress accumulation from the Hayward fault and other neighboring faults. The separation of this long-wavelength interseismic signal is difficult from the interferometric residual orbital ramps. Accordingly, to estimate the orbital ramp, we first modeled and removed

the interseismic deformation using a deep dislocation model in half-space on the Hayward fault (Okada 1992). The rate for the deep dislocation stress accumulation is 10 mm/year (Smith et al. 2005). We assumed that the effect of the neighboring faults are very small and below the DInSAR detection limit. We projected the modeled rates to LOS direction and removed them from the surface velocity maps. The results were further refined for the residual orbits resulting from inaccuracies in the position of the SAR satellite. After the orbital correction, the interseismic rates were added back to the linear velocity maps. Figure 4.2 represent the deformation due to tectonic origin, both the deep interseismic stress accumulation rates and the shallow creep rates.

We use optimization of equation (4.2) on both sets of SAR images on a pixel-by-pixel basis. The ESM technique was applied to derive the optimum scattering mechanisms ( $\omega$ ) with multilooking factor of 5 and 10 pixels in range and azimuth directions, respectively. The optimum scattering mechanism were applied to the scattering vectors ( $k$ ) corresponding to each SAR image in order to transform the images in (H,V) basis to the optimized basis. Later, these new optimized images were used to form the same number of interferograms as mentioned above. The SBAS processing was performed on the PolInSAR interferograms to derive the linear velocity rates and solve for the residual topographic errors. Residual orbital ramps were removed from the linear velocity maps as explained above for single-channel HH and VV dataset.

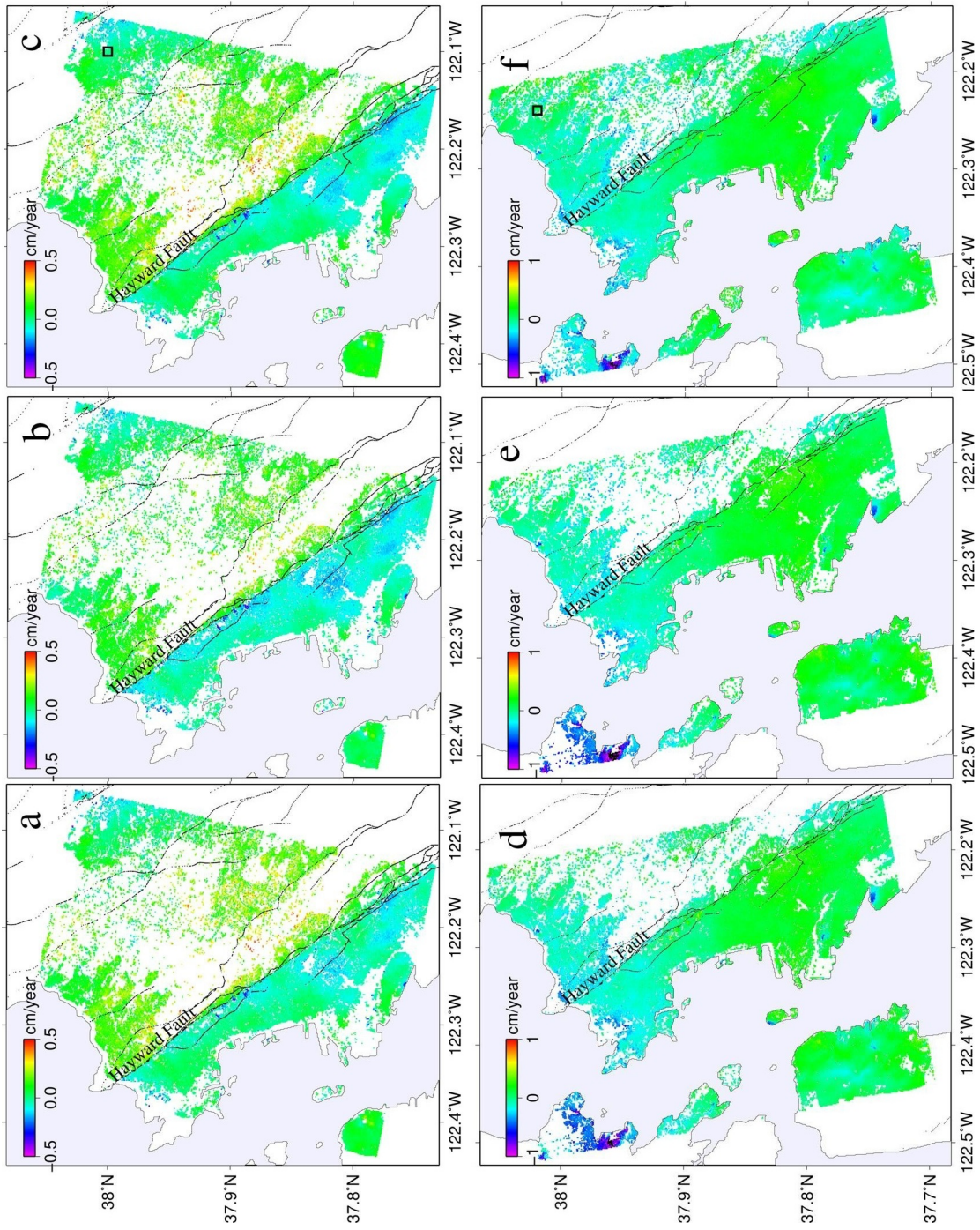


**Figure 4.2. Linear deformation map derived from SBAS technique by using single-channel HH dataset for the (a) descending (d) ascending tracks. Linear deformation map derived from SBAS technique by using single-channel VV dataset for the (b) descending (e) ascending tracks. Linear deformation map derived from SBAS technique by using the optimized channel for the (c) descending (f) ascending tracks. Note that here the LOS shortening is represented by positive and LOS lengthening is represented by negative values. The black lines represent the faults in this region, as in Figure 4.1. The black squares in (c) and (f) mark the reference region for calibration of DInSAR images in the descending and ascending geometries, respectively.**

## **4.5. Results**

### **4.5.1. Creep along North Hayward Fault**

Here we present the results which compare the PolInSAR analysis with single polarimetric channel analysis. Figure 4.2 (a) and (d) shows the linear deformation map derived from SBAS technique by using single-channel HH dataset for the (a) descending (d) ascending tracks. Figure 4.2 (b) and (e) shows the linear deformation map derived from SBAS technique by using single-channel VV dataset for the (b) descending (e) ascending tracks. Figure 4.2 (c) and (f) shows the linear deformation map derived from SBAS technique by using the optimized channel for the (c) descending (f) ascending tracks. Note that here the LOS shortening is represented by positive and LOS lengthening is represented by negative values. The black squares in (c) and (f) mark the reference region for DInSAR images in the descending and ascending geometries, respectively. In these maps we observe that there is a phase discontinuity across the Hayward fault, expressing the right-lateral creep along the Hayward fault. The deformation rate differences in the top left part (NW corner) of the interferograms is due to the discontinuities in the phase unwrapping.

In order to analyze the fault creep we plot profiles across the fault, as shown in Figure 4.4, locations marked as red lines in Figure 4.3. The deformation along all of these profiles has a discontinuity at 0 km, on the Hayward fault. This discontinuity is sharper in the north (profiles 1-5) than to the south of the fault. Profiles 1-5 show  $\sim 2$ - $2.5$  mm/year of LOS displacement, while the southern profiles show an LOS displacement of  $\sim 1.5$ - $2$  mm/year. Projecting this onto the horizontal component yields  $\sim 4$ - $5$  mm/year of surface creep in the northern part of the fault and  $\sim 3$ - $4$  mm/year in the south, assuming that the vertical motion is negligible.

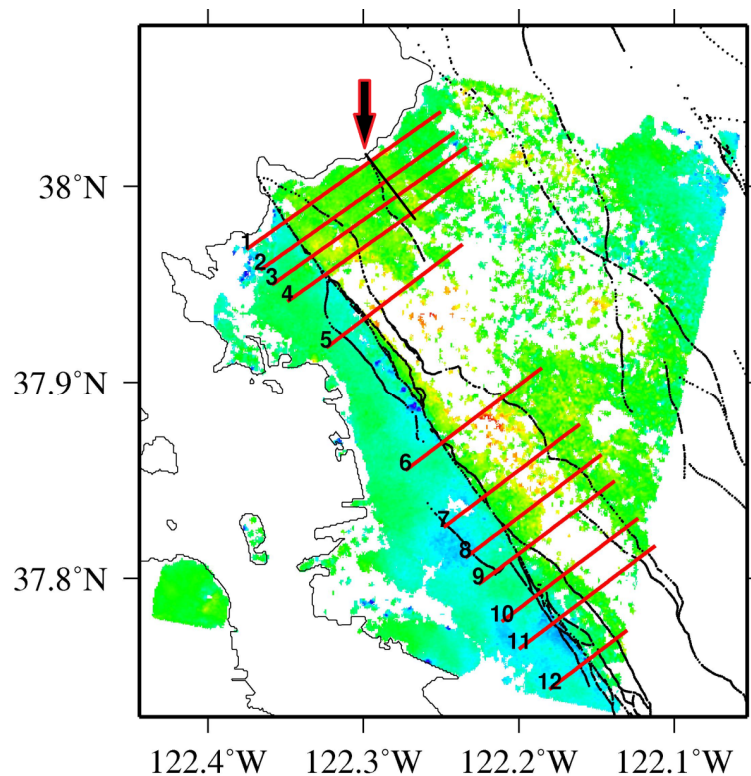


**Figure 4.3. Location of profiles in the PolInSAR deformation map from the optimized channel marked by red lines and the numbers associated with each. The deformation rate along these profiles is presented in Figures 4.4-4.5. The black lines represent the faults in this region, as in Figure 4.1. The black line parallel to the Hayward fault in the north (identified by the black arrow) represents the location of a secondary fault that may experience creep events.**

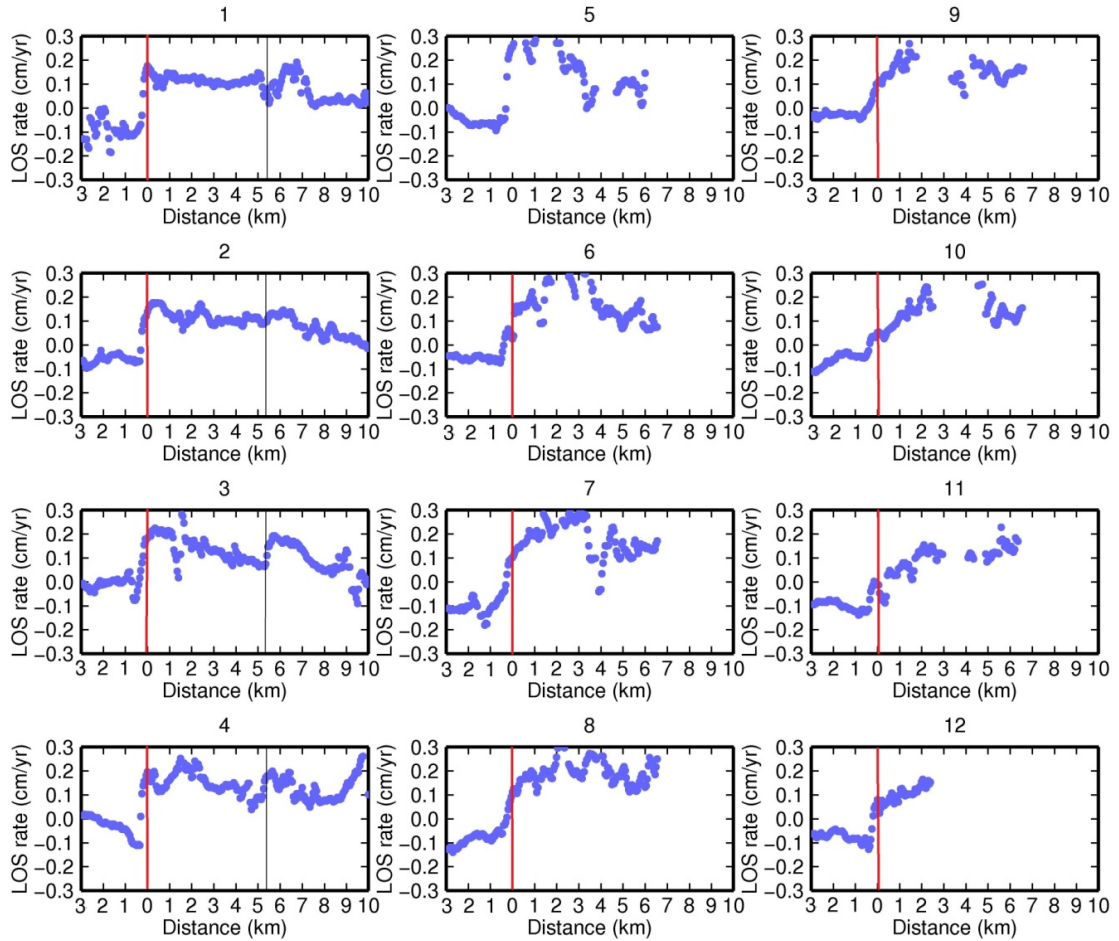


**Figure 4.4. Linear rate of deformation along profiles in Figure 4.3, derived from descending images. The horizontal axis represents distance from Hayward fault. The red line marks the location of Hayward fault. The black line in profiles (1-4) might be another fault parallel to the Hayward fault in the north (the location is shown in Figure 4.3).**

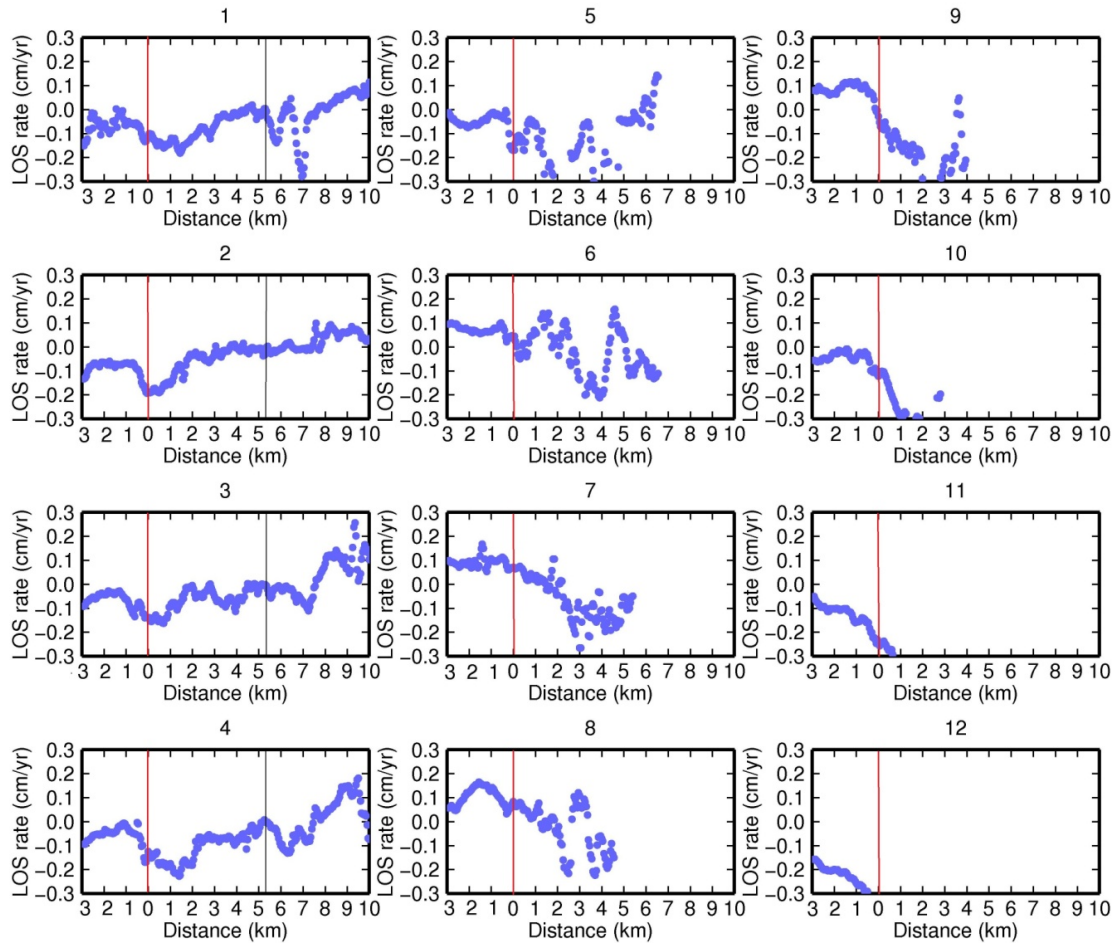


**Figure 4.5. Linear rate of deformation along profiles in Figure 4.3, derived from ascending images. The horizontal axis represents distance from Hayward fault. The red line marks the location of Hayward fault. The black line in profiles (1-4) might be another fault parallel to the Hayward fault in the north (the location is shown in Figure 4.3).**

Looking at the linear deformation map produced by the ascending geometry, we do not observe a sharp discontinuity for most of the sections of the fault (Figure 4.2). This is due to the insensitivity of the ascending geometry to the motion along strike. We further plot the linear rate of displacement from ascending geometry for the same profiles in Figure 4.3 (Figure 4.5). There is only 1 mm/year of displacement visible at the Hayward fault. Without prior knowledge of the fault location, it is very difficult to distinguish this fault-induced creep from the DInSAR noise, in the ascending interferograms. Analogous to the profiles from descending trajectory (Figure 4.4), the ascending profiles (Figure 4.5) show higher rates for the profiles associated with the northern part of the fault than the southern profiles.

Comparison of HH and PolInSAR derived deformation maps (Figure 4.2) shows that PolInSAR technique results in higher number of reliable points. As explained before, the eastern portion of the Hayward fault is dominated by vegetation, while the western area is the residential and urban region. The newly selected points are scattered in the vegetated as well as the urban part of the image. This contributes to a higher number of measurement points in the regions of higher decorrelation. This additional information is quantified in more detail in Alipour et al. (2013).

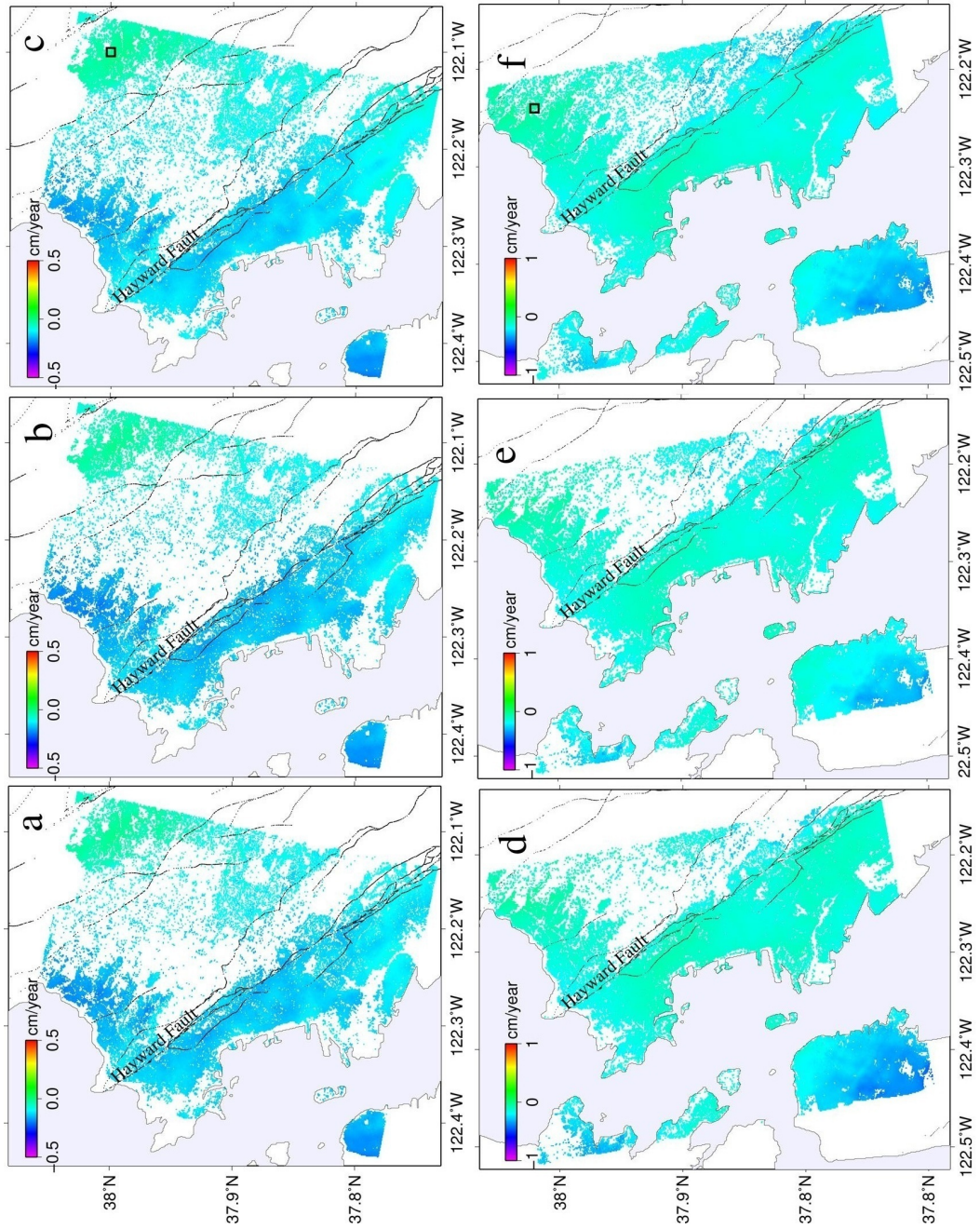


**Figure 4.6. Residual errors of linear deformation map derived from SBAS technique by using single-channel HH dataset for the (a) descending (d) ascending tracks. Residual errors of linear deformation map derived from SBAS technique by using single-channel VV dataset for the (b) descending (e) ascending tracks. Residual errors of linear deformation map derived from SBAS technique by using the optimized channel for the (c) descending (f) ascending tracks. Note that here the LOS shortening is represented by positive and LOS lengthening is represented by negative values. The black lines represent the faults in this region, as in Figure 4.1. The black squares in (c) and (f) mark the reference region for calibration of DInSAR images in the descending and ascending geometries, respectively.**

In order to assess the quality of the newly selected points, we investigate the residual errors from the linear trend of SBAS technique. Figure 4.6 shows these errors by (a) and (d) using single-channel HH dataset for the (a) descending (d) ascending tracks. Figure 4.6 (b) and (e) are errors by using single-channel VV dataset for the (b) descending (e) ascending tracks. Figure 4.6 (c) and (f) are errors by using the optimized channel for the (c) descending (f) ascending tracks. Note that here the LOS shortening is represented by positive and LOS lengthening is represented by negative values. It is clear that the error profile of the points selected after optimization are of the same orders as the points at their vicinity which are previously selected by HH channel. This means that adding the new points does not change or bias the linear rates for fault creep. More results on this will be presented in section 4.6.

#### **4.5.2. Landslide Motion**

Here we present the results associated with the Berkeley landslides along the Hayward fault. In this section, we only focus on a small region of these slides. We produced linear deformation maps from both the ascending and descending geometries in order to gain a

better understanding of the type of landslide motion by separating the vertical and horizontal components of the displacement.

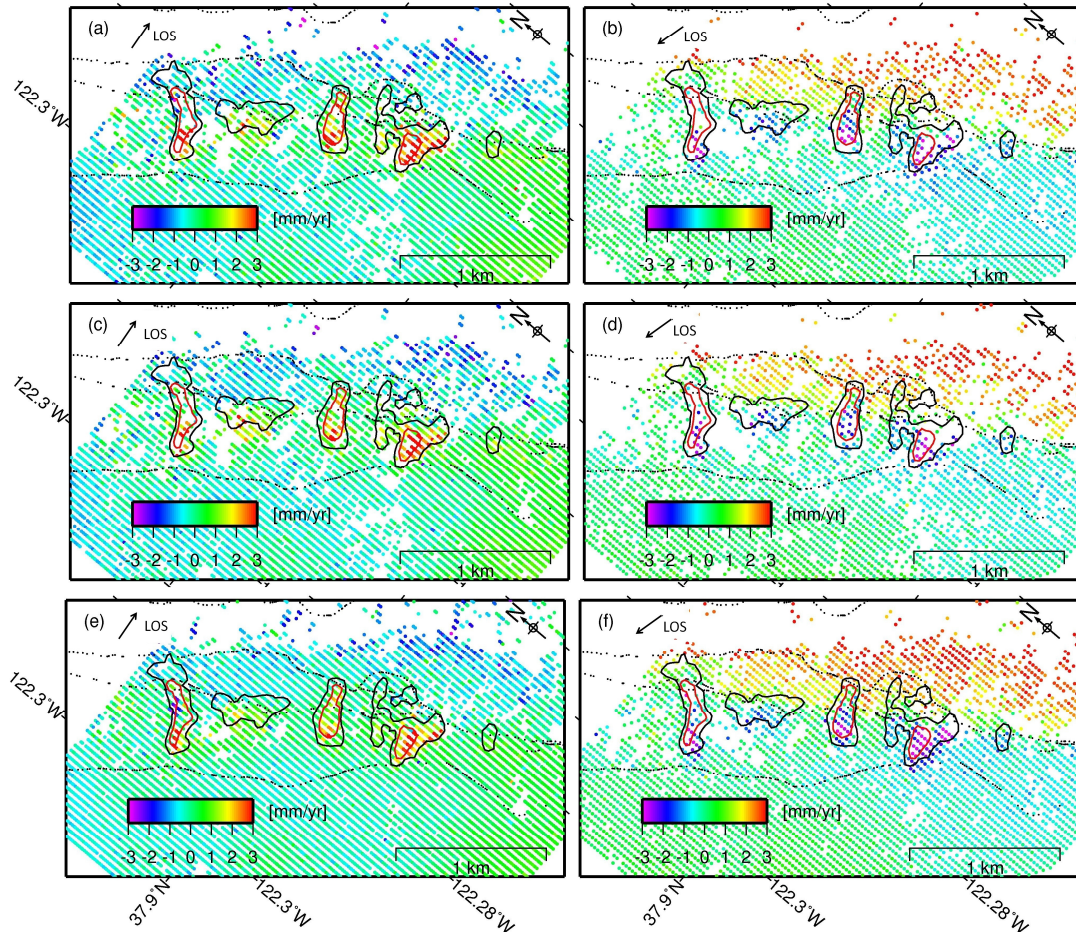


**Figure 4.7. LOS linear displacement maps for the Berkeley landslides: Figures (a), (c) and (e) are the maps from ascending images derived from (a) the HH, (c) the VV and (e) the PolInSAR optimized channel. Figures (b), (d) and (f) show the corresponding maps from descending images derived from (b) the HH, (d) the VV and (f) the PolInSAR optimized channel. Note that positive displacement represents motion toward the satellite. The black and red polygons outline the location of moderately active and highly active slope instabilities (USGS Earthquake Hazard Program 1999). The black dashed lines represent the faults in this region, as in Figure 4.1.**

Figure 4.7 shows the LOS displacement maps for these landslides. In these figures (a), (c) and (e) are the maps from ascending images derived from (a) the HH, (c) the VV and (e) the PolInSAR optimized channel. Figures (b), (d) and (f) show the corresponding maps from descending images derived from (b) the HH, (d) the VV and (f) the PolInSAR optimized channel. We observe that the ascending and descending trajectories show the same pattern for movement of the slides. However, due to the different imaging geometry, most of the landslides are marked by range shortening (positive) in ascending and range lengthening (negative) in descending geometries. The patterns that we have found for landslide locations match the ones earlier published by Hilley et al. (2004). Our mapped landslides coincide with the location of those from USGS Earthquake Hazard Program (1999), as well. Four different landslides are mapped by USGS Earthquake Hazard Program (1999) as in Figure 4.7. In this figure the red and black polygons outline the highly active and moderately active slope instabilities.

Inspection of Figure 4.7 demonstrates that the landslide maps produced from single-channel (HH or VV) data lack a significant number of points associated with the location of the highest displacement rates. In Figure 4.7 (e) and (f) PolInSAR is shown to be an effective technique in resolving the motion on most of these points. Moreover, the more detailed patterns identified in the landslides using the PolInSAR technique are more similar to those mapped by field investigations. For example, the northern most active landslide has an elongated shape which matches the PolInSAR pattern than the one from single-pol HH or technique. There is a 7-10% of increase in the number of coherent pixels for this area, which are not selected by any single-channel (HH,VV,VH) images. This results from the better phase accuracy of PolInSAR after integration of three different polarimetric channels and the identification of new reliable pixels.

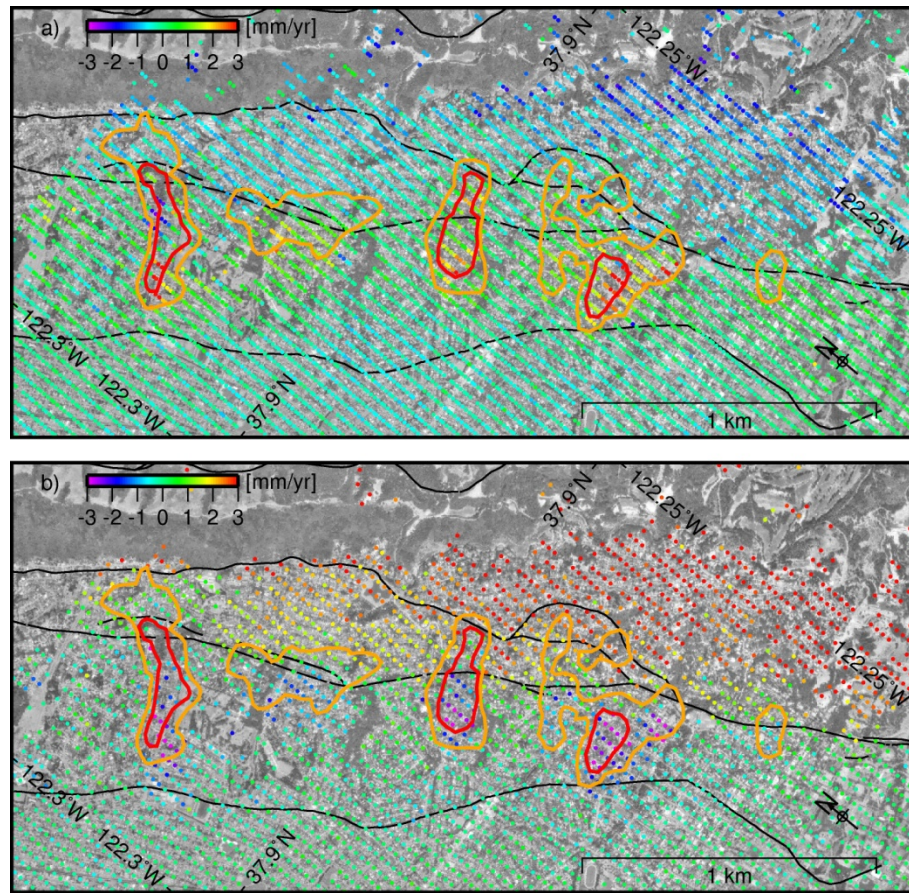


**Figure 4.8. Optimized linear deformation maps for (a) ascending (b) descending tracks, overlaid on an aerial photography. The orange and red polygons outline the location of moderately active and highly active slope instabilities (USGS Earthquake Hazard Program 1999). The black lines represent the faults in this region, as in Figure 4.1.**

Figure 4.8 is the LOS deformation from PolInSAR optimized channels for the (a) ascending (b) descending images, overlaid on an aerial photo. By comparing the ascending and descending maps in Figure 4.7-4.8, we observe that the northernmost landslide is subject to range lengthening in both the ascending and descending datasets in the middle of the landslide. However, the foot of the slide is subject to range lengthening and range shortening in both the descending and ascending datasets, respectively. We conclude that for this landslide, the middle part is displaced primarily in the vertical direction and the foot of the slide is displaced horizontally. This pattern is similar to rotational type landslides; however, here the slide is very long and the pattern along most of its length is translational. Inspection of the other landslides along the fault shows a constant range lengthening in the descending datasets and range shortening in the ascending datasets. This implies that the rest of these slope instabilities are translational types of landslide, where all the material moves along a plane with a constant slope.

The maximum rate of motion of 35 mm/year along the hill slope was previously documented by (Hilley et al. 2004). Here, our estimated landslide motion along the hill slope, assuming a fixed slope of 4 degrees, is 23 mm/year. In general, due to lower accuracy of single-channel (HH or VV) dataset, and a small number of points, it is difficult to distinguish the exact location and motion of the landslide. By applying PolInSAR technique a clear pattern of deformation is recognized using DInSAR techniques.

#### **4.6. Discussion**

Our estimates show a creep rate of 3-5 mm/year along the surface of the Hayward fault for the northern 35 km. These rates are more pronounced in the northern 5 km of the fault and the observed phase discontinuity is much sharper in this region. We speculate that this sharp phase gradient in the north is due to the fact that creep extends deeper in this region. Previous studies have inverted for geodetic data and estimated that Hayward fault is creeping deeper in the north (Shirzaei & Bürgmann 2013; Bürgmann et al. 2000). Our

rates agree well with the previous study of Tiampo et al. (2013), which compared fault slip obtained from the PPD technique with those of the alignment array along the Hayward fault trace (Lienkaemper et al. 2012). Here, we should note that our observation period is limited to three years of data from 2008-2011, while most of the ground-based measurements estimate a long-term creep rates. In fact, the fault might undergo periods of short-term rate change and we could be observing these short-term fluctuations from a long-term trend (Tiampo et al. 2013).

We assume that there is a potential for fault creep on secondary faults close to the Hayward fault. The northern profiles (1-4) of Figures 4.4 and 4.5 show a discontinuity at 5-6 km (shown by black line in Figures 4.3-4.5) that is evident more on the descending dataset. We can trace this pattern on the ascending data too, but the phase jump is very small. They persist at one location along these four profiles. This discontinuity could be attributed to a secondary fault which is creeping parallel to Hayward in the north. This feature shows  $\sim 1$  mm/year of displacement in the LOS direction, which translates to  $\sim 1.5$  mm/year of horizontal displacement. However, a larger dataset of DInSAR data is necessary to investigate whether this discontinuity is observed through different and longer time periods or it is only an artificial fluctuation in the analyzed data.

In order to quantitatively analyze the additional accuracy that PolInSAR provides in comparison to the single-channel DInSAR, comparison with ground-truth data is required. However, here we show some promising results comparing PolInSAR to DInSAR for the well-studied Hayward fault. Analysis of the errors associated with the linear creep velocity show that the PolInSAR technique provides a greater number of points, while their errors are in the same order as those measurements from single-channel (HH or VV) dataset.

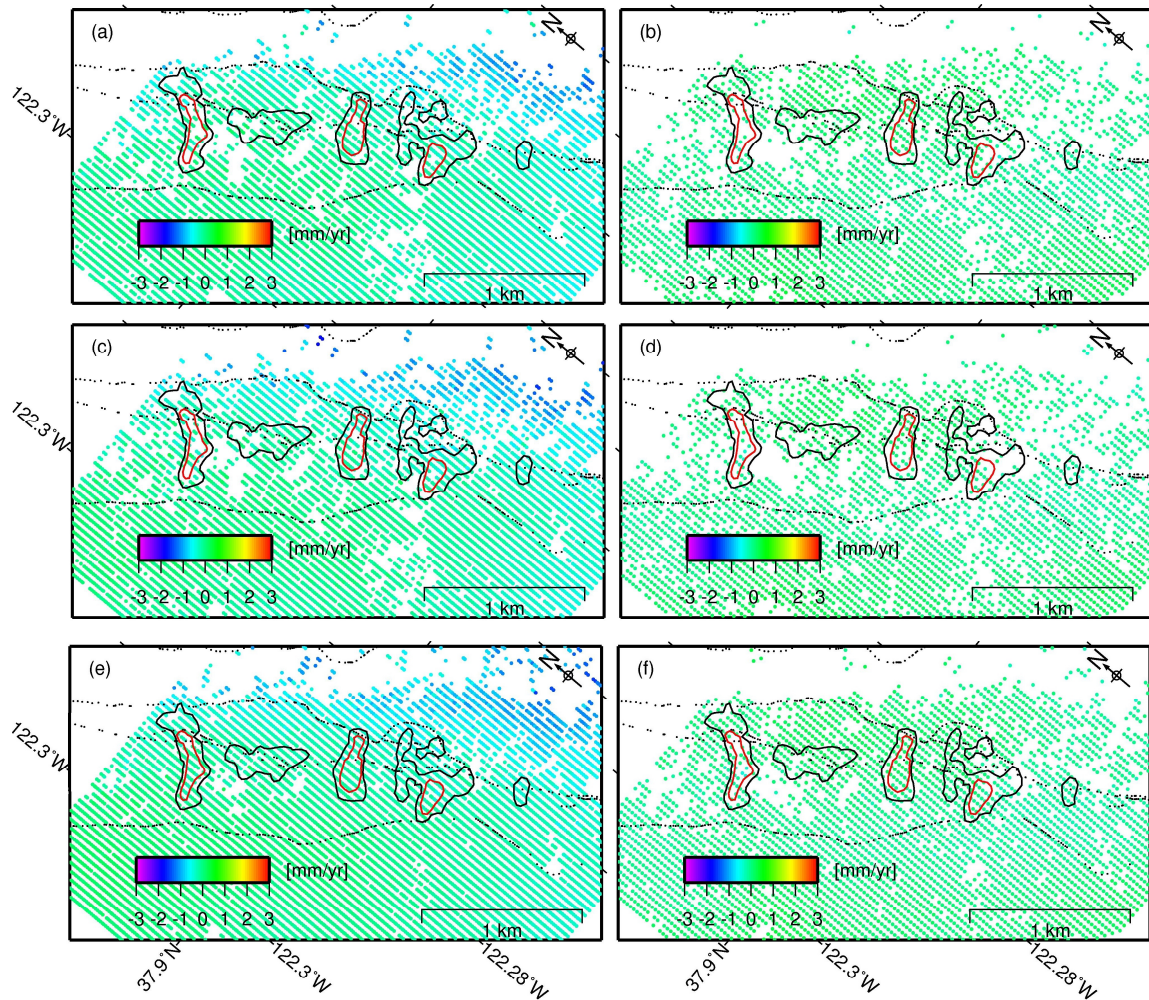


**Figure 4.9. Residual errors of linear deformation rate after application of the SBAS technique: (a), (c) and (e) are the maps from ascending images derived from (a) the HH, (c) the VV and (e) the PolInSAR optimized channel. Figure 4.9 (b), (d) and (f) show the corresponding maps from descending images derived from (b) the HH, (d) the VV and (f) the PolInSAR optimized channel. The black and red polygons outline the location of moderately active and highly active slope instabilities (USGS Earthquake Hazard Program 1999). The black dashed lines represent the faults in this region, as in Figure 4.1.**

Figure 4.9 presents the close up of Figure 4.6 corresponding to the region of landslides, where we have more clear deformation from the slope instabilities. The figure shows the residual errors of linear deformation rate after application of the SBAS technique: (a), (c) and (e) are the maps from ascending images derived from (a) the HH, (c) the VV and (e) the PolInSAR optimized channel. Figure 4.9 (b), (d) and (f) show the corresponding maps from descending images derived from (b) the HH, (d) the VV and (f) the PolInSAR optimized channel. We clearly observe that the errors of the points selected after optimization are of the same orders as the points at their vicinity which are previously selected by HH or VV channels, in both ascending and descending dataset. We conclude that by adding new points our estimation of the linear rates for landslide motion remains the same.

As we note in Figure 4.7-4.8, the landslides resolved by PolInSAR displays a displacement patterns that closely resembles landslides mapped from field investigations. The location of the mapped slides coincides with those identified by Hilley et al. (2004). Moreover, the rates for the newly selected points in landslide region are consistent with the rates from the HH or VV channel. Three of the four slides labeled as highly active and one is marked as moderately active by the prior field investigations. Previous studies (Hilley et al. 2004) estimate a maximum displacement of 35 mm/year along the hill slope for these landslides. Analogous to that analysis, we derived the along-slope rate of surface displacement associated with the time period of 2008-2011 for a constant slope of 4 degrees. We got a maximum rate of 23 mm/year for the movement of the active slides.

The integration of ascending and descending proves to be helpful in distinguishing the different types of landslides by separation of the vertical and horizontal components of the displacement vector. Here we visually assess the sense of motion visually for these slides by using both sets of data. We speculate that most of the landslides in this region have translational behavior, since the slide scarp and the slide foot both are primarily subject to more horizontal than vertical motion. Only the northern slide is recognized as having mainly vertical motion in the middle of the landslide. As noted earlier, our dataset spans a relatively short time period of three years. More in-depth studies of the creep

velocity using a greater number of SAR images are required to investigate the velocity and its potential correlation with meteorological and hydrological factors.

#### **4.7. Conclusion**

In this study we analyzed ten RADARSAT-2 SAR images with ascending geometry and fifteen RADARSAT-2 SAR images with descending geometry from the Hayward fault area using a PolInSAR technique. Our purpose was to increase the number of measurement points for the region, which is mainly dominated by topography and dense vegetation in the hills east of the fault. We showed that the newly added points have the same error as the points previously measured by single-channel HH or VV images. We further observed that there are possible sources of secondary fault creep ~ 5 km northeast of Hayward fault. However, more in depth studies with additional images are required to confirm this feature.

We further analyzed the landslide motion and identified four landslides near Berkeley, with rates of 23 mm/yr. Based on our analysis, one of the slides shows mainly a vertical motion in the middle part, as opposed to others which have translational slide characteristics (mainly horizontal). Furthermore, by using the PolInSAR technique, we get a better pattern for the landslides which correlate well with the landslide map from prior field investigations. This work illustrates the capability of PolInSAR coherence optimization to provide better DInSAR results and more accurate deformation measurements.

#### **4.8. Acknowledgements**

Images were acquired under SOAR-E project 5024 from the Canadian Space Agency. This research was funded by the NSERC and Aon Benfield/ICLR IRC in Earthquake Hazard Assessment, an NSERC Discovery Grant, and an Ontario Early Researcher Award. PJG also acknowledges support from a Banting postdoctoral fellowship (Government of Canada). We thank the Canadian Space Agency for help planning RADARSAT-2 acquisitions. GMT software (Wessel & Smith 1998) was used to create the figures.

#### 4.9. References

- Adam, N., Kampes, B. & Eineder, M. 2005. Development of a scientific permanent scatterer system: Modifications for mixed ERS/ENVISAT time series. *European Space Agency Special Issue Publication*, ESA SP-572, 457-465
- Alipour, S., Tiampo, K. F., Samsonov, S. & Gonzalez, P. J. 2013. Multibaseline PolInSAR using RADARSAT-2 Quad-pol Data: Improvement in Interferometric Phase Analysis. *IEEE Geosci. Remote Sens. Lett.*, doi: 10.1109/LGRS.2012.2237501
- Berardino, P., Fornaro, G., Lanari, R. & Sansosti, E. 2002. A new algorithm for surface deformation monitoring based on small baseline differential SAR interferograms. *IEEE Trans. Geosci. Remote Sens.* **40**, 11, 2375-2383
- Bürgmann, R., *et al.* 2000. Earthquake potential along the northern Hayward fault, California. *Science*, **289**, 5482, 1178-1182
- Bürgmann, R., Fielding, E. & Sukhatme, J. 1998. Slip along the Hayward fault, California, estimated from space-based synthetic aperture radar Interferometry. *Geology*, **26**, 559-562
- Bürgmann, R., Hilley, G., Ferretti, A. & Novali, F. 2006. Resolving vertical tectonics in the San Francisco Bay area from GPS and Permanent Scatterer InSAR analysis. *Geology*, **34**, 221-224
- Cloude, S. R. & Papathanassiou, K. P. 1998. Polarimetric SAR Interferometry. *IEEE Trans. Geosci. Remote Sens.*, **36**, 5, 1551-1565
- Colin, E., Titin-Schnaider, C. & Tabbara, W. 2006. An interferometric coherence optimization method in radar polarimetry for high-resolution imagery. *IEEE Trans. Geosci. Remote Sens.*, **44**, 1, 167-175
- Evans, E. L., Loveless, J. P. & Meade, B. J. 2012. Geodetic constraints on San Francisco Bay Area fault slip rates and potential seismogenic asperities on the partially creeping Hayward fault. *J. Geophys. Res.: Solid Earth*, **117**, doi:10.1029/2004JB003496

Hilley, G. E., *et al.* 2004. Dynamics of Slow-Moving Landslides from Permanent Scatterer Analysis. *Science*, **304**, 5679, 1952-1955, doi: 10.1126/science.1098821

Lienkaemper, J. J., Borchardt, G. & Lisowski, M. 1991. Historic creep rate and potential for seismic slip along the Hayward fault, California. *J. Geophys. Res.*, **96**, B11, 18261-18283

Lienkaemper, J. J., *et al.* 2012. Long-Term Creep Rates on the Hayward Fault: Evidence for Controls on the Size and Frequency of Large Earthquakes. *Bull. Seismol. Soc. Am.*, **102**, 31-41

Lienkaemper, J. J. & Galehouse, J. S. 1997. Revised long-term creep rates on the Hayward fault, Alameda and Contra Costa counties, California. *U. S. Geological Survey*, Open File Rep. 97-690

Lienkaemper, J. J. & Galehouse, J. S. 1998. New evidence doubles the seismic potential of the Hayward fault. *Seis. Res. Letts.*, **69**, 6, 519-523, doi:10.1785/gssrl.69.6.519

Malservisi, R., Gans, C. & Furlong, K. P. 2003. Numerical modeling of strike-slip creeping faults and implications for the Hayward fault, California. *Tectonophysics*, **361**, 1-2, 121-137

Navarro-Sanchez, V. & Lopez-Sanchez, J. M. 2012. Improvement of Persistent-Scatterer Interferometry Performance by Means of a Polarimetric Optimization. *IEEE Geosci. Remote Sens. Lett.*, **9**, 4, 609-613

Navarro-Sanchez, V., Lopez-Sanchez, J. M. & Vicente-Guijalba, F. 2010. A Contribution of Polarimetry to Satellite Differential SAR Interferometry: Increasing the Number of Pixel Candidates. *IEEE Geosci. Remote Sens. Lett.*, **7**, 2, 276-280

Neumann, M., Ferro-Famil, L. & Reigber, A. 2008. Multibaseline polarimetric SAR interferometry coherence optimization. *IEEE Trans. Geosci. Remote Sens.*, **5**, 1, 93-97

- Okada, Y. 1992. Internal deformation due to shear and tensile faults in a half-space, *Bull. Seism. Soc. Am.*, **82**, 1018-1040
- Qong, M. 2005. Coherence Optimization Using the Polarization State Conformation in PolInSAR. *IEEE Geosci. Remote Sen. Lett.*, **2**, 3, 301-305
- Samsonov, S. & Tiampo, K. 2011. Polarization phase difference analysis for selection of persistent scatterers in SAR Interferometry. *IEEE Geosci. Remote Sens. Lett.*, **8**, 2, 331-335
- Savage, J. C. & Lisowski, M. 1993. Inferred depth of creep on the Hayward fault, central California. *J. Geophys. Res.*, **98**, B1, 787-793, doi:10.1029/92JB01871
- Schmidt, D. A., Bürgmann, R., Nadeau, R. M. & d'Alessio, M. 2005. Distribution of aseismic slip rate on the Hayward fault inferred from seismic and geodetic data. *J. Geophys. Res.*, **110**, B08406, doi:10.1029/2004JB003397
- Shirzaei, M & Bürgmann, R. 2013. Time-dependant model of creep on the Hayward Fault from joint inversion of 18 years of InSAR and surface creep data. *J. Geophys. Res.: Solid Earth*, **118**, 1-14, doi:10.1002/jgrb.50149
- Simpson, R.W., Lienkaemper, J. J. & Galehouse, J. S. 2001. Variations in creep rate along the Hayward Fault, California, interpreted as changes in depth of creep. *Geophys. Res. Lett.*, **28**, 11, 2269- 2272
- Tiampo, K. F., González, P. J. & Samsonov, S. 2013. New results for aseismic creep on the Hayward fault using polarization persistent scatterer InSAR. *Earth planet. Sci Lett.*, doi:10.1016/j.epsl.2013.02.019
- Wessel, P. & Smith, W. H. F. 1998. New, improved version of Generic Mapping Tools released. *EOS Trans. Am. Geophys. Union*, **79**, 579
- Williams, R. A., *et al.* 2005. Seismic reflection evidence for a northeast-dipping Hayward fault near Fremont, California: Implications for seismic hazard. *J. Geophys. Res.*, **32**, L13301, doi:10.1029/ 2005GL023113

<http://earthquake.usgs.gov/regional/nca/bayarea/landslides.php>, *USGS open-file report*  
97-745 D. 1991

## 5 Conclusions

### 5.1. Summary and conclusions

The aim of this research was to exploit the latest advancements in radar satellite technology in order to acquire better images of surface deformation caused by geophysical phenomena. More precise surface measurements will provide better and more complete details of the associated causes in the subsurface. Subsequently, this enables us to acquire a better understanding of the future behavior of these sources and estimate the extent of any possible hazard.

In this work, I applied standard DInSAR technique to study faulting mechanisms for the Ahar double earthquakes in northwest Iran ( $M_w = 6.2$  and  $6.4$ ) on August 11, 2012. Fault modeling of coseismic interferograms from a pair of RADARSAT-2 images shows that the two ruptures occurred on a single fault structure, one with east-west orientation. Understanding fault structure is of great importance in this region since the largest strike-slip structure (North Tabriz Fault) lies 50 km away, also with NW-SE geometry. This structure has the highest seismic hazard in the region and previous studies have suggested that most of shear stress in NW Iran primarily is accommodated parallel to this fault (Masson et al. 2007). The results of my study show that some part of the interseismic stress is accommodated on minor faults in NW Iran, such as the east-west oriented Ahar fault. This has important implications for the stress history of the North Tabriz Fault and for future hazard assessment in the region.

The primary focus of this research was in the application and improvement of multibaseline Polarimetric SAR Interferometry (PolInSAR) (Neumann et al. 2008). PolInSAR techniques were developed and assessed in order to better understand the potential improvement associated with the incorporation of fully polarimetric data for increased interferometric coherence. The results demonstrate a considerable increase in the number of Pixel Candidates (PCs), one indicator of interferometric phase reliability and coherence (Ferretti et al. 2001). Moreover, inspection of interferometric phase

(residual RADARSAT-2 orbits) demonstrated an increased phase quality, which can lead to more accurate and unbiased phase unwrapping solution. This improvement of coherence is shown to be dependent on the interferometric spatial and temporal baselines. Generally, for a large temporal or spatial baseline interferograms, we observe a higher coherence increment, due to the lower single-channel coherence.

More measurements are acquired by using this technique in vegetated regions at the eastern part of the fault, which are comparable in terms of error analysis with the standard DInSAR analysis. A study of landslides in the Berkely hills demonstrates that the analysis can provide detailed deformation maps, but also that landslide patterns mapped by PolInSAR better resemble those from field surveys (USGS Open File Report, 1999). This is attributed to the more accurate interferometric phase measurement acquired with the PolInSAR technique.

The choice of the best polarimetric channel derives the most stable scattering in a resolution cell. My analysis shows that there is a correspondence between the increased interferometric coherence and the scattering mechanism of the ground target. The use of PolInSAR resolves mostly double-bounce scattering types in the urban area and surface-type and double-bounce scattering types in the rural regions.

It should be noted that the most stable target does not necessarily correspond to the ground. Rather, it might be associated with other mechanisms such as man-made structures, ground-truck interaction, or some more coherent surface in the vegetation cover. For example in a densely vegetated area, the scattering from tree trunks might be more stable because the vegetation cover limits the wave penetration through to the ground, causing decorrelation. In addition, where there is a high interferometric decorrelation, the optimized solution might not correspond to any particularly stable mechanism. However, the PC selection quality criterion eliminates these pixels from the subset of the pixels for interferometric analysis. Future investigations with the application of PolInSAR coherence optimization using simulated SAR data should be implemented in order to have a better understanding of the optimized scattering types.

Based on the study, we conclude that PolInSAR is a promising technique to increase the reliability of standard DInSAR in order to understand the geophysical phenomena in regions of lower coherence, e.g. when the ground pixels are partly contaminated with volume scattering of vegetation.

## **5.2. Future work**

Potential avenues for future work are outlined as follows:

- Analysis of the scattering mechanisms for the improved coherences, in more detail.
- Apply PolInSAR coherence optimization using ground-based SAR sensors, in which the patterns of deformation are known a priori. This will enable us to quantify the precision of deformation measurements for PolInSAR as compared to single-channel DInSAR analysis.
- Comparison of Multiple Scattering Mechanism (MSM) and Equal Scattering Mechanism (ESM) techniques in terms the scattering mechanism.
- Detailed studies of the scattering mechanism using both ground-truthed natural and synthetic data sets.
- Application of PolInSAR technique in regions of lower coherence in order to measure deformation with increased coherence. Examples of this include the slow-slip events in western Canada.
- Perform a refined analysis of kinematics of northwest Iran, using geodetic data such as GPS, taking into account the Ahar fault geometry.
- Study of the post-seismic deformation of Ahar earthquake using interferometric techniques.

### 5.3. References

- Cameron, W. L. & Leung, L. K. 1990. Feature motivated polarization scattering matrix decomposition. *Proceeding of IEEE International Radar Conference*, Arlington, VA, 549-557
- Cloude, S.R. 1985. Radar target decomposition theorems. *Institute of Electrical Engineering and Electronics Letter*, **21**, 1, 22–24
- Ferretti, A., Prati, C. & Rocca, F. 2001. Permanent scatterers in SAR interferometry. *IEEE Trans. Geosci. Remote Sens.*, **39**, 1, 8-20
- Masson, F. *et al.*, 2007. Large-scale velocity field and strain tensor in Iran inferred from GPS measurements: new insight for the present-day deformation pattern within NE Iran, *Geophys. J. Int.* **170**, 436-440
- Neumann, M., Ferro-Famil, L. & Reigber, A. 2008. Multibaseline polarimetric SAR interferometry coherence optimization. *IEEE Geosci. Remote Sens. Lett.*, **5**, 1, 93-97
- <http://earthquake.usgs.gov/regional/nca/bayarea/landslides.php>, *USGS open-file report 97-745 D*. 1991

## A Glossary

DInSAR	Differential Interferometric Synthetic Aperture Radar
Dual-pol	Dual-Polarization
HH	Horizontal transmission, Horizontal receive
HV	Horizontal transmission, Vertical receive
LOS	Line-of-Sight
MB-ESM	Multi-Baseline Equal Scattering Mechanism
MB-MSM	Multi-Baseline Multiple Scattering Mechanism
PC	Pixel Candidate
PCT	Polarization Coherence Tomography
PolInSAR	Polarimetric SAR Interferometry
Pol-SAR	Polarimetric SAR
PPD	Polarization Phase Difference (PPD)
PS	Permanent Scatterer
Quad-pol	Quad-Polarization
SAR	Synthetic Aperture Radar
SBAS	Small BASeline
SM	Scattering Mechanism
SVD	Singular Value Decomposition
TD	Target Decomposition
VH	Vertical transmission, Horizontal receive
VV	Vertical transmission, Vertical receive

## B Computer Code

### B. 1. Run\_ESM.cpp

```

#include <math.h>

#include <fstream>

#include <iostream>

#include <string.h>

#include <stdlib.h>

#include <stdio.h>

#include <complex>

#include <algorithm>

#include <cstdlib>

#include <algorithm>

#include <sstream>

#include <string>

#include <math.h>

#include <cmath>

#include <gsl/gsl_math.h>

#include <gsl/gsl_eigen.h>

using namespace std;

typedef struct{ double re; double im; } complex16;

extern "C" void zgetri_(int *N, complex16 *a, int *lda, int *ipiv, complex16 *work, int *lwork, int *info);

extern "C" void zgetrf_(int* m,int *n,complex16 *a,int *lda,int *ipiv,int *info);

extern "C" void zgees_(char *jobvs, char *sort, bool *select, int *N, complex16 *a, int *lda, int *sdim,
complex16 *W,complex16 *vs, int *ldvs, complex16 *work, int *lwork, double *rwork, bool *bwork, int
*info);

extern "C" void zgeev_(char *jobvl,char *jobvr,int *N, complex16 *a, int *lda, complex16 *W, complex16
*vl, int *ldvl, complex16 *vr, int *ldvr, complex16 *work, int *lwork, double *rwork, int *info);

extern "C" void zgesvd_(char *jobu,char *jobvt,int *m,int *n,complex16 *A,int *lda,double *S,complex16
*U,int *ldu,complex16 *vt,int *ldvt,complex16 *work, int *lwork, double *rwork, int *info);

```

```
#define float_mem_alloc(data,length) data = (float*) calloc (length,sizeof(float)); if (!data) { printf ("error:
can not allocate memory\n"); return 1;} memset (data, 0, sizeof(float)*length);
```

```
int write_float_data (const char *name, int fwidth, int flength, int cstart, int cstop, int lstart, int lstop, float
*dataR, float *dataI, int be_se)
```

```
{
    ofstream out;
    out.clear();
    out.open (name, ofstream::outofstream::binary);
    if(out.fail())
    {
        printf ("error: can not cretae file %s \n", name);
        return 1;
    }

    char tmpstr[4]; memset (tmpstr, 0, 4);

    int i=0, j=0, myindex=0;
    float a=0, *fdata;
    char* pstr;
    while(j<flength)
    {
        for (i=0; i<fwidth; i++)
        {
            if ((i>=cstart)&&(i<=cstop)&&(j>=lstart)&&(j<=lstop))
            {
                myindex=(i-cstart)+(j-lstart)*(cstop-cstart+1);
                a=dataR[myindex];
            }
            else
            {
                a=0;
            }
        }
    }
}
```

```

fdata=&a;
pstr = reinterpret_cast <char*> (fdata);
if (be_se == 1)
{
    tmpstr[3]=*(pstr+0);
    tmpstr[2]=*(pstr+1);
    tmpstr[1]=*(pstr+2);
    tmpstr[0]=*(pstr+3);
}
else if (be_se == 0)
{
    tmpstr[0]=*(pstr+0);
    tmpstr[1]=*(pstr+1);
    tmpstr[2]=*(pstr+2);
    tmpstr[3]=*(pstr+3);
}
else
{
    printf ("error: input data format is unspecified: %i\n", be_se);
    return 1;
}
out.write(tmpstr,4);
// write imaginary part
if ((i>=cstart)&&(i<=cstop)&&(j>=lstart)&&(j<=lstop))
{
    myindex=(i-cstart)+(j-lstart)*(cstop-cstart+1);
    a=dataI[myindex];
}
else
{
    a=0;
}

```

```

    }
    fdata=&a;
    pstr = reinterpret_cast <char*> (fdata);
    if (be_se == 1)
    {
        tmpstr[3]=*(pstr+0);
        tmpstr[2]=*(pstr+1);
        tmpstr[1]=*(pstr+2);
        tmpstr[0]=*(pstr+3);
    }
    else if (be_se == 0)
    {
        tmpstr[0]=*(pstr+0);
        tmpstr[1]=*(pstr+1);
        tmpstr[2]=*(pstr+2);
        tmpstr[3]=*(pstr+3);
    }
    else
    {
        printf ("error: input data format is unspecified: %i\n", be_se);
        return 1;
    }
    out.write(tmpstr,4);
}
j++;
}
out.close();
return 0;
}

int read_complex_data (char *name, int fwidth, int flength, int cstart, int cstop, int lstart, int lstop, float
*dataR, float *dataI, int be_se)

```

```

{
    char tmpstr[4]; memset (tmpstr, 0, 4);
    int i=0, j=0, num=0, myindex=0;
    float *fdata;
    void *v;
    int floatwidth=8*fwidth;
    char* readdata = (char*) calloc (floatwidth,sizeof(char));
    if (!readdata)
    {
        printf ("error: can not allocate memory for readdata array\n");
        return 1;
    }
    memset (readdata, 0, floatwidth);
    ifstream in;
    in.clear();
    in.open (name, ifstream::in|ifstream::binary);
    if(in.fail())
    {
        printf ("error: can not open file %s \n", name);
        return 1;
    }
    j=0;
    while(!in.eof())
    {
        in.read(readdata,floatwidth);
        num = in.gcount();
        if (num == floatwidth)
        {
            for (i=0; i<fwidth; i++)
            {
                //read real part
            }
        }
    }
}

```

```

if (be_se == 1)
{
    tmpstr[3]=readdata[8*i+0];
    tmpstr[2]=readdata[8*i+1];
    tmpstr[1]=readdata[8*i+2];
    tmpstr[0]=readdata[8*i+3];
}
else if (be_se == 0)
{
    tmpstr[0]=readdata[8*i+0];
    tmpstr[1]=readdata[8*i+1];
    tmpstr[2]=readdata[8*i+2];
    tmpstr[3]=readdata[8*i+3];
}
else
{
    printf ("error: input data format is unspecified: %i\n", be_se);
    return 1;
}
v=(void*)tmpstr;
fdata = reinterpret_cast <float*> (v);
if ((i>=cstart)&&(i<=cstop)&&(j>=lstart)&&(j<=lstop))
{
    myindex=(i-cstart)+(j-lstart)*(cstop-cstart+1);
    //cout<<i<<" "<<cstart<<" "<<j<<" "<<lstart<<" "<<myindex<<endl;;
    dataR[myindex]=*fdata;
}
// read img part
if (be_se == 1)
{
    tmpstr[3]=readdata[8*i+4];

```



```

        return 1;
    }
}
j++;
}
in.close();
free(readdata);
return 0;
}

////////////////////////////////////

int Sca_Vec_Generation (char *name1, char *name2, char *name3, int fwidth, int flength, float *K1, float
*K2, float *K3, float *K4, float *K5, float *K6, int wmin, int wmax, int lmin, int lmax)
{
float *dataRhh, *dataIhh;
float *dataRvv, *dataIvv;
float *dataRvh, *dataIvh;
float_mem_alloc(dataRhh, (wmax-wmin+1)*(lmax-lmin+1));
float_mem_alloc(dataIhh, (wmax-wmin+1)*(lmax-lmin+1));
cout << "read HH data" << endl;
read_complex_data (name1, fwidth, flength, wmin-1, wmax-1, lmin-1, lmax-1, dataRhh, dataIhh, 1);
float_mem_alloc(dataRvv, (wmax-wmin+1)*(lmax-lmin+1));
float_mem_alloc(dataIvv, (wmax-wmin+1)*(lmax-lmin+1));
cout << "read VV data" << endl;
read_complex_data (name3, fwidth, flength, wmin-1, wmax-1, lmin-1, lmax-1, dataRvv, dataIvv, 1);
cout << "Generating Scattering Vector (part 1)" << endl;
for ( int i = 0; i < (wmax-wmin+1)*(lmax-lmin+1); i++ ) {
K1[i]=(dataRhh[i]+dataRvv[i])/1.4142;
K4[i]=(dataIhh[i]+dataIvv[i])/1.4142;
K2[i]=(dataRvv[i]-dataRhh[i])/1.4142;
K5[i]=(dataIvv[i]-dataIhh[i])/1.4142;
}
}

```

```

free(dataRhh);

free(dataIhh);

free(dataRvv);

free(dataIvv);

float_mem_alloc(dataRvh,(wmax-wmin+1)*(lmax-lmin+1));

float_mem_alloc(dataIvh,(wmax-wmin+1)*(lmax-lmin+1));

cout << "read VH data" << endl;

read_complex_data (name2, fwidth, flength, wmin-1, wmax-1, lmin-1, lmax-1, dataRvh, dataIvh, 1);

cout << "Generating Scattering Vector (part 2)" << endl;

for ( int i = 0; i < (wmax-wmin+1)*(lmax-lmin+1); i++ ) {

K3[i]=(2*dataRvh[i])/1.4142;

K6[i]=(2*dataIvh[i])/1.4142;

}

free(dataRvh);

free(dataIvh);

}

////////////////////////////////////

int Cova_Mat_Cons(float *K1R,float *K2R,float *K3R,float *K1I,float *K2I,float *K3I,float *GRo,float
*GIo,int itab,int itab1, int jj, int jj1, int fwidth, int flength, int slc_num, int wmin, int lmin)

{

float GR[3][3],GI[3][3];

for (int kk=0; kk<=2; kk++){

for (int pp=0; pp<=2; pp++){

GR[kk][pp]=0 ;GI[kk][pp]=0;

}

}

int j;

int j1;

for (int i=0; i<=9; i++){

for (int ii=0; ii<=4; ii++){

```

```

j=itab*flength*fwidth+(jj+5-i)*fwidth+jj1+2-ii;
j1=itab1*flength*fwidth+(jj+5-i)*fwidth+jj1+2-ii;
GR[0][0]=GR[0][0]+(K1R[j]*K1R[j1]+K1I[j]*K1I[j1])/50;
GR[0][1]=GR[0][1]+(K1R[j]*K2R[j1]+K1I[j]*K2I[j1])/50;
GR[0][2]=GR[0][2]+(K1R[j]*K3R[j1]+K1I[j]*K3I[j1])/50;
GR[1][0]=GR[1][0]+(K2R[j]*K1R[j1]+K2I[j]*K1I[j1])/50;
GR[1][1]=GR[1][1]+(K2R[j]*K2R[j1]+K2I[j]*K2I[j1])/50;
GR[1][2]=GR[1][2]+(K2R[j]*K3R[j1]+K2I[j]*K3I[j1])/50;
GR[2][0]=GR[2][0]+(K3R[j]*K1R[j1]+K3I[j]*K1I[j1])/50;
GR[2][1]=GR[2][1]+(K3R[j]*K2R[j1]+K3I[j]*K2I[j1])/50;
GR[2][2]=GR[2][2]+(K3R[j]*K3R[j1]+K3I[j]*K3I[j1])/50;
GI[0][0]=GI[0][0]+(K1I[j]*K1R[j1]-K1R[j]*K1I[j1])/50;
GI[0][1]=GI[0][1]+(K1I[j]*K2R[j1]-K1R[j]*K2I[j1])/50;
GI[0][2]=GI[0][2]+(K1I[j]*K3R[j1]-K1R[j]*K3I[j1])/50;
GI[1][0]=GI[1][0]+(K2I[j]*K1R[j1]-K2R[j]*K1I[j1])/50;
GI[1][1]=GI[1][1]+(K2I[j]*K2R[j1]-K2R[j]*K2I[j1])/50;
GI[1][2]=GI[1][2]+(K2I[j]*K3R[j1]-K2R[j]*K3I[j1])/50;
GI[2][0]=GI[2][0]+(K3I[j]*K1R[j1]-K3R[j]*K1I[j1])/50;
GI[2][1]=GI[2][1]+(K3I[j]*K2R[j1]-K3R[j]*K2I[j1])/50;
GI[2][2]=GI[2][2]+(K3I[j]*K3R[j1]-K3R[j]*K3I[j1])/50;
}
}
//cout << jj << " " <<jj1<< endl;
GRo[0] = GR[0][0];
GRo[1] = GR[0][1];
GRo[2] = GR[0][2];
GRo[3] = GR[1][0];
GRo[4] = GR[1][1];
GRo[5] = GR[1][2];
GRo[6] = GR[2][0];
GRo[7] = GR[2][1];

```

```

GRo[8] = GR[2][2];

GIo[0] = GI[0][0];
GIo[1] = GI[0][1];
GIo[2] = GI[0][2];
GIo[3] = GI[1][0];
GIo[4] = GI[1][1];
GIo[5] = GI[1][2];
GIo[6] = GI[2][0];
GIo[7] = GI[2][1];
GIo[8] = GI[2][2];
}

////////////////////////////////////

int MMultiply(float *M1,float *M2,float *M3,float *M4,float *M5,float *M6, int slc_num)
{
complex <double> G[slc_num][slc_num];
complex <double> T[slc_num][slc_num];
complex <double> Mu[slc_num][slc_num];
int k=0;
for (int i=0; i< slc_num; i++){
for (int j=0; j< slc_num; j++){
//cout << "*****multiply*****" <<endl;
T[j][i] = complex<double>(M1[k],M2[k]);
G[j][i] = complex<double>(M3[k],M4[k]);
Mu[j][i] = complex<double>(0,0);
k=k+1;
}
}
for (int i=0; i< slc_num; i++){
for (int j=0; j< slc_num; j++){
for (int i1=0; i1< slc_num; i1++){

```

```

Mu[i][j] = Mu[i][j] + T[i][i1]*G[i1][j];
}
}
}
k=0;
for (int i=0; i< slc_num; i++){
for (int j=0; j< slc_num; j++){
M5[k]=real(Mu[j][i]);
M6[k]=imag(Mu[j][i]);
k=k+1;
}
}
}
////////////////////////////////////
int Root_Square(int m,int n,int N,float *M1, float *M2){
int lda=m;
int lda2=m;
bool SELECT[3];
bool BWORK[m];
char *jobvl="N";
char *jobvr="V";
int ldvr=3;
int ldvl=3;
complex16 vl[m*m];
complex16 vr[m*m];
int info;
int info2;
int lwork =500;
complex16 work[500];
int lwork2 =500;
complex16* work2;

```

```

work2=(complex16*)malloc(lwork2*sizeof(complex16) );
double rwork[2*m];
complex16 W[m];
int ipiv[m];
complex16 F1[m*m];
int SDIM=3;
double S[3];
complex16 u[9];
complex16 v[9];
float *M3,*M4,*M5,*M6,*M7,*M8;
float_mem_alloc(M3,m*m);
float_mem_alloc(M4,m*m);
float_mem_alloc(M5,m*m);
float_mem_alloc(M6,m*m);
float_mem_alloc(M7,m*m);
float_mem_alloc(M8,m*m);
for (int i=0; i<m*m; i++){
F1[i].re=double(M1[i]);
F1[i].im=double(M2[i]);
}
//zgees_("N","S",SELECT,&N,F1,&lda2,&SDIM,W,vr,&ldvr,work2, &lwork2,rwork, BWORK,&info2);
//zgeev_("N","V",&N, F1, &lda2, W, vl,&ldvl, vr, &ldvr,work2, &lwork2, rwork, &info2);
zgesvd_("A","A",&m,&N,F1,&lda2,S,u,&lda2,v,&lda2,work2,&lwork2,rwork,&info2);
//cout<< " THIS IS U " <<endl;
for (int i=0; i<m*m; i++){
M1[i]=float(u[i].re);
M2[i]=float(u[i].im);
//cout<< u[i].re <<" +" <<u[i].im<<"i" <<endl;
}
//cout<< " THIS IS S " <<endl;
for (int i=0; i<m; i++){

```

```

M3[i*m+i]=sqrt(S[i]);
M4[i*m+i]=0;
//cout<< S[i] <<endl;
}
//cout<< " THIS IS V " <<endl;
for (int i=0; i<m; i++){
for (int j=0; j<m; j++){
M5[i*m+j]=float(v[i*m+j].re);
M6[i*m+j]=float(v[i*m+j].im);
//cout<< v[j*m+i].re <<" +" <<v[j*m+i].im<<"i" <<endl;
}
}
//cout<< " THIS IS A TEST " <<endl;
for (int i=0; i<m*m; i++){
//cout<< M5[i] <<" +" <<M6[j] <<"i" <<endl;
}
MMultiply(M1,M2,M3,M4,M7,M8,m);
MMultiply(M7,M8,M5,M6,M1,M2,m);
for (int i=0; i<m*m; i++){
F1[i].re=M1[i];
F1[i].im=M2[i];
}
zgetrf_(&m,&n,F1,&lda,ipiv,&info);
zgetri_(&N,F1,&lda,ipiv,work,&lwork,&info);
//cout<< " THIS IS A TEST " <<endl;
for (int i=0; i<m*m; i++){
M1[i]=F1[i].re;
M2[i]=F1[i].im;
//cout<< M1[i] <<" +" <<M2[i] <<"i" <<endl;
}
free(M3);free(M4);free(M5);free(M6);free(M7);free(M8);

```

```

}

int ESM(float *T1,float *T2,float *initial, int int_num,float *WESM1,float *WESM2,float *WESM3,float
*WESM4){

float *M1, *M2;

complex<double>temp;

complex<double>temp1;

float *M3,*M4,*M5,*M6,*M7,*M8,*M9,*M10;

complex16 F1[9];

int N=3;

int lda=3;

char *jobvl="N";

char *jobvr="V";

int ldvr=3;

int ldvl=3;

complex16 vl[9];

complex16 vr[9];

int info2;

int lwork2 =500;

complex16 work2[500];

double rwork[6];

complex16 W[3];

int ipiv[3];

float mmm,maxx;int sh;

for(int itt=0;itt<5;itt++){

//cout<< initial[0]<< " " << initial[1] << " " << initial[2] << endl;

float_mem_alloc(M1,9);

float_mem_alloc(M2,9);

float_mem_alloc(M3,9);

float_mem_alloc(M4,9);

float_mem_alloc(M5,9);

float_mem_alloc(M6,9);

```

```

float_mem_alloc(M7,9);
float_mem_alloc(M8,9);
float_mem_alloc(M9,9);
float_mem_alloc(M10,9);
for (int j=0;j<int_num;j++){
temp1=complex<double>(cos(initial[j]),-sin(initial[j]));
for (int i=0;i<9;i++){
temp=complex<double>(T1[9*j+i],T2[9*j+i]);
M1[i]=M1[i]+real((temp*temp1));
M2[i]=M2[i]+imag((temp*temp1));
}
}
for (int i=0;i<9;i++){
F1[i].re=M1[i];
F1[i].im=M2[i];
}
zgeev_(jobvl,jobvr,&N, F1, &lida, W, vl, &ldvl, vr, &ldvr,work2, &lwork2, rwork, &info2);
maxx=abs(complex<double>(W[0].re,W[0].im));sh=0;
for (int itab=0; itab < 3 ; itab++){
mmm=abs(complex<double>(W[itab].re,W[itab].im));
if (maxx<mmm) { maxx= mmm; sh=itab; }
}
M3[0]=vr[3*sh].re;M3[3]=vr[3*sh+1].re;M3[6]=vr[3*sh+2].re;M3[1]=0;M3[2]=0;M3[4]=0;M3[5]=0;M3[7]=0;M3[8]=0;
M4[0]=-vr[3*sh].im;M4[3]=-vr[3*sh+1].im;M4[6]=-vr[3*sh+2].im;M4[1]=0;M4[2]=0;M4[4]=0;M4[5]=0;M4[7]=0;M4[8]=0;
M7[0]=vr[3*sh].re;M7[1]=vr[3*sh+1].re;M7[2]=vr[3*sh+2].re;M7[3]=0;M7[4]=0;M7[5]=0;M7[6]=0;M7[7]=0;M7[8]=0;
M8[0]=vr[3*sh].im;M8[1]=vr[3*sh+1].im;M8[2]=vr[3*sh+2].im;M8[3]=0;M8[4]=0;M8[5]=0;M8[6]=0;M8[7]=0;M8[8]=0;
for (int i=0;i<int_num;i++){
for (int j=0;j<9;j++){
M5[j]=T1[i*9+j];M6[j]=T2[i*9+j];

```

```

}
MMultiply(M3,M4,M5,M6,M1,M2,3);
MMultiply(M1,M2,M7,M8,M9,M10,3);
initial[i]=arg(complex<double>(M9[0],M10[0]));
}
} //ITERATION END
for (int i=0;i<9;i++){
WESM1[i]=M3[i];WESM2[i]=M4[i];
WESM3[i]=M7[i];WESM4[i]=M8[i];
}
free(M1);free(M2);free(M3);free(M4);free(M5);free(M6);free(M7);free(M8);free(M9);free(M10);
}
//inside main:
main(int argc, char *argv[])
{
int fwidth=atoi(argv[1]);
int flength=atoi(argv[2]);
int wmin=atoi(argv[3]);
int wmax=atoi(argv[4]);
int lmin=atoi(argv[5]);
int lmax=atoi(argv[6]);
int Y=atoi(argv[7]);
int YY=atoi(argv[8]);
//Read SLC_file (BEG)
ifstream File("slc_file1");
    if (File == NULL)
    {
        printf ("error: can not open parameter file: itab \n");
        return 1;
    }
    long begin,end,size;

```

```

File.seekg (0, ios::beg);
begin = File.tellg();
File.seekg (0, ios::end);
end = File.tellg();
size = end-begin;
cout << " slc_file size is: " << size << endl;
File.seekg (0, ios::beg);
string x;
File >> x;
File.seekg (0, ios::beg);
int slc_num = size/(x.size()+1);
char SLC_data[slc_num+1][256];
char x1[256];
int o=0;
while (!File.eof())
{
    memset (x1, 0, 256);
    File >> x1;
    memset (SLC_data[o], 0, 256);
    if (o< slc_num){
        strcpy(SLC_data[o],x1) ;
        cout << "SLC: " << SLC_data[o] << " SLC size: " << sizeof(SLC_data[o]) << endl;
        cout << " O is equal to: " << o<< endl;
        o=o+1;
    }
}
cout << " Number of SLC images are:" << slc_num << endl;
//Read SLC_file (END)
float *name1;float *name2;float *name3;
float *name4;float *name5;float *name6;
float_mem_alloc(name1,(wmax-wmin+1)*(lmax-lmin+1)*slc_num/3);

```

```

float_mem_alloc(name2,(wmax-wmin+1)*(lmax-lmin+1)*slc_num/3);
float_mem_alloc(name3,(wmax-wmin+1)*(lmax-lmin+1)*slc_num/3);
float_mem_alloc(name4,(wmax-wmin+1)*(lmax-lmin+1)*slc_num/3);
float_mem_alloc(name5,(wmax-wmin+1)*(lmax-lmin+1)*slc_num/3);
float_mem_alloc(name6,(wmax-wmin+1)*(lmax-lmin+1)*slc_num/3);

for ( int j = 0; j < slc_num; j=j+3 ) {
cout << "Reading SLC_image " << j/3 << endl;

Sca_Vec_Generation (SLC_data[j], SLC_data[j+1], SLC_data[j+2], fwidth, flength,
&(name1[(j/3)*(wmax-wmin+1)*(lmax-lmin+1)]), &(name2[(j/3)*(wmax-wmin+1)*(lmax-lmin+1)]),
&(name3[(j/3)*(wmax-wmin+1)*(lmax-lmin+1)]), &(name4[(j/3)*(wmax-wmin+1)*(lmax-lmin+1)]),
&(name5[(j/3)*(wmax-wmin+1)*(lmax-lmin+1)]), &(name6[(j/3)*(wmax-wmin+1)*(lmax-
lmin+1)]),wmin,wmax,lmin,lmax);

}

int j;

float *GRo;

float *GIo;

float *GRo1;

float *GIo1;

int m=3;

int n=3;

int N=3;

complex<double> WW1[3];

complex<double> kk1[3][1];

char name[256];

char name_n[256];

int ssa1, ssb1;

cout <<" ***Generate Covariance Matrixes*** " << endl;

float *M1, *M2, *M3, *M4, *M5, *M6, *M7, *M8, *M9, *M10,*initial;

float *W1out;float *W2out;float *W3out;

float *W4out;float *W5out;float *W6out;

float *T1, *T2;

float_mem_alloc(W1out,(wmax-wmin+1)*(lmax-lmin+1));

```

```

float_mem_alloc(W2out,(wmax-wmin+1)*(lmax-lmin+1));
float_mem_alloc(W3out,(wmax-wmin+1)*(lmax-lmin+1));
float_mem_alloc(W4out,(wmax-wmin+1)*(lmax-lmin+1));
float_mem_alloc(W5out,(wmax-wmin+1)*(lmax-lmin+1));
float_mem_alloc(W6out,(wmax-wmin+1)*(lmax-lmin+1));
int int_num;
complex<double>temp;
for ( int jj = 4; jj < (lmax-lmin+1)-5; jj=jj+10 ) {
for ( int jj1 = 2; jj1 < (wmax-wmin+1)-2; jj1=jj1+5 ) {
int_num=0;
float_mem_alloc(T1,9*(slc_num/3-1)*(slc_num/3));
float_mem_alloc(T2,9*(slc_num/3-1)*(slc_num/3));
float_mem_alloc(initial,(slc_num/3)*(slc_num/3-1));
float_mem_alloc(M3,9);
float_mem_alloc(M4,9);
for ( int itab=0; itab <slc_num/3; itab++){
float_mem_alloc(GIo1,9);
float_mem_alloc(GRo1,9);
Cova_Mat_Cons(name1,name2,name3,name4,name5,name6,GRo1,GIo1,itab,itab,jj,jj1,(wmax-
wmin+1),(lmax-lmin+1),slc_num, wmin, lmin);
M3[0]=M3[0]+(double)GRo1[0]/(slc_num/3);
M3[1]=M3[1]+(double)GRo1[3]/(slc_num/3);
M3[2]=M3[2]+(double)GRo1[6]/(slc_num/3);
M3[3]=M3[3]+(double)GRo1[1]/(slc_num/3);
M3[4]=M3[4]+(double)GRo1[4]/(slc_num/3);
M3[5]=M3[5]+(double)GRo1[7]/(slc_num/3);
M3[6]=M3[6]+(double)GRo1[2]/(slc_num/3);
M3[7]=M3[7]+(double)GRo1[5]/(slc_num/3);
M3[8]=M3[8]+(double)GRo1[8]/(slc_num/3);
M4[0]=M4[0]+(double)GIo1[0]/(slc_num/3);
M4[1]=M4[1]+(double)GIo1[3]/(slc_num/3);

```

```

M4[2]=M4[2]+(double)GIo1[6]/(slc_num/3);
M4[3]=M4[3]+(double)GIo1[1]/(slc_num/3);
M4[4]=M4[4]+(double)GIo1[4]/(slc_num/3);
M4[5]=M4[5]+(double)GIo1[7]/(slc_num/3);
M4[6]=M4[6]+(double)GIo1[2]/(slc_num/3);
M4[7]=M4[7]+(double)GIo1[5]/(slc_num/3);
M4[8]=M4[8]+(double)GIo1[8]/(slc_num/3);
}
Root_Square(m,n,N,M3,M4);
for ( int itab=0; itab <slc_num/3; itab++){
for ( int itab1=0; itab1 <slc_num/3; itab1++){
//for ( int itab=0; itab <1; itab++){
//for ( int itab1=itab+1; itab1 <3; itab1++){
if (itab!=itab1){
float_mem_alloc(GIo,9);
float_mem_alloc(GRo,9);
float_mem_alloc(M1,9);
float_mem_alloc(M2,9);
float_mem_alloc(M5,9);
float_mem_alloc(M6,9);
float_mem_alloc(M7,9);
float_mem_alloc(M8,9);
float_mem_alloc(M9,9);
float_mem_alloc(M10,9);
temp=complex<double>(0,0);
Cova_Mat_Cons(name1,name2,name3,name4,name5,name6,GRo,GIo,itab,itab1,jj,jj1,(wmax-
wmin+1),(lmax-lmin+1),slc_num, wmin, lmin);
M1[0]=(double)GRo[0];
M1[1]=(double)GRo[3];
M1[2]=(double)GRo[6];
M1[3]=(double)GRo[1];

```

```

M1[4]=(double)GRo[4];
M1[5]=(double)GRo[7];
M1[6]=(double)GRo[2];
M1[7]=(double)GRo[5];
M1[8]=(double)GRo[8];
M2[0]=(double)GIo[0];
M2[1]=(double)GIo[3];
M2[2]=(double)GIo[6];
M2[3]=(double)GIo[1];
M2[4]=(double)GIo[4];
M2[5]=(double)GIo[7];
M2[6]=(double)GIo[2];
M2[7]=(double)GIo[5];
M2[8]=(double)GIo[8];
MMultiply(M3,M4,M1,M2,M5,M6,m);
MMultiply(M5,M6,M3,M4,M7,M8,m);
temp=complex<double>(M7[0],M8[0])+complex<double>(M7[4],M8[4])+complex<double>(M7[8],M8[8]);
initial[int_num]=float(arg(temp));
T1[9*int_num+0]=(double)M7[0];
T1[9*int_num+1]=(double)M7[1];
T1[9*int_num+2]=(double)M7[2];
T1[9*int_num+3]=(double)M7[3];
T1[9*int_num+4]=(double)M7[4];
T1[9*int_num+5]=(double)M7[5];
T1[9*int_num+6]=(double)M7[6];
T1[9*int_num+7]=(double)M7[7];
T1[9*int_num+8]=(double)M7[8];

T2[9*int_num+0]=(double)M8[0];
T2[9*int_num+1]=(double)M8[1];

```

```

T2[9*int_num+2]=(double)M8[2];
T2[9*int_num+3]=(double)M8[3];
T2[9*int_num+4]=(double)M8[4];
T2[9*int_num+5]=(double)M8[5];
T2[9*int_num+6]=(double)M8[6];
T2[9*int_num+7]=(double)M8[7];
T2[9*int_num+8]=(double)M8[8];
int_num=int_num+1;
}
}
}
ESM(T1,T2,initial,int_num,M5,M6,M7,M8);
MMultiply(M5,M6,M3,M4,M1,M2,m);
MMultiply(M1,M2,M7,M8,M9,M10,m);
float temp10=M9[0];
MMultiply(M3,M4,M7,M8,M1,M2,m);
WW1[0] = complex<double>(M1[0]/temp10,M2[0]/temp10);
WW1[1] = complex<double>(M1[1]/temp10,M2[1]/temp10);
WW1[2] = complex<double>(M1[2]/temp10,M2[2]/temp10);
for (int ssa=0;ssa<10;ssa++){
for (int ssb=0;ssb<5;ssb++){
ssa1=jj+5-ssa;
ssb1=jj1+2-ssb;
W1out[ssa1*(wmax-wmin+1)+ssb1]=real(WW1[0]);
W4out[ssa1*(wmax-wmin+1)+ssb1]=imag(WW1[0]);

W2out[ssa1*(wmax-wmin+1)+ssb1]=real(WW1[1]);
W5out[ssa1*(wmax-wmin+1)+ssb1]=imag(WW1[1]);
W3out[ssa1*(wmax-wmin+1)+ssb1]=real(WW1[2]);
W6out[ssa1*(wmax-wmin+1)+ssb1]=imag(WW1[2]);
}
}

```

```
}  
} //end of col  
cout << " Generate Covariance Matrixes for Line " << jj << endl;  
} //end of row  
memset (name, 0, 256);  
strcat(name,"W0");  
write_float_data (name, fwidth, flength, wmin-1, wmax-1, lmin-1, lmax-1, W1out, W4out, 1);  
memset (name, 0, 256);  
strcat(name,"W1");  
write_float_data (name, fwidth, flength, wmin-1, wmax-1, lmin-1, lmax-1, W2out, W5out, 1);  
memset (name, 0, 256);  
strcat(name,"W2");  
write_float_data (name, fwidth, flength, wmin-1, wmax-1, lmin-1, lmax-1, W3out, W6out, 1);  
}
```

## B. 2. Complement.cpp

```

#include <math.h>
#include <fstream>
#include <iostream>
#include <string.h>
#include <stdlib.h>
#include <stdio.h>
#include <complex>
#include <algorithm>
#include <cstdlib>
#include <algorithm>
#include <sstream>
#include <string>
#include <math.h>
#include <cmath>
using namespace std;

typedef struct{ double re; double im; } complex16;

extern "C" void zgetri_(int *N, complex16 *a, int *lda, int *ipiv, complex16 *work, int *lwork, int *info);

extern "C" void zgetrf_(int* m,int *n,complex16 *a,int *lda,int *ipiv,int *info);

extern "C" void zgees_(char *jobvs, char *sort, bool *select, int *N, complex16 *a, int *lda, int *sdim,
complex16 *W,complex16 *vs, int *ldvs, complex16 *work, int *lwork, complex16 *rwork, bool *bwork,
int *info);

extern "C" void zgeev_(char *jobvl,char *jobvr,int *N, complex16 *a, int *lda, complex16 *W, complex16
*v1, int *ldvl, complex16 *vr, int *ldvr, complex16 *work, int *lwork, complex16 *rwork, int *info);

#define float_mem_alloc(data,length) data = (float*) calloc (length,sizeof(float)); if (!data) { printf ("error:
can not allocate memory\n"); return 1;} memset (data, 0, sizeof(float)*length);

int Sca_Vec_Generation (char *name1, char *name2, char *name3, int fwidth, int flength, float *K1, float
*K2, float *K3, float *K4, float *K5, float *K6,int wmin,int wmax,int lmin,int lmax)

{

float *dataRhh, *dataIhh;

float *dataRvv, *dataIvv;

```

```

float *dataRvh, *dataIvh;

float_mem_alloc(dataRhh,(wmax-wmin+1)*(lmax-lmin+1));
float_mem_alloc(dataIhh,(wmax-wmin+1)*(lmax-lmin+1));
cout << "read HH data" << endl;

read_complex_data (name1, fwidth, flength, wmin-1, wmax-1, lmin-1, lmax-1, dataRhh, dataIhh, 1);

float_mem_alloc(dataRvv,(wmax-wmin+1)*(lmax-lmin+1));
float_mem_alloc(dataIvv,(wmax-wmin+1)*(lmax-lmin+1));
cout << "read VV data" << endl;

read_complex_data (name3, fwidth, flength, wmin-1, wmax-1, lmin-1, lmax-1, dataRvv, dataIvv, 1);

cout << "Generating Scattering Vector (part 1)" << endl;
for ( int i = 0; i < (wmax-wmin+1)*(lmax-lmin+1); i++ ) {
K1[i]=(dataRhh[i]+dataRvv[i])/1.4142;
K4[i]=(dataIhh[i]+dataIvv[i])/1.4142;
K2[i]=(dataRvv[i]-dataRhh[i])/1.4142;
K5[i]=(dataIvv[i]-dataIhh[i])/1.4142;
}
free(dataRhh);
free(dataIhh);
free(dataRvv);
free(dataIvv);

float_mem_alloc(dataRvh,(wmax-wmin+1)*(lmax-lmin+1));
float_mem_alloc(dataIvh,(wmax-wmin+1)*(lmax-lmin+1));
cout << "read VH data" << endl;

read_complex_data (name2, fwidth, flength, wmin-1, wmax-1, lmin-1, lmax-1, dataRvh, dataIvh, 1);

cout << "Generating Scattering Vector (part 2)" << endl;
for ( int i = 0; i < (wmax-wmin+1)*(lmax-lmin+1); i++ ) {
K3[i]=(2*dataRvh[i])/1.4142;
K6[i]=(2*dataIvh[i])/1.4142;
}
free(dataRvh);
free(dataIvh);

```

```

}
//inside main:
main(int argc, char *argv[])
{
int fwidth=atoi(argv[1]);
int flength=atoi(argv[2]);
int wmin=atoi(argv[3]);
int wmax=atoi(argv[4]);
int lmin=atoi(argv[5]);
int lmax=atoi(argv[6]);
int mm1=atoi(argv[7]);
complex<double> WW1[6][1];
complex<double> kk1[6][1];
complex<double> eq5, eq6;
//Read SLC_file (BEG)
ifstream File("slc_file1");
    if (File == NULL)
    {
        printf ("error: can not open parameter file: itab \n");
        return 1;
    }
    long begin,end,size;
    File.seekg (0, ios::beg);
    begin = File.tellg();
    File.seekg (0, ios::end);
    end = File.tellg();
    size = end-begin;
    cout << " slc_file size is: " << size << endl;
    File.seekg (0, ios::beg);
    string x;
    File >> x;

```

```

File.seekg (0, ios::beg);
int slc_num = size/(x.size()+1);
char SLC_data[slc_num+1][256];
char x1[256];
int o=0;
while (!File.eof())
{
    memset (x1, 0, 256);
    File >> x1;
    memset (SLC_data[o], 0, 256);
    if (o< slc_num){
        strcpy(SLC_data[o],x1) ;
        cout << "SLC: " << SLC_data[o] << " SLC size: " << sizeof(SLC_data[o]) << endl;
        cout << " O is equal to: " << o<< endl;
        o=o+1;
    }
}

cout << " Number of SLC images are:" << slc_num << endl;
//Read SLC_file (END)
float *name1;float *name2;float *name3;
float *name4;float *name5;float *name6;
float_mem_alloc(name1,(wmax-wmin+1)*(lmax-lmin+1));
float_mem_alloc(name2,(wmax-wmin+1)*(lmax-lmin+1));
float_mem_alloc(name3,(wmax-wmin+1)*(lmax-lmin+1));
float_mem_alloc(name4,(wmax-wmin+1)*(lmax-lmin+1));
float_mem_alloc(name5,(wmax-wmin+1)*(lmax-lmin+1));
float_mem_alloc(name6,(wmax-wmin+1)*(lmax-lmin+1));
float *dataR1;float *dataR2;float *dataR3;
float *dataI1;float *dataI2;float *dataI3;
float_mem_alloc(dataR1,(wmax-wmin+1)*(lmax-lmin+1));
float_mem_alloc(dataR2,(wmax-wmin+1)*(lmax-lmin+1));

```

```

float_mem_alloc(dataR3,(wmax-wmin+1)*(lmax-lmin+1));
float_mem_alloc(dataI1,(wmax-wmin+1)*(lmax-lmin+1));
float_mem_alloc(dataI2,(wmax-wmin+1)*(lmax-lmin+1));
float_mem_alloc(dataI3,(wmax-wmin+1)*(lmax-lmin+1));

float *outputR1, *outputI1;
float_mem_alloc(outputR1,(wmax-wmin+1)*(lmax-lmin+1));
float_mem_alloc(outputI1,(wmax-wmin+1)*(lmax-lmin+1));
cout << "Reading SLC_image " << mm1 << endl;

Sca_Vec_Generation (SLC_data[3*(mm1-1)], SLC_data[3*(mm1-1)+1], SLC_data[3*(mm1-1)+2],
fwidth, flength,name1,name2,name3, name4,name5,name6,wmin,wmax,lmin,lmax);

char name[256];
memset (name, 0, 256);
strcat(name,"W0");
cout << "read file " << name << endl;
read_complex_data (name, fwidth, flength, wmin-1, wmax-1, lmin-1, lmax-1, dataR1, dataI1, 1);
memset (name, 0, 256);
strcat(name,"W1");
cout << "read file " << name << endl;
read_complex_data (name, fwidth, flength, wmin-1, wmax-1, lmin-1, lmax-1, dataR2, dataI2, 1);
memset (name, 0, 256);
strcat(name,"W2");
cout << "read file " << name << endl;
read_complex_data (name, fwidth, flength, wmin-1, wmax-1, lmin-1, lmax-1, dataR3, dataI3, 1);
for ( int jj = 4; jj < (lmax-lmin+1)-4; jj=jj+1 ) {
for ( int jj1 = 4; jj1 < (wmax-wmin+1)-4; jj1=jj1+1 ) {
//for ( int jj = 3228; jj < 3229; jj=jj+1 ) {
//for ( int jj1 = 2040; jj1 < 2041; jj1=jj1+1 ) {
WW1[0][0]=complex<double>(dataR1[jj*(wmax-wmin+1)+jj1],dataI1[jj*(wmax-wmin+1)+jj1]);
WW1[1][0]=complex<double>(dataR2[jj*(wmax-wmin+1)+jj1],dataI2[jj*(wmax-wmin+1)+jj1]);
WW1[2][0]=complex<double>(dataR3[jj*(wmax-wmin+1)+jj1],dataI3[jj*(wmax-wmin+1)+jj1]);

```

```

kk1[0][0]=complex<double>(name1[jj*(wmax-wmin+1)+jj1],name4[jj*(wmax-wmin+1)+jj1]);
kk1[1][0]=complex<double>(name2[jj*(wmax-wmin+1)+jj1],name5[jj*(wmax-wmin+1)+jj1]);
kk1[2][0]=complex<double>(name3[jj*(wmax-wmin+1)+jj1],name6[jj*(wmax-wmin+1)+jj1]);
eq5=conj(WW1[0][0])*kk1[0][0]+conj(WW1[1][0])*kk1[1][0]+conj(WW1[2][0])*kk1[2][0];
if (isnan(abs(eq5))){
outputR1[jj*(wmax-wmin+1)+jj1]=0;
outputI1[jj*(wmax-wmin+1)+jj1]=0;
}
else
{
outputR1[jj*(wmax-wmin+1)+jj1]=real(eq5);
outputI1[jj*(wmax-wmin+1)+jj1]=imag(eq5);
}
}
}

memset (name, 0, 256);
strcat(name,SLC_data[3*(mm1-1)]) ;
strcat(name,"_pol" ) ;
cout << name << endl;

write_float_data (name, fwidth, flength, wmin-1, wmax-1, lmin-1, lmax-1, outputR1, outputI1, 1);
free(outputR1);
free(outputI1);
}

```

## C Curriculum vitae

### Samira Alipour

#### **Post Secondary Education and Degrees**

K.N. Toosi University of Technology, Tehran, Iran

2002-2006 B.Sc. in Geomatics Engineering

The University of Tehran, Tehran, Iran

2006-2008 M.Sc. in Remote Sensing

The University of Western Ontario, London, ON, Canada

2009-2013 PhD. in Geophysics

#### **Honors and Awards**

WGRS, 2009-2013

Robert and Ruth Lumsden Graduate Fellowship, 2013

KEGS Scholarship, 2012

#### **Related Work Experience**

2009-2013, Research Assistant, the University of Western Ontario

2009-2013, Teaching Assistant, the University of Western Ontario

2009, Geomatics Engineer, NTM Co., Tehran, Iran

2008, Research Assistant, GFZ, Potsdam, Germany

#### **Professional Membership**

AGU, CGU, PDAC

#### **Selected Presentations**

Alipour. S., Motgah. M., Sharifi. M.A., Walter. T.R., "InSAR time series investigation of land subsidence due to groundwater overexploitation in Tehran, Iran", 10.1109/USEREST.2008.4740370.

Alipour. S, Tiampo. K. F, Samsonov. S, "Application of Interferometric Coherence Optimization for Radarsat-2 data over Hayward fault, San Francisco", AGU Fall meeting, 2010, San Fransisco.

Alipour. S, Tiampo. K. F, Samsonov. S, Gonzalez. P. J., "Creep rate estimation along the Hayward fault using polarimetric SAR interferometry", JLG, 2011, Luxamburg.

## **Publications**

S. Alipour, K. F. Tiampo, S. Samsonov, P. J. Gonzalez, “Multibaseline PolInSAR using RADARSAT-2 Quad-pol Data: Improvement in Interferometric Phase Analysis”, IEEE Geosciences and Remote Sensing Letters, (in press), doi: 10.1109/LGRS.2012.2237501.

S. Alipour, K. F. Tiampo, P. J. Gonzalez, S. Samsonov, “Short-term surface deformation on the northern Hayward fault, CA, using Polarimetric SAR Interferometry (PolInSAR)”, accepted by Pure and Applied Geophysics, 2013.

S. Alipour, K. F. Tiampo, P. J. Gonzalez, S. Samsonov, “Source model for the 2012 Ahar double earthquakes, Iran, from DInSAR analysis of RADARSAT-2 imagery”, submitted to the Journal of Geophysical International

S. Alipour, K. F. Tiampo, S. Samsonov, P. J. Gonzalez, “Polarimetric SAR Interferometry (PolInSAR) coherence optimization using RADARSAT-2 imagery for DInSAR applications: analysis of the optimized scattering mechanisms”, submitted to the Canadian Journal of Remote Sensing.